UiT Norges arktiske universitet

Faculty of Science and Technology,

Department of Geoscience

Dating and analysis of the Hinlopen Megaslide, northern Svalbard.

Georga-Marie Hooton

Master's Thesis in Marine Geology and Geophysics - GEO-3900

May 2024

Abstract

During a research cruise in the summer of 2022, a number of sediment cores were collected from the main headwall scar area of the Hinlopen Megaslide, northern Svalbard. In this study two of those sediment cores have undergone ^{14}C AMS radiocarbon dating and a multi-proxy analysis to determine an accurate age for the slide deposits in this location. The results have been calibrated using the Marine20 Radiocarbon Calibration Curve (Heaton et al., 2020) and a ΔR value of 70±30 (Mangerud and Svendsen., 2017).

Two different landslide events have been identified, one is from the southern scar lobe dating to >40ka yrs BP and the other was taken from the eastern headwall area and dates between 15-13ka yrs BP.

These results, along with the ages from Winkelmann et al., (2007) mean that there has been at least a minimum of three landslide events in the Hinlopen Megaslide Complex. The understanding so far is that the 30ka yrs BP age from Winkelmann et al., was the initial main slide event which has been challenged by the results of this study.

All three events occur during warmer climatic conditions, being the Kapp Ekholm Interstadial and the Bølling-Allerød Interstadial, and this implies that warmer climates have a large impact on the stability of the material at the continental shelf at this location.

The potential of a failure in the future has been proposed (Geissler et al., 2016) due to the presence of internally deformed sediment just north of the slide scar. Here surface cracks and slump deposits are frequent and the implication that all three known slide events occurred during warmer periods means that the occurrence of a future event is not impossible.

Acknowledgements

I would like to express my sincerest thanks to my main supervisor for this project Jochen Knies, who has helped me and without him this project would not have been possible. I would also like to thank my co-supervisor Matthias Forwick for answering all of my questions no matter how strange. I would also like to express an enormous thank you to my other co-supervisor Tine Rasmussen who has supported me thorough not only this project but all of my work since the beginning of my time here in Tromsø.

I would also like to take the time to thank the lab technicians in the geoscience lab at Tromsø, Karina Monsen for helping me with the equipment throughout the project and for always taking the time to answer my emails or have a chat, Matteus Lindgren for his support when things did not go to plan, Trine Merete Dhal and Ingvild Hald for also being there as technical support throughout my roadblocks. A thank you to Ule Ninnemann from the University of Bergen who helped me out towards the end when technical errors made me think I wouldn't be able to finish.

An incredible thanks goes to the Leverhulme Trust for granting me a Study Abroad Studentship which has funded my time here at Tromsø. Without their support I never would have been able to come so far and experience the things that I have. Thank you!

Two people who have been supporting me since the beginning deserve my greatest thanks and the biggest hugs. My mum and dad have always been there at the end of the phone to answer when I call and they deserve to be acknowledged as a big part of the completion of this project. I look forward to explaining what all the boring bits mean when I am back home and they cannot hide behind the phone.

And finally, I would like to thank my peers here at UiT for keeping me company throughout my time here and being there to talk to through the ups and downs. A special thank you to Ana María Montaña Mónoga who has kept me company, been there for the failures and always been down to get lunch when things get difficult.

Thank you everyone, you have all had a part in this project in some way!

Georga-Marie Hooton

Tromsø, May 2024

Contents Page

1. Introduction

Submarine landslides transport large quantities of sediment from the continental shelf into the deep abyssal plain and are frequent features found through the continental margins world wide and are extremely common off the Norwegian margin (Canals et al., 2004; Winkelmann et al., 2006). Submarine Landslides are especially common in high latitude glacially dominated continental margins and are frequently found near the mouth of past ice stream glacial troughs (Canals et al., 2004).

Submarine slides are not limited to the Norwegian coast but they cycle of sediment deposition in these locations as a result of glacial ice cover is a major influence of the failure of the shelf. Reaching further into the Arctic, other mass wasting events can be found off northern Canafe (Mosher et al., 2012), Alpha Ridge (Boggild et al., 2020), Lomonosov Ridge (Kristoffersen et al., 2007) and Svalbard (Forwick et al., 2016; Vanneste et al., 2006).

The Hinlopen Slide (also referred to in the past as the Yermak Slide or the Hinlopen/Yermak Slide) is one such event located at the slope of the Northern Svalbard Margin at the mouth of the Hinlopen Strait between Spitsbergen and Nordaustlandet. It is one of the largest examples of submarine mass movement in the Arctic with a total estimated volume of 1,350 km^3 of reworked material over a total run out volume of approximately 10,000 km^3 (Vanneste et al., 2006).

Past research (Winkelmann et al., 2006) dates the slide to MIS 3 (25,390 cal yrs BP ± 220 ^{14}C years directly above the slide deposit) with core samples take from the distal part of the slide in the Sofia Basin (Stein, 2005). Winkelmann also concluded that the landslide occurred in on major event with several repeated minor events following and this is still the accepted understanding of the slope failure.

Winkelmann's dating of the slide coincides to the build-up of the Svalbard Barents Sea Ice Sheet and therefore the provided theories for the influencing factors leading to the subsequent failure corresponds with the environmental conditions of this time, such as falling sea level and changes in the Gas Hydrate Stability Zone (Winkelmann et al., 2006).

Other potential influence include tectonic activity and seismicity, glacio-isostatic processes and glacial build up or erosion (Vanneste et al., 2006).

1.1. Objectives

The purpose of this project is to investigate and date the Hinlopen submarine landslide offshore northern Svalbard by analysing two sediment gravity cores taken from the headwall area of the landslide in July 2022 onboard the RV *Helmer Hanssen*.

The main objectives of this study are to:

- Determine accurate dating of two marine sediment cores.
- Use multiproxy data (in the form of grain size analysis, micropalaeontology, X-Ray Fluorescence, Multi Sensor Core Logging data, stable oxygen, and carbon isotopes and ^{14}C AMS radiocarbon dating) to correlate results in relation to past oceanographical and environmental changes.

and

- Investigate slide morphology by the use of sub-bottom profile data.

2. Geological Setting

The northern Svalbard and Barents Shelf margin separated from the continental Lomonosov Ridge approximately 60-55Ma and marked the opening of the Eurasian Basin (Jokat., 2005). The northern Svalbard margin is located here on the Eurasia Basin section of the Arctic Ocean where the boundary is flanked by the Yermak Plateau to the west and the Nansen basin to the east.

The Hinlopen Strait separates the islands of Spitsbergen and Nordaustlandet in northern Svalbard running over 100km and extending into the continental shelf where the Hinlopen Trough terminates at the continental shelf break. Investigation into the geomorphology of the Hinlopen Strait and continental shelf indicate that the strait acted as a major route for ice movement and debris transfer during the Late Weichselian deglaciation approximately 20k cal BP (Batchelor et al., 2011). The deposition of ice and debris marks the Hinlopen Fan which is built of glaciogenic sediment and debris flow deposits and numerical ice sheet modelling (Svendsen et al., 2004) indicate glaciation ice sheets during the Weichselian extends over the shelf break which, in association with the surface geomorphology (Batchelor et al., 2011) and borehole data dating glacial deposits >2.3Ma show the area has a long history of glacial-interglacial activity (Butt et al., 2000; Knies et al., 2009).

Ice movement and subsequent sediment transportation through troughs, fjords, straits, and channels in glaciated environments result accumulated deposition in front of the stream resulting in a trough mouth fan (TMF) at the continental shelf edge. These are common along the Norwegian Margin (Bear Island TMF, North Sea TMF) and offshore Svalbard (Kongsfjorden TMF, Isfjorden TMF) and the Hinlopen Strait is no exception (Laberg and Vorre., 1993; Laberg and Vorren.,1996; Vorren and Laberg., 1997; Rydningen et al., 2015; Rydningen et al., 2016). Shelf edge propagation is visible in swath bathymetry showing sediment deposition during the late Weichselian deposited on top of the main headwall location of the Hinlopen Slide.

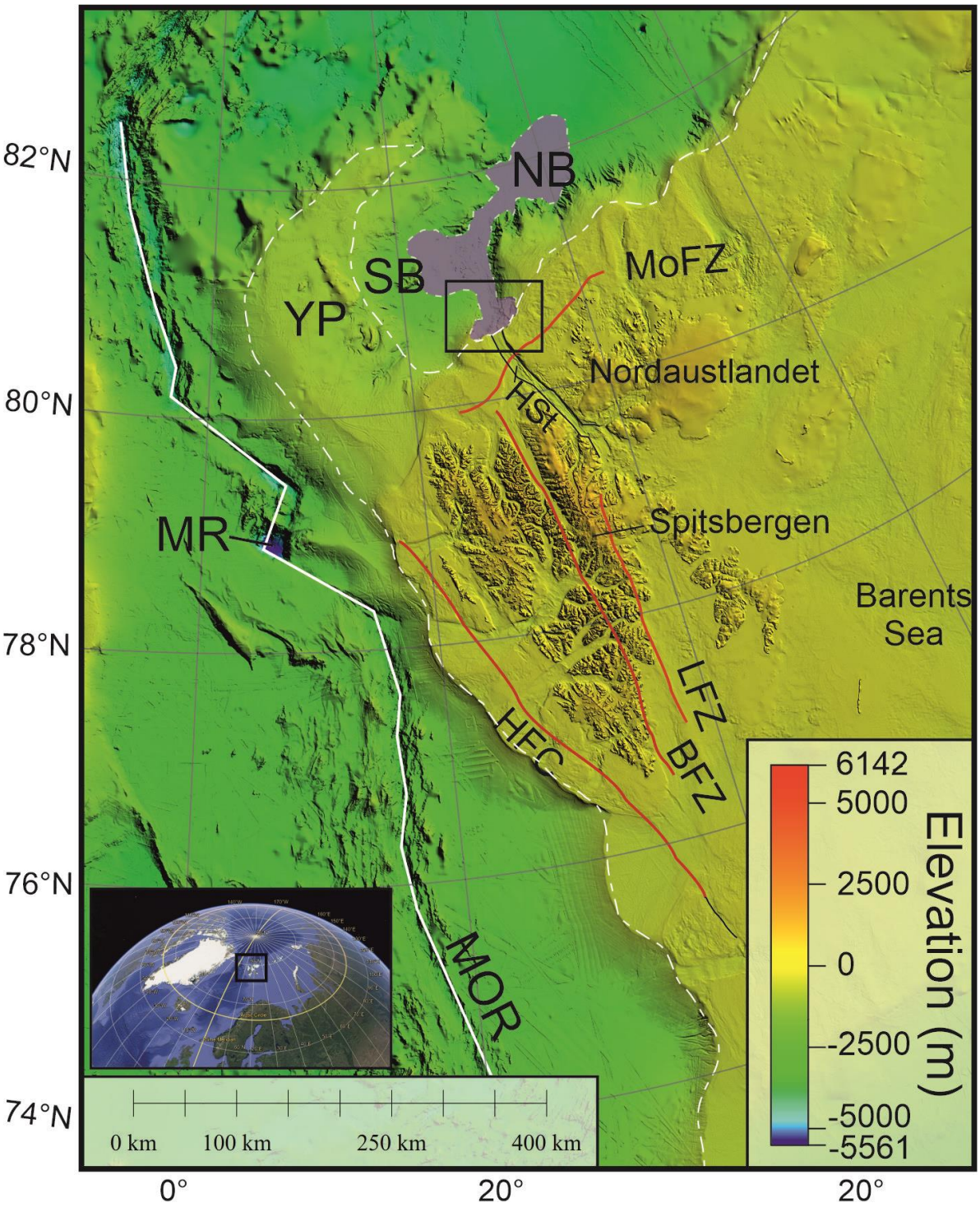

Figure 1: Map shows the location of Svalbard on a global map and the most discussed tectonic fault zones. The white dotted line marks the continental shelf edge, the purple shaded area marks the extent of the Hinlopen Slide run-out, MR = Molloy Ridge, MOR = Mid Ocean Ridge, YP = Yermak Plateau, SB = Sofia Basin, NB = Nansen Basin, HFC – Hornsund Fault Complex, BFZ – Billefjorden Fault Zone, LFZ = Lomfjord Fault Zone, MoFZ – Moffen Fault Zone, HSt – Hinlopen Strait. The black box marks the study area of the Hinlopen Slide headwall (Fig. 4) and the white dotted line marks the maximum glacier extent during the LGM. Bathymetry comes from the IBCAO Arctic Bathymetric Map (Jakobsson et al., 2020),

the fault map takes inspiration from Dallmann (2015) and the globe showing the location comes from Google Earth., (2024).

2.1. Tectonics

The Mid-Ocean Ridge (MOR) extending from the Atlantic runs along eastern Svalbard where it extends northwards past the Yermak Plateau into the Arctic (Fig 1). This marks a series of transform faults and the deepest locality in the in the Arctic Ocean, the

Molloy Ridge. The Hornsund Fault Complex is the most identifiable feature in this zone and runs along the eastern edge of Spitsbergen, formed from the separation of Svalbard and Greenland (Sundvor and Eldholm., 1976; Sundvor and Austegard., 1990; Myhre et al., 1982).

The proximity to the rifting between the Svalbard and Barents Sea margin and the Lomonosov Ridge shows a history of tectonic activity (Eiken, 1994). The rifting event itself has resulted in deep sediment faulting as the Moffen Fault, which cuts through the continental shelf on the Northern Svalbard Margin north of Spitsbergen (Eiken., 1994).

Tectonic activity on land at Svalbard presents itself in mostly a NW-SE trending pattern cutting through Spitsbergen, where the largest and most investigated fault zones are the Billefjordern Fault Zone and the Lomfjorden Fault Zone. (Fig. 1).

2.2. Oceanographical and Hydrological Setting

The North Atlantic Current (NAC) brings warm saline water from the Atlantic Ocean into the Arctic via northwards transport through the Greenland-Scotland Ridge (Fig. 2). The NAC diverges at the continental shelf of the Barents sea separating towards Svalbard along the Fram Strait into the West Spitsbergen Current (WSC) and also into the Barents Sea as the Nordkapp and Murmansk Currents. The WSC is the northmost extension of the NAC and branches in two north of Svalbard into the Svalbard branch which is responsible for bringing warm saline waters along the Svalbard Continental shelf (Koc et al., 2002) and the Yermak Branch which flows northward. The action of the NAC transporting warm water northwards plays a major role in the overall circulation of the global ocean in the form of the Atlantic Meridional Overturning Circulation (Henry et al., 2016).

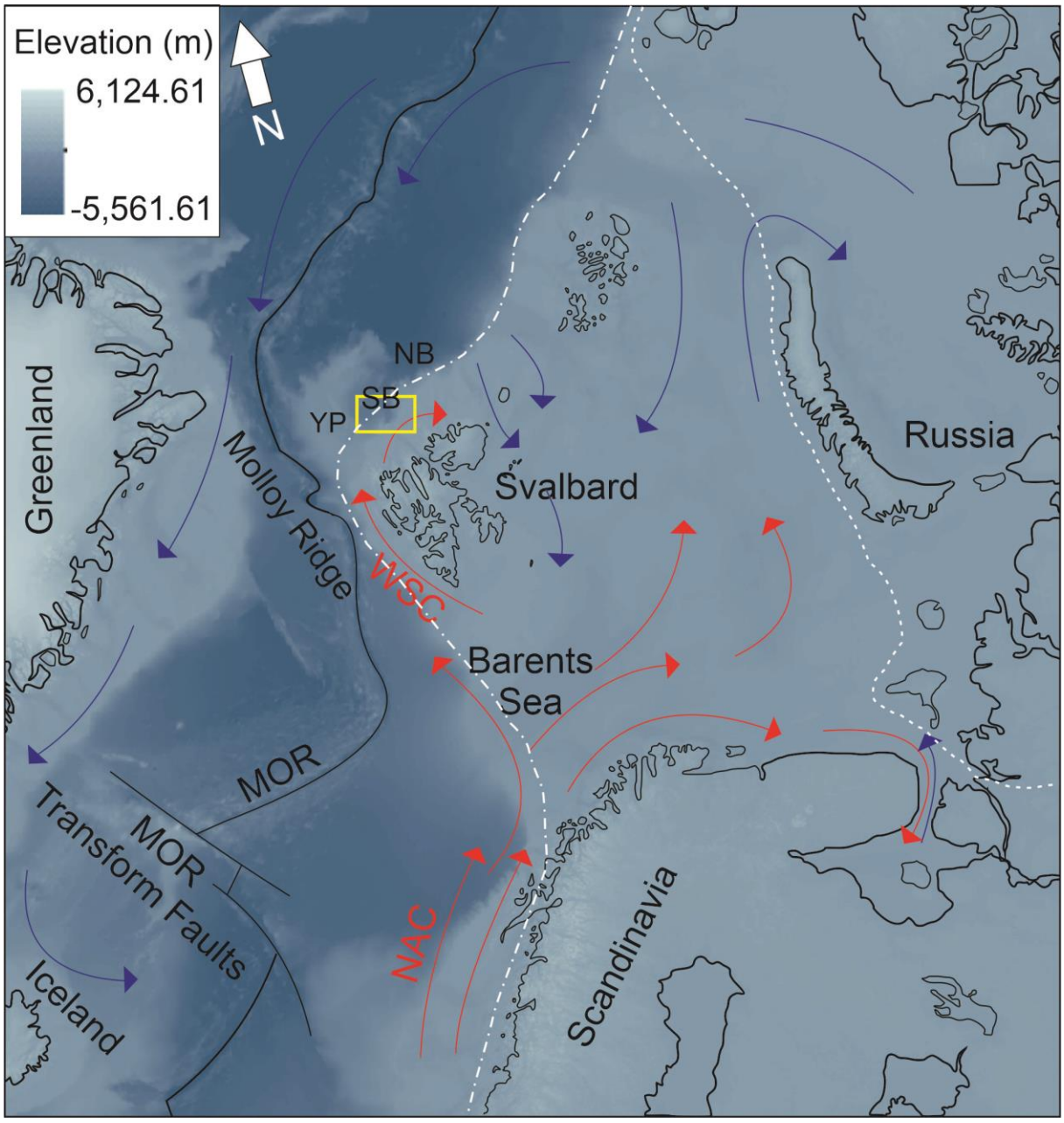

Figure 2: Map showing the ocean currents affecting the Nordic Seas and Arctic Ocean.. The red arrows indicate warm saline water, the blue arrows indicate cold fresher water. NAC = North Atlantic Current, WSC = West Spitsbergen Current, MOR = Mid Ocean Ridge, YP = Yermak Plateau, SB = Sofia Baisn, NB = Nansen Basin. The yellow box indicates the study location and the white dotted line indicates the SBSIS extent during glaciations. The bathymetry belongs to Jakobbsen et al., 2020 and inspiration was taken from AMAP (2016) and the Icelandic Marine Research Instisute (2016)

Cold Arctic water (AW) is transported from the Arctic southwards into the Barents Sea as the Persey Current (PC) (Sjundfjord et al., 2015). The PC flows eastwards along the south

of Svalbard and then north along the eastern Spitsbergen coast, resulting in clockwise circulation. Near-surface coastal waters also show a clockwise pattern.

The Barents Sea Polar Front separates the cold Arctic Water from the Atlantic Water and is influenced from a variety of factors including bathymetry, atmospheric forces, ocean circulation patterns and others (Skagseth et al., 2008).

2.3. Glacial History of Svalbard

Glaciations have been documented to have occurred on Svalbard since the onset of the Pleistocene and the islands have undergone repeated glaciations and deglaciations throughout the Quaternary. An investigation by Knies et al., (2009) based on borehole data and a chronostratigraphic record shows no indication of an ice sheet during the Late Pliocene to the Early Pleistocene prior to the onset of the Pleistocene Glaciation/Northern Hemisphere Glaciation (3.5-2.4Ma). During this time, glaciation was limited to only the mountainous regions of Svalbard but from 2.4-1Ma the ice sheet expanded and reached the southern Barents Sea. Maximum glaciation is believed to have occurred around 950ka with repeated advancement onto the continental shelf.

2.3.1. The Saale Glaciation and the Eemian Interglacial

The Saale glaciation covers a number of glacial-interglacial cycles that occurred from approximately 400-130ka cal yrs BP (Mangerud et al., 1998; Lauer and Weiss., 2018). During a large-scale glaciation event the Svalbard Barents Sea Ice Sheet (SBSIS) reached a maximum limit at the continental shelf on the western Svalbard margin which occurred at approximately 140-130ka cal yrs BP (Svendsen et al., 2004). This occurred during MIS 6 and was proceeded by the Eemian interglacial.

The Eemian Interglacial period (also referred to as the Last Interglacial) was one of the warmest climatic periods in the last 800ka years (Shackelton et al., 2020). It began at approximately 130ka BP and ranged through MIS 5e to approximately 115ka BP (Shackelton et al., 2020). During this time, sea levels were approximately 3 metres higher than they are today (Stirling et al., 1998) due to meltwater from both the West

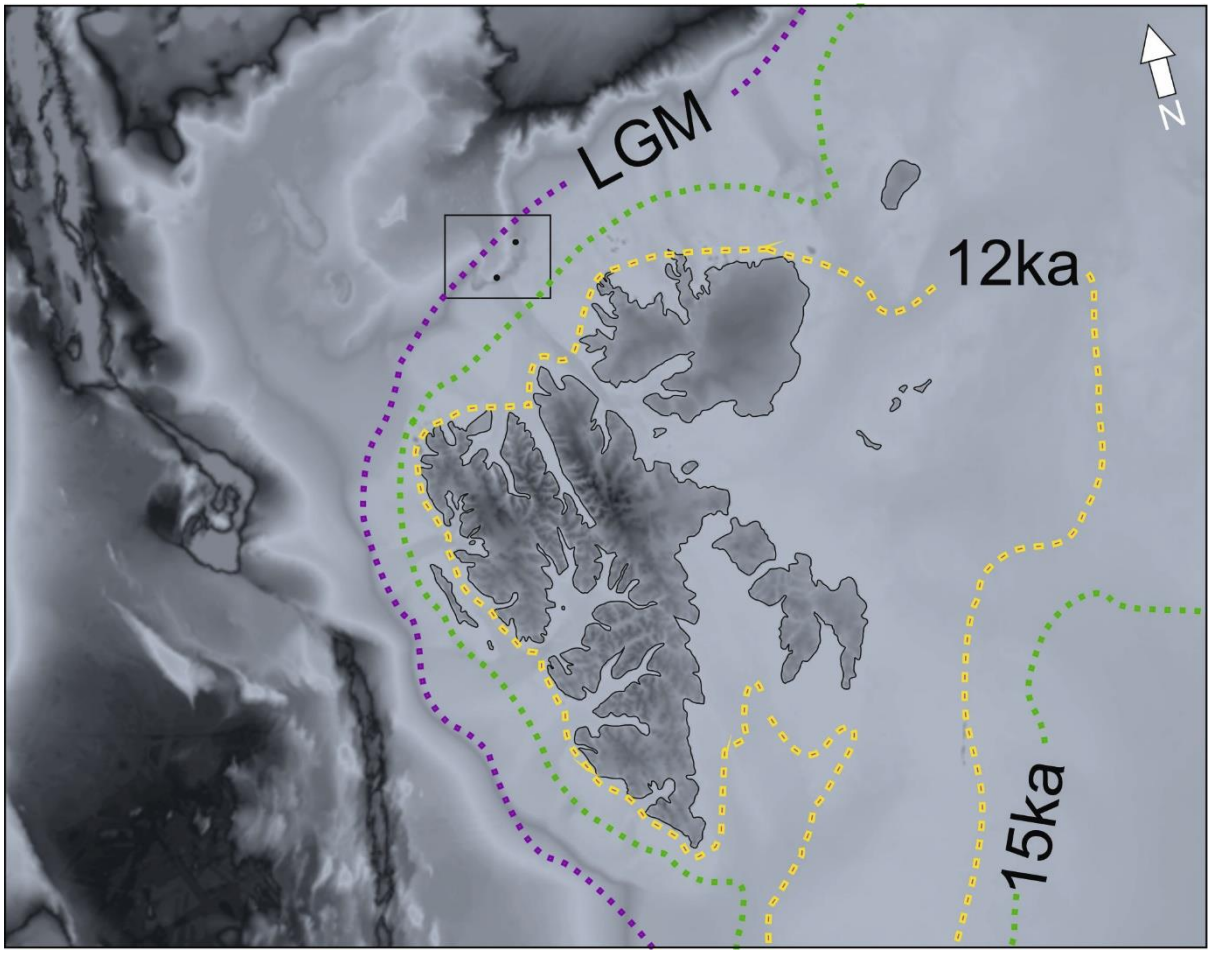

Figure 3: Map showing the extent of the Svalbard Barents Sea Ice Sheet during the late Weichselian, inspiration taken from Ingólfsson and Landvik, (2013) and Landvik et al, (1998) and bathymetry belongs to Jakobssen et al (2020).

Antarctic ice sheet (Mercer., 1978) and Greenland ice sheet (Cuffey and Marshall., 2000). The warmer conditions means that the extent of the SBSIS was substantially reduced and glaciers were of similar size to those of today (Mangerud and Svendsen., 1992). Little research has been done to investigate the extent of sea ice levels during the Eemian, and results Stein et al., (2017) simulate that seasonal sea ice cover was prominent and during the summers the Barents Sea was almost completely free of sea ice however a recent study by Vermassen et al., (2023) suggests the ice extent was substantially reduced and summer periods were likely completely free of sea ice.

2.3.2. The Weichselian

The end of the Eemian Interstadial sees the beginning of the Weichselian, which is a time period that spans from approximately 115-11.7ka and sees a repeated cycle of glacial-interglacial periods through a time known as the Last Glacial Period, falling withing the larger Pleistocene Glaciation (Ehlers et al., 2024). It is broken down into the Early, Middle and Late Weichselian which each correspond to MIS 5e-5a, 4-3 and 2 respectively. Multiple glacial events show the SBSIS reaching the continental shelf edge west of Svalbard (Mangerud et al., 1998).

2.3.2.1. The Early Weichselian

The glacial extent of the SBSIS at Svalbard during the Early Weichselian reaches the continental shelf on the western side of Spitsbergen at approximately 110ka BP as seen by glacial loading (Mangerud et al 1998). The maximum limit of the SBSIS is believed to have occurred between 90-80ka BP (Svendsen et al., 2004a;2004b); however, Mangerud et al., (1998) marks the Phantomodden Interstadial as having occurred from 107-75Ka but being a period not-completely ice free implies the non-conflicting results. In 2020, a study by Hesjedal Weiberg et al., determined that the SBSIS reached its maximum extent at 90ka BP at Kongsfjorden Trough Mouth Fan (TMF), further confirming the studies by Svendesn et al (2004a;2004b).

2.3.2.2. The Middle Weichselian

The Middle Weichselian sees the SBSIS growth once again in MIS 4, and the time it reached its maximum extent has been discussed frequently. Svendsen et al., (2004a) suggested the ice sheet reached its maximum extent at the continental shelf from 60-50ka BP whereas Hesjedal Weiberg et al., (2023) have recently suggested it occurred around 90ka BP. Both age ranges correlate with those of Mangerud et al., (1998) and with the understanding that following this glaciation period the deglaciation begins at ca. 54ka BP (Mangerud et al., 1998; Hesjedal Weiberg et al., 2023) it is possible that it could have occurred earlier during this time range as the deglaciation period is now believed to have occurred rapidly. This deglaciation is known as the Kapp Ekholm Interstadial from the

location of Radiocarbon dates taken from Kapp Ekholm, Svalbard and occurred during MIS 3 (Mangerud et al., 1998). A layer with a high influx of IRD was investigated by Hesjedal Weiberg et al., (2023) at Kongsfjorden TMF occurring from 38-34ka BP with an unknown ice extent and Svalbard glaciers began their growth again at approximately 32ka BP (Landvik et al., 1998).

2.3.2.3. The Late Weichselian

The Late Weichselian that is characterised by the last glacial period of the Last Glaciation and occurred during MIS 2. The growth of the ice sheet began at the end of the Middle Weichselian and the maximum ice extent once again reached the continental shelf edge west of Svalbard (Svendsen et al., 2004a;2004b) and therefore inferred to have reached the continental shelf completely surrounding the archipelago. The date for when the ice sheet reached the shelf edge has been debated, newer studies, Jessen et al., 2010 and Hesjedal Weiberg et al., 2023, put the glacier reaching the shelf edge at 20ka BP and 24ka BP respectively. Mangerud et al., (1998) gives an age range for maximum glacial extent to 20-15ka and Salvigsen and Nydal (1981) dates it to 18ka. The idea that the glaciation was at its maximum extent at around 15ka BP is challenged by the acceptance of a rapid deglaciation event occurring over a centennial- possibly even decadal- scale from 15-14ka in an event known as the Bølling Allerød (B-A) Interstadial (Johnsen et al., 1992; Sierstad et al., 2005; Jessen et al., 2010). The B-A Interstadial was the first warming event of the deglaciation and during this time, where seismic and sediment core investigation showed a major outlet glacier reached the shelf edge (Svendsen et al. ,1192) during the Last Glacial Maximum, by 14.1ka BP research has found that the mouth of Isfjorden on western Spitsbergen was deglaciated and that final glacial retreat there occurred at 11.3ka (Svendsen et al., 1996) (Fig. 3).

2.3.3. The Holocene

Following the B-A Interstadial came the rapid onset and offset of the Younger Dryas, a cooling event that occurred from ca. 12,900-11,700ka BP (Allaart et al., 2023; Ebbsen and Hald., 2004). It is the last cold period at the transition into the Holocene and was likely

the result of freshwater input into the Atlantic Meridional Overturning Circulation resulting in weaker transport of warm water (Allaart et al., 2023).

2.4. Landslides

The Norwegian Margin marks a long line of submarine landslides of deposited sediment into the Norwegian and Barents Sea. Landslides stretch from offshore southern Norway all the way into the high-latitude Arctic and northern Svalbard. Continental ice sheets during past glacial events extended across northern Europe, branching from northern Norway down to southern United Kingdom, reaching out past the continental land mass towards the continental shelf where the ice sheet terminated.

This location for ice masses and the glacial-interglacial cycles occurring frequently throughout time has allowed for conditions resulting in the frequent failures of the shelf leading to a magnitude of submarine landslide events. This includes rapid sedimentation and excess pore pressure, which, when occurring together allow for an easier event of failure along a slide plane.

2.4.1. The Storegga Slide

The largest known exposed submarine landslide is the Storegga Slide, found in the Norwegian Basin this slide was a series of events occurring around 8,200 cal yrs BP and resulted in the transportation of approximately 2,400 to 3,200 km^3 of sediment (Haflidason et al., 2005). The area has been had multiple failures dating back to the early Pleistocene, the oldest, Slide W, dating to 1.7 ma (Solheim et al., 2005). The trigger for the Storegga Slide is still unknown (Zhu et al., 2023) however it is believed to be a combination of repetitive rapid deposition during glacial events as well as low inclination and rapid pore pressure mixed with a marine clay and glacial sediments, which act differently when put under pressure and play as an additional factor to creating areas of weakness and subsequent failure (Kim et al., 2019).

The Storegga Slide generated a tsunami, reaching from Northern Scotland (Smith et al., 2004), Norway (Bondevik et al., 1997) and potentially reached all the way to Greenland

(Wagner et al., 2006). The extent of the tsunami is known from marine deposits and organisms found in freshwater and terrestrial locations as well as tsunami deposits in coastal freshwater lakes.

2.4.2. Trænadjupet Slide

Also along the Norwegian margin is the Trænadjupet Slide, found northwards of the Storegga Slide and dates to approximately 4,000 ^{14}C yrs BP (Laberg and Vorren., 2000a). This event covered an area of approximately 14,100 km2 and the failure is understood to have been caused by a combination of high sedimentation rates preventing gas and water to escape and an eventual build-up of pore pressure and a final trigger resulting from a series of earthquakes that occurred associated with the Fennoscandinavian uplift (Gudmundssen,1999).

2.4.3. Andøya Slide

A third large slide occurred along the Norwegian continental slope during the Holocene and that is the Andøya Slide. Covering an approximate area of 9,700km^2 the slide is believed to have been triggered by earthquake activity sometime during the Holocene and, following the Storegga and Trænadjupet Slides, is the third largest submarine landslides offshore western Norway which all occurred in the past 10,000 years (Laberg et al., 2000).

2.4.4. Other Landslides along the Norwegian Margin

There are many submarine landslides off the Norwegian Margin and reaching up to the Fram Strait. Some predate the Holocene, for example Bjørnøyrenna Slide (younger than 330,000 yrs) is inferred to have also been triggered by increased sedimentation combined with tectonic activity (Laberg and Vorren, 1993), Slide W (Solheim et al., 2005), and Bear Island Slide (Laberg and Vorren, 1993), smaller landslide events are also common: Sklinnadjupet Slide (Rise et al., 2006; Rise et al., 2010), Nyk Slide (Lindberg et al., 2004), Fugloy Bank Slide complex (Taylor et al., 2003) and Finneidfjord (Longva et al., 2003), the latter of which being the most recent to scale, occurring in 1996.

2.4.5. Landslides in the Arctic

A variety of submarine landslides and mass wasting events can be found throughout the Arctic. Large scale mass-wasting events occurred in the high latitude Arctic, one most famous example being the Lomonosov Ridge wasting event dating from the mid Miocene to mid Pliocene in age (approximately 15Ma to 4.5Ma (Schlager et al., 2021). This landslide event is interesting as it is not believed to have had any glacial influence causing the failure event. The current understanding being that the instability leading to failure was caused by earthquake loading, however in past studies the hypothesis that the instability was the result of a shock- or pressure-wave as a result of high intensity impact somewhere in the Arctic (Kristoffersen et al., 2007).

This was also a hypothesised trigger mechanism for another mass wasting event in the Arctic located at Alpha Ridge, which extends from the Canadian Arctic Archipelago into the Arctic Basin. There is no clear age for this wasting event to date, and a confident trigger or failure mechanism has not been determined beyond basement tectonics and the possible influence of extraterrestrial impact nearby in the Arctic (Kristoffersen et al., 2009).

2.4.6. Landslides offshore Svalbard

The Fram Strait Slide Complex is an area located off western Svalbard The youngest slide in this location is dated to 60k cal yrs BP and the oldest occurred >2.58Ma (Elger et al., 2014). The failure mechanism of this event was not the result of glacimarine deposition, as many other slides offshore Norway have been discussed. These events are understood to be a combination of, or solely related to contour currents, tectonic faulting, and other influences from high-degree pressure as a result of the gas hydrate system offshore Svalbard (Elger et al., 2014).

2.5. Study Area

2.5.1. The Hinlopen Slide Morphology

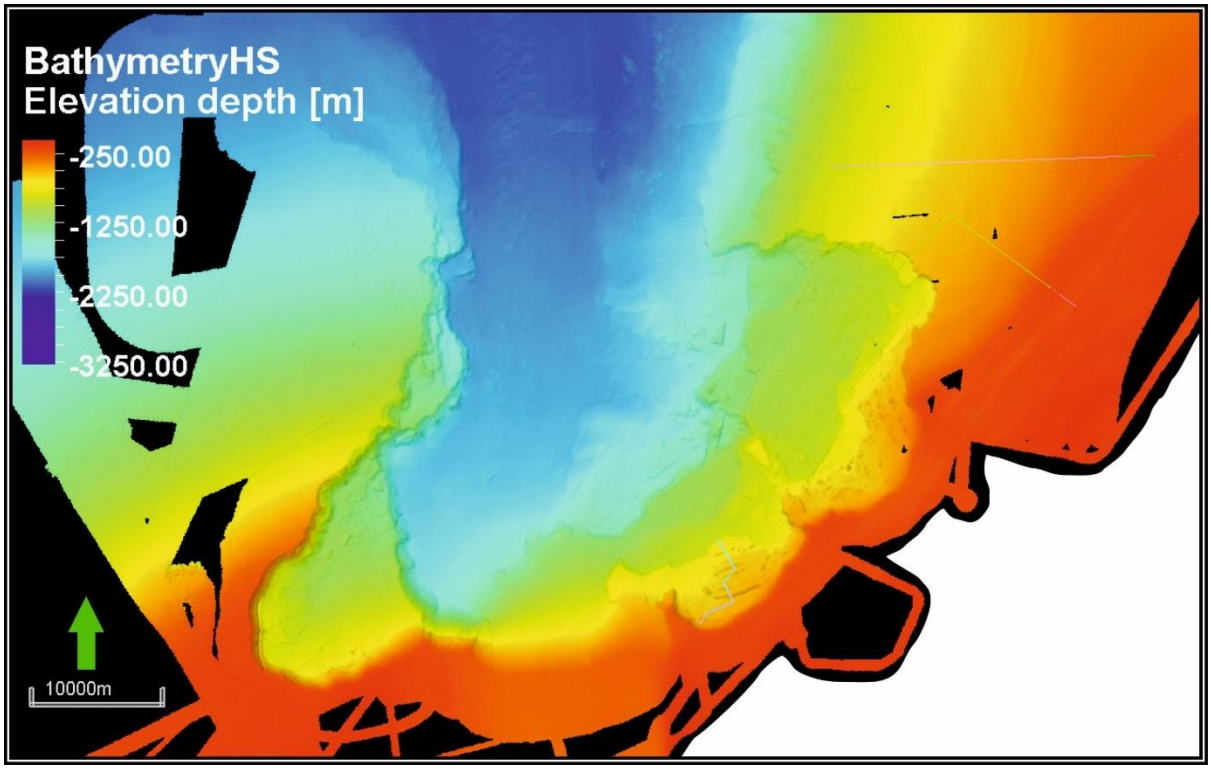

Figure 4: Swath bathymetry map showing the study location at the headwall area of the Hinlopen Slide, the location of this figure can be found in Figs. 1, 2, and 3.

The Hinlopen Slide was first reported in 1999 using single-beam echo sounding and side-scan sonar (Cherkis et al., 1999) and investigation using swath bathymetric data has allowed for a higher degree of investigation to analyse the geomorphological characteristics and run-out area of the landslide (Vanneste et al., 2006). The content of slide deposit was mostly Plio-Quaternary sediments consisting of stacked glaciomarine deposits (Eiken, 1994; Geissler and Jokat, 2004) and trough mouth fan deposits from former glacial intervals (Vanneste et al., 2006; Batchelor et al., 2011).

The slide itself has been characterised into four main subdivisions of morphological zones (Vanneste et al., 2006); the headwall area, the upper slide area, the intermediate slide area, and the distal slide area.

2.5.1.1. Headwall Area

The headwall area is approximately 120km in length shaped in an amphitheatre structure (Cherkis et al., 1999). The headwall of the landslide occurs at a water depth ranging from 200-500m and has a width stretching to approximately 58km at its widest and narrowing to 20km downslope in a bottle-neck formation (Fig. 4). The headwall scarps are steep (30°, Vanneste et al., 2006) and range in height from approximately >1,000-200m. Vanneste et al (2006) further divides the area into the western headwall area and the eastern headwall area and Hogan et al (2013) combines this with the intermediate slide area.

2.5.1.1.1. Western Headwall Area

The western headwall area has a gullied sidewall approximately 600m high leading into a flat depression 12km wide and dips around 3° before further dropping another 600m into the deepest surface in the headwall area. This area contains some isolated slide blocks and debris which indicate it was properly evacuated during the failure event along a slip surface (Vanneste et al., 2006). Further to the east is the scarp in front of the Hinlopen Trough which shows post slide sediment infill forming a young trough mouth fan.

2.5.1.1.2. Eastern Headwall Area

The eastern headwall area has a more complex morphology, showing multiple separate backscarps with smaller detachment surfaces separated by steep sediment walls. Separate elongated blocks or ridges over several thousand metres in length and varying in height approximately 150m but decreasing with distance from the headwall (Fig. 4 and 9). The furthest east shows many detached ridges protruding from the seafloor and a hummocky seabed morphology containing slump debris and slide blocks (Vannest et al., 2006; Winkelmann et al., 2008).

2.5.1.2. Intermediate Slide Area

The intermediate slide area is approximately 60km downslope of the main headwall and extends past the headwall bottleneck. Here the morphology shows several debris lobes, slump deposits and enormous rafted blocks (Vanneste et al., 2006; Winkelmann et al., 2008).

2.5.1.3. Distal Slide Area

Lastly, the distal slide area is further downslope from the intermediate slide area and has a hummocky surface which smooths out as the runout distance from the slide increases (Vanneste, et al., 2006) and shows a debris flow-like appearance (Winkelmann et al., 2008). The complete extent of the Hinlopen Slide continues into the Nansen Basin some 200km from the shelf break at a water depth >2000m.

3. Methods

In a research cruise to Svalbard in July of 2022 aboard the RV Helmer Hanssen, with assistance of the Alfred Wegener Institute (Helmholtz Centre for Polar and Marine Research, Bremehaven, Germany), Inha University (Incheon, South Korea), the Korean Polar Research Institute/KOPRI (Incheon, South Korea), Korea University (Seol, Korea) Geologiska institutionen Lunds universitet (Lund, Swedes), Marum – Centre for Marine Environmental Science University of Bremen (Bremen, Germany), NGU – The Geological Survey of Norway (Trondheim Norway), University of Tromsø - The Arctic University of Norway (Tromsø, Norway) and UNIS- The University Centre in Svalbard (Longyearbyen, Svalbard). variety of sediment gravity cores, seismic and acoustic data was collected at the mouth of the Hinlopen Strait at the headwall location of the Hinlopen Slide. Two sediment gravity cores have undergone a multiproxy investigation for the purpose of this project, as well as radiocarbon and isotope analysis. The specifics of each method is outlined in the following section of the report.

3.1. Bathymetry

Bathymetric data provides an insight to the seafloor characteristics in the chosen study location. The data used in this project belongs to the open access databases IBCAO (Jakobsson et a., 2020) database. This investigation will be looking into the main headwall and runout area closest to the mouth of the Hinlopen Strait. This data has been projected with the Schlumberger software Petrel (2023) to assist with acoustic investigation.

3.2. Acoustic Investigation – Sub-Bottom Profiles

Mapping of the Hinlopen Slide requires Sub-Bottom Profile (SBP) acoustics in order to investigate the characteristics of the seafloor. A Sub-Bottom Profiler is a sonar system which emits low frequency acoustics towards the seafloor while aboard a vessel using a transducer. The acoustic waves travel through the water column and at the seafloor some are reflected back to a receiver and others penetrate the substrate and are then reflected back.

The data is measured in Two-Way-Travel (TWT) time, which is a result of the waves having to travel through the water column, hit the substrate and then travel back through the water column to the receiver. Different sediment types and composition can affect the amount of time it takes for the waves to be reflected back and so when the data has been collected and processed it creates a cross section of the seafloor following the path of the ship.

SBP data was collected aboard the 2022 research cruise using an *Innomar Deep-36 Parametric Sub-Bottom Profiler* which has a water depth range of 5-6,000m below the transducer, can penetrate up to 150m (dependant on noise and the type of sediment being penetrated) and has a primary frequency of 36kHz and a secondary frequency range of 2-7kHz (Innomar., 2024).

The resulting SBP lines have been investigated and analysed using The *Petrel Subsurface Software* to amplify and identify seafloor and sub-seafloor features, the results of which will be disclosed in Section 4.4.1.4. of this report. Overall, the SBP data identifies seafloor characteristics nicely and, in some locations, provide a nice view into the sub-seafloor sediment transitions. However, the quality of the data leaves areas open to interpretation, specifically at the headwall scour and slump deposits.

3.3. Sediment Gravity Coring

A total of nine sediment gravity cores were collected in the Hinlopen Slide area, this project will investigate two of these: IG22-1_KOREA-HH-1168 (referred to throughout this text as Core 1168) and IG22-1-KOREA-HH-1192 (referred to throughout this text as Core 1192 (Table 1). A gravity corer is used which allows for sediment sampling in deep waters. A plastic liner is fitted to the corer and with the help of gravity and a 1,900kg weight is it released overboard and penetrates the seafloor. The sediment is collected in the plastic liner and transported back on board where it is then cut into approximately 1m lengths. The ends of the sediment are stuffed with foam to remove the possibility of disturbing the material inside and sealed with plastic caps and waterproof tape to reduce the likelihood

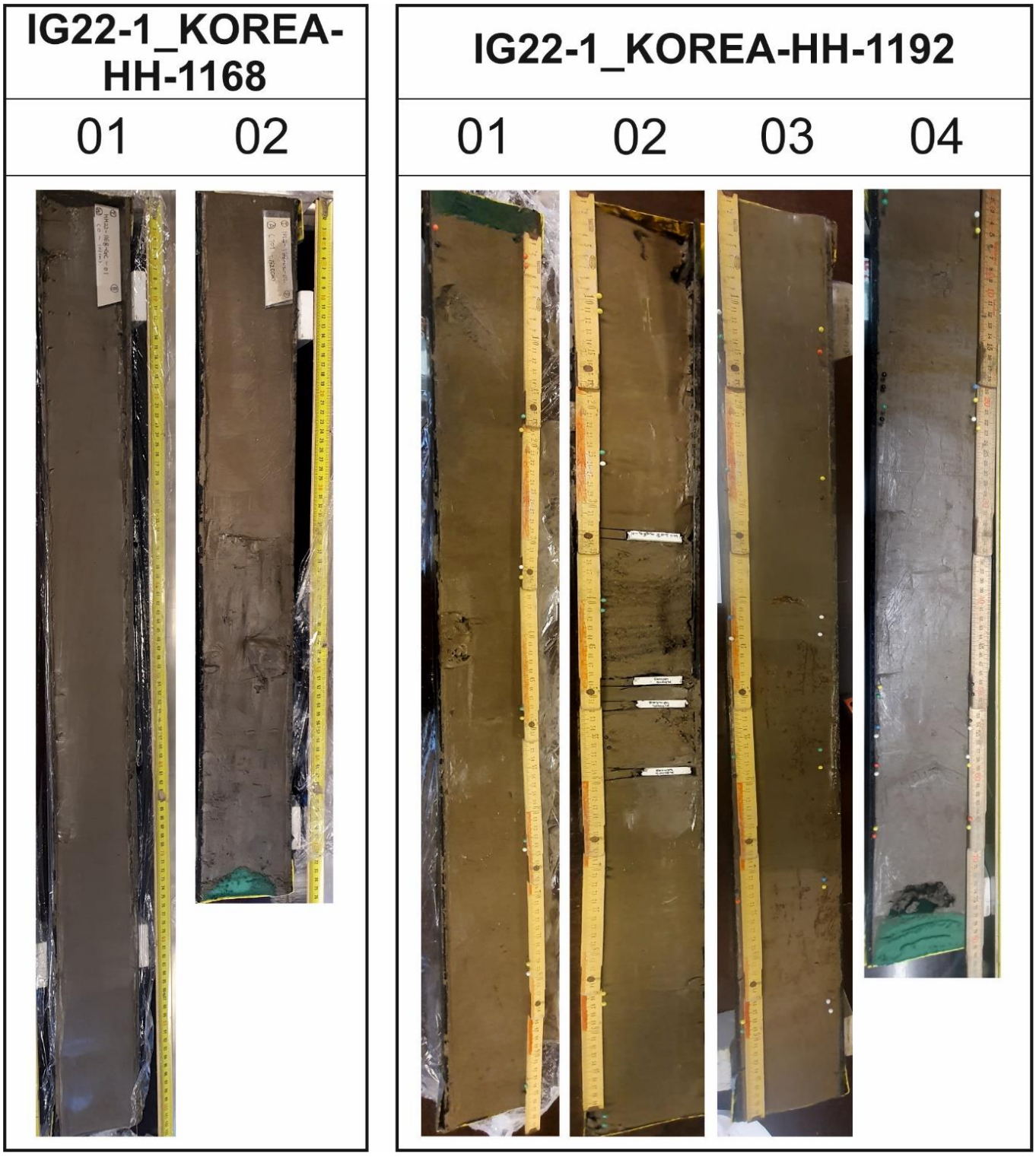

Figure 5: Photographs taken with a mobile camera after splitting and before sampling for sediment. The small pins in Core 1192 are placeholders to mark where samples may be taken and the white polystyrene marks samples taken from the Korean Polar Research Institute in December of 2022.

Core	Latitude (N)	Longitude (E)	Water Depth (m)	Recovered Length (cm)	Location
IG22-1_KOREA-HH-1168	80°43.466’	016°18.686’	523	198	Elongated block, South Headwall Area
IG22-1-KOREA-HH-1192	80°53.508’	016°49.175’	988	383	Slump Deposits, North-Eastern Headwall Area

Table 1: Core ID locations, water depth and recovered lengths from the July 2022 research cruise aboard the RV Helmer Hanssen.

of water seepage. The top and bottom of each core is clearly marked as well as the station number and the length of the core.

The cores were stored in a cooler at 4°C aboard the vessel and transported to NGU in Trondheim where they underwent non-destructive elemental analysis (further information can be found in Section 3.2.2 of the report).

The cores were then cut in half using a core splitter, which uses a sharp blade to cut through the plastic core liner on opposite sides of the core. After this, a clean flat blade was used to cut through the sediment within, resulting in two halves sliced nicely down the centre. One half of the core is used as a working core (where samples are taken from) and the other half is kept as an archive core (stored for the potential of future analysis), the samples from this project have been collected from the working core.

3.3.1. Core Analysis

3.3.2. Non-Destructive Investigation and Analysis

Soft sediment and elemental analysis were undertaken on the split cores by using the GEOTECK Multi Sensor Core Logger (MSCL) (Fig 5). This equipment was also attached to record X-Ray Fluorescence and Photographic Imaging.

3.3.2.1. Multi Sensor Core Logging

Soft sediment properties were analysed in both cores using the GEOTEK Multi Sensor Core Logger (MSCL) (Fig. 6). The soft sediment properties analysed for this project are magnetic susceptibility, fractional porosity and wet bulk density, however other physical properties can also be recorded. The cores were loaded onto the MSCL which pushes the core horizontally beneath the stationary sensors in 0.5cm intervals using a heavy-duty core pusher.

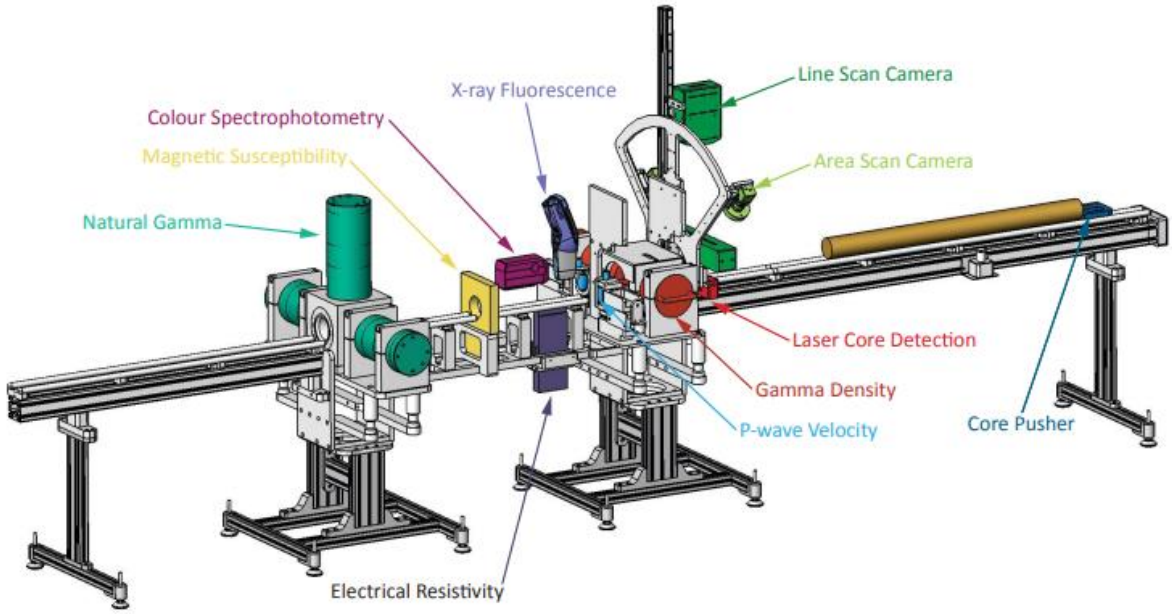

Figure 6: The GEOTEK Multi Sensor Core Logger, labelled with equipment used for different analysis techniques (GEOTEK Ltd, 2016).

3.3.2.1.1. Magnetic Susceptibility

Magnetic susceptibility shows the amount of magnetism a material has when responding to a controlled magnetic field. The presence of magnetic material is amplified in response to the applied magnetic field and can be recorded and as such, material that is diamagnetic gives a low recording response. A GEOTEK MS2E Point Sensor was attached to the MSCL and in 0.5cm intervals the sensor was lowered onto the surface of the core and measurements were digitally recorded.

3.3.2.1.2. Wet Bulk Density

The density of material involves the ratio of mass to volume of a material, the bulk density is used in reference to sedimentological analysis. The recordings of bulk density rely heavily on the material being analysed and its internal mineralogy as well as the degree to which the material is compacted.

The process is involves using a small Cs-137 gamma source and detector that align with the centre of the sediment core. A beam of gamma ray is emitted and passes through the core and are recorded in the detector, the number of photons emitted is known and therefore the number that pass through the core determines the density of the material in the core.

3.3.2.1.3. Fractional Porosity

The fractional porosity tells us the porosity of the sediment core, measuring the voids in each measurement as a fraction of the total volume. It is reliant on the measurement of the sediment density mentioned previously. It works under the assumption that the sediment is fully saturated (with water, air etc.) and that the mineral grain density and fluid density is known (GEOTEK, 2016). The fractional porosity is then calculated with the following equation, where FP is the fractional porosity, MGD is the mineral grain density, GD1 is the gamma density and WD is the fluid phase density:

$$FP = \frac{MGD - GD1}{MGD - WD} \quad \text{(i)}$$

This equipment is attached to the MSCL and as such is measured in the same way, horizontally along the belt pushed in 0.5cm intervals through the sensor.

3.3.2.2. Line Scan Imaging

A Geoscan V colour line-scan camera is attached to the MSCL to produce high quality images of the sediment cores. The camera works in synchronisation with the timing of the core pusher and takes an image as a line across the core directly beneath the camera. The result of this is so that there is no distortion resulting from the camera lens.

Digital imaging is used to identify internal characteristics or structures inside of the core. It is also useful when taken directly after core-splitting as in can then be used to take into account any discolouration or changes that could occur once the sediment is exposed to the air.

3.3.2.3. X-Ray Photography, Radiographs

The internal structure of the sediment cores can be investigated without disturbance through the use of X-ray photography. This can tell us about sub-surface structures, such as bedding and lamination, contact boundaries, bioturbation, Ice-Rafted Debris (IRDs), shells and a variety of other features. Both cores were x-rayed from a variety of angles using a Thermo Kevex PSX10-65W-Varian2520DX camera and Beryllium as a source. The machine emits strong x-rays through the sediment core and the resulting x-rays are picked up by a detector beneath.

The core is laid horizontally beneath and moves beneath the x-ray camera in 0.5cm intervals and, much like the digital line scan imaging process, takes snapshots of the material directly beneath the camera which it the combined into one mosaic image giving a high-resolution internal image.

The resulting image is a contrast of high- and low-density resolution, where low density is signified by a darker signature in the x-ray image and the high-density measurements are lighter in colour (Fig 7).

3.3.2.4. X-Ray Fluorescence Analysis

X-Ray Fluorescence (XRF) spectrometry is an analytical technique to measure secondary radiation (fluorescence) to identify the elemental abundance throughout a sediment core. A handheld Olympus DELTA Premium HHXRF Handheld Spectrometer is attached to the MSCL and the core passes beneath.

To prepare for scanning, the surface of the core is cleaned carefully and a thin film of Prolene laid on top and pressed down gently to remove any air trapped beneath. This film is 4µm thick and acts to remove the possibility of contamination as the handheld sensor makes contact with the surface of the core.

The process works by using high energy primary X-ray photons to stimulate electrons that are in the sediment (GEOTEK., 2016). The primary photons knock the electrons out of their inner orbitals and the vacancies left behind leave the shells unstable. An outer orbital electron will fill the vacancy to become stable and as this outer orbital electron changes place it emits a secondary x-ray photon. This secondary photon is specific to each individual element and is the recorded fluorescence, it is displayed as peak and height intensity at each point along the sediment core (GEOTEK., 2016).

The recorded elemental intensities leave open a margin of error, and to limit or remove this, the elemental XRF data is shown as ratios instead. These elemental ratios can be used as proxies to identify changes in environmental factors and material input in marine environments (Rothwell., 2008). The ratios are also presented as log-ratios (Weltje and Tjallingii., 2008).

There are some elements which are common in marine sediment cores which can help us to investigate environmental reconstruction, such as Ca, Fe, Ti, and K. To investigate further the following log-ratios have been used in this project: Ca/Fe, Ca/Ti, Ca/Si, Ca/K, Ti/Al, Zr/Al, and Si/Al.

The ratio of Ca/Fe has been used as it offers a good proxy for discerning between glacial and interglacial cycles due to warmer conditions resulting in the deposition of sediment

with higher carbonate contents than during colder periods (Balsam and McCoy., 1987). It can also be used to determine between turbidites and pelagites as there is usually a higher abundance of Fe in turbidite deposits compared with Ca in relation to the pelagic material (Rothwell et al., 2006).

The ratio of Ca/Ti has been considered as a palaeoenvironmental proxy as it can be used to determine terrestrial versus marine biogenic material. Ti is typically a result of terrestrial sedimentation and higher level of Ca in an indication of higher marine productivity (Ingram et al., 2010). It can also be used to indicate changes in temperature.

Other ratios that can distinguish between terrestrial and marine sediment is the Ca/Si rand Ca/K. Again, Si and K are common terrigenous elements and so the ratio of them to Ca can be a good indicator of marine to terrestrial input (Rothwell and Croudace., 2015). Ca/Si can also be an indicator of water temperature change, as seen in lake sediments from Jouve et al., (2013).

There is also the potential to scan the sediment to determine grain size fractions. These can be used in conjunction with other methods in this study. The elements Zr, Ti, and Si are all common in material with a larger grain size, for instance Si is commonly in sediment cores as the result of quartz which has a high hardness level and therefore does the minerals are typically larger as they can be transported further without eroding. This is also similar to Zr which is usually in sediment cores as Zircon which also has a high hardness level (Calvert and Pendersen., 2007).

3.3.3. Destructive Investigation and Analysis

3.3.3.1. Sampling

Sampling of the two sediment cores were taken at intervals down core. Samples of 1cm thickness were taken at intervals of approximately 15cm downcore (Fig. 7).

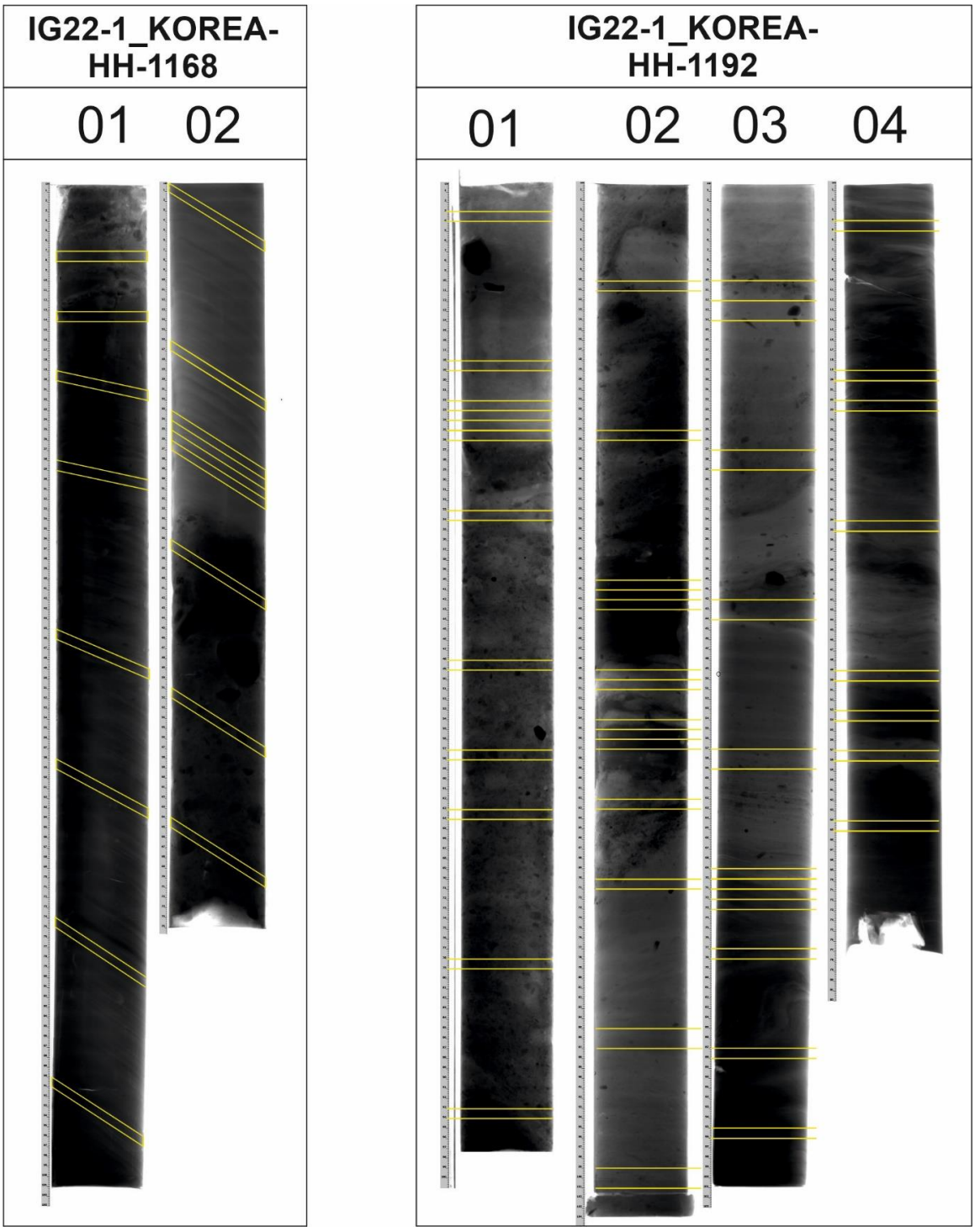

Figure 7: Xray imagery of both sediment cores showing the depth at which samples were taken for later study.

3.3.3.1.1. Sampling: Core 1168

Core 1168 differs from the other core as it was disturbed during coring, as shown from the angle of lamination increasing downcore. This is not related to sediment deposition and is solely a result of coring and so samples were taken following the lamination in the core X-ray. Samples were taken in 1cm thick slices however as the entire core had been disturbed the 1cm edge that was left behind for the previous core was included in the sample.

3.3.3.1.2. Sampling: Core 1192

For Core 1192 samples were taken mostly at the previously mentioned intervals, however multiple samples were taken in 1cm thick slices whilst leaving the 1cm to the edge of the core liner to account for disturbance for coring. This was done for approximately 5cm above the landslide deposit to account for errors or poor samples and to ensure back up samples as access to the cores was limited to two instances across the duration of this project.

3.3.3.1.3. Storage, Drying, Weighing and Sieving

The samples were weighed then stored in the freezer at the Department of Geosciences, University of Tromsø and were then freeze dried for a minimum of 24 hours. Once removed from the freeze-dryer the samples were weighed again to calculate the wet-weight abundance and then sieved through three sieves of different mesh sizes. The size fractions of the sieves were 500µm, 100µm and 63µm with warm clean water and stored at 40°C for a minimum of 48 hours and then weighed again to determine the fraction weights for sediment grain size analysis.

3.3.3.1.4. Grain Size Analysis

After the samples have been dried and weighed the samples can then undergo a simple grain size analysis. The process is as follows:

$$wet\ weight\ (g) - dry\ weight\ (g) = water\ content\ (g) \quad \text{(ii)}$$

$$(63 - 100\mu m\ fraction) + (100 - 500\ \mu m fraction) + (> 500\mu m\ fraction) = sampled\ weight\ (g) \quad \text{(iii)}$$

$$dry\ weight - sampled\ weight = < 63\mu m\ fraction\ weight\ (g) \quad \text{(iv)}$$

The size fraction of 100µm was chosen to pick for benthic and planktic foraminifera which were then used for ^{14}C AMS radiocarbon dating, $\delta^{13}C$ and $\delta^{18}O$ isotope analysis, and identification for environmental correlation.

3.3.3.2. Foraminiferal Investigation

Using the 100-500µm size fraction the samples were picked for foraminifera for identification to correlate with past environmental changes to help to constrain the landslide deposit and to see if any known environmental changes could be related to species change downcore.

For samples with a small 100-500µm fraction, the whole sample was evenly spread across a picking tray and the total number of foraminifera were counted. For larger samples, the samples were split using a Sample Splitter to obtain a usable size fraction. Then, the split sample was evenly spread across the picking tray and a minimum of 250 individuals was picked for each sample (note: some samples resulted in less than 250 individuals due to the size of the sample being picked from or the low foraminifera count in the fraction).

Benthic and planktic specimen were picked and identified down closed to species level using a variety of identification sources, including Orbigny (1826) and Kireenko et al

(2022) and specific original references to specific species have been referenced as mentioned in the results and discussion section of this study.

3.3.3.2.1. Foraminifera for ^{14}C AMS Radiocarbon dating

Foraminifer was picked from the 100-500µm fraction to collect intact and well-preserved specimen of *N. pachyderma* from pre-decided depths. Either a fraction of a sample or the entire sample (depending of the size of said sample) was sorted through for intact individuals which clearly showed the coiling direction of their chambers and no presence of sediment still remaining around the aperture (an indication that there is sediment within the test and could then affect the results of dating). These samples were then packaged into glass vials and shipped off to the MICADAS lab at the University of Zurich for ^{14}C AMS radiocarbon dating.

3.3.3.2.2. Foraminifera for Stable Isotope Analysis

Similar to the previous section, foraminifer of the same fraction size was investigated to look for species which would be useful for stable isotope analysis. Modern analysis means that smaller samples can still be accurately tested and that proved a good thing for this project as samples that contained higher numbers of specimen that would be suitable for dating did not have the best-preserved specimen. Thankfully, in every sample to be investigate there was at least one species (in Core 1192) showing good preservation in a number suitable for testing. Core 1168 proved to have better luck where only on species was needed.

3.3.3.2.3. Foraminifera for Identification

In every sample, an attempt was made to collect 250 benthic individuals whilst also collecting all the planktic specimen that were present in those same sample fractions. This was not possible in every sample, either due to small sample fractions or low foraminifera counts within larger fraction sizes. The foraminifera were separated benthic-planktic and then identified down to species level when possible.

3.3.3.3. Stable Isotope Analysis

The calcium carbonate foraminifera tests that are collected for analysis can provide a variety of useful information regarding the reconstruction of past environments, climates and changing conditions. The information determined for this project is regarding the stable isotopic analysis of $\delta^{18}O$ and $\delta^{13}C$.

Foraminifera samples were taken from both Core 1168 and Core 1192. They were taken at equal intervals of approximately 15cm in Core 1168 and similar ranges above and below the disturbed material in Core 1192. Samples were only taken in Core 1192 up to 286cm due to limited funds and also the presence of potentially disturbed material towards the base of the core which would not have given reliable results which could be correlated to a trustworthy source.

In Core 1168 the foraminifera species *Cassidulina reniforme* were measured in every sample, however due to the quality of individual species and a necessary weight limit, the species of foraminifera in Core 1192 included *Melonis barleeanus, Cassidulina reniforme, Cassidulina neoteretis* and *Nonionellina labradorica*.

Samples were sent to the *Facility for advanced isotopic research and monitoring of weather, climate, and biochemical cycling* (FARLAB) at the University of Bergen. Here samples were analysed using a Thermo Scientific MAT253 and Online Kiel IV Carbonate Device to acquire $\delta^{18}O$ and $\delta^{13}C$ measurements simultaneously.

3.3.3.3.1. Stable Isotope Analysis: $\delta^{18}O$

Oxygen has three stable isotopes which occur naturally: 16O, 17O and ^{18}O where the proportion of each isotope is 99.757% 16O, 0.038% 17O and 0.205% ^{18}O (Rosman and Taylor, 1998). The two of interest when it comes to $\delta^{18}O$ analysis is 16O and ^{18}O. The stable isotope 16O has 8 protons and 8 neutrons whereas ^{18}O has 8 protons and 10 neutrons making it the heavier of the two.

Oxygen isotopes enter the marine biosphere through gas exchange at the ocean surface and then marine organisms absorbs both the ^{16}O and ^{18}O into their shells and tests as

they grow. As the oxygen isotopes are stable they do not decay when the organism dies and the ratio of ^{18}O to ^{16}O can be calculated.

The ^{16}O isotope is the lighter of the two and when the earths temperature is warmer it is evaporated easier than ^{18}O and more ^{16}O is present in the atmosphere. It then rains and the ^{16}O in the water on land, where it eventually drains back into the ocean, or back into the ocean directly.

During colder periods, ^{16}O is still evaporated easier than ^{18}O however when it condenses it falls as snow which builds up on land and causes the ^{16}O to become trapped and not drain back to the ocean. This results in a higher concentration of ^{18}O in the ocean and therefore marine tests which become depleted in ^{16}O.

With this understanding the ^{16}O and ^{18}O isotopes can be measured relative to each other and the results can provide insight into the ocean and earths temperatures.

The equation for calculating $\delta^{18}O$ is as follows (Shackelton., 1947):

$$\delta 18O = \frac{\left(\frac{18O}{16O\text{Sample}}\right) - \left(\frac{18O}{16O\text{Standard}}\right)}{\left(\frac{18O}{16O\text{Standard}}\right)} * 1000 \quad \text{(vi)}$$

3.3.3.3.2. Stable Isotope Analysis $\delta^{13}C$.

As mentioned previously, carbon exists in three forms:^{12}C, ^{13}C and ^{14}C. The unstable ^{14}C has been discussed for AMS Radiocarbon Dating, however the other two isotopes have their usefulness for stable isotopic analysis. Much the same as the oxygen isotope analysis, ^{12}C and ^{13}C are found relative to one another and the ratio of ^{13}C to ^{12}C in marine tests can tell a lot about ocean composition, circulation, and the global carbon cycle

(Schmitter et al., 2017). ^{12}C has six protons and six neutrons and ^{13}C has six protons and seven neutrons.

The presence of ^{12}C in organic matter is more easily incorporated into shells and tests due to it being the lighter isotope of the two and therefore its abundance compared to ^{13}C is much higher. During colder glacial periods, the levels of ^{13}C in upper waters are higher than during interglacial as the ^{12}C is store on land (much the same was as oxygen isotopes) and so the ratio of ^{13}C:^{12}C can provide insight into palaeo-ocean temperatures, circulation, and ventilation (Armstrong and Brasier, 2004). The degradation of marine organisms beneath the photic zone and the release of respiratory CO_2 means that more ^{12}C is released into the ocean and deeper water values of $\delta^{13}C$ are more negative (Armstrong and Brasier, 2004). The ratio of ^{13}C to ^{12}C is what determines the $\delta^{13}C$ value and it is calculated by the following equation (Craig., 1953):

$$\delta 13\mathrm{C} = \frac{\left(\frac{13C}{12\mathrm{CSample}}\right) - \left(\frac{13\mathrm{C}}{12\mathrm{Cstandard}}\right)}{\left(\frac{113\mathrm{C}}{12\mathrm{CStandard}}\right)} * 1000 \qquad \text{(vi)}$$

3.3.3.4. ^{14}C AMS Radiocarbon Dating

There are three Carbon isotopes, ^{14}C, ^{13}C, and ^{12}C all of which are naturally occurring. ^{13}C and ^{12}C are the more common isotopes (98.9% and 1.1% respectively) which are found in the atmosphere; however, they are less reliable for studying due to them being affected by human release of carbon into the atmosphere (Glaser., 2005). Therefore, the less common unstable radioactive ^{14}C (10^{-8}%) isotope is used (it is also affected by unnatural human carbon release however the effects are negligent and thus ignored).

^{14}C combines with oxygen to create $^{14}CO_2$ which along with CO_2 enters the terrestrial biosphere through photosynthesis and into the marine environment by absorption

through gas exchange at the surface and then creatures living in the ocean take that carbon in when making their shells and tests. A living creature will absorb carbon throughout its live until the moment it dies, from that point the intake is stopped, and decay begins.

The unstable nature of the radioactive ^{14}C means the decay is exponential and with a half-life of 5,730 years that means that it takes 5,730 years for half of the ^{14}C to decay and another 5,730 years for the next 25% to decay and so on. Therefore, as ^{14}C absorption stops at the time of death and begins to decay, the quantity of radiocarbon can be compared with the known half-life and the amount of time that has since passed since death can be calculated.

There are two methods that can measure the amount of radiocarbon in a sample: radiometric dating by counting β particle emissions and through accelerator mass

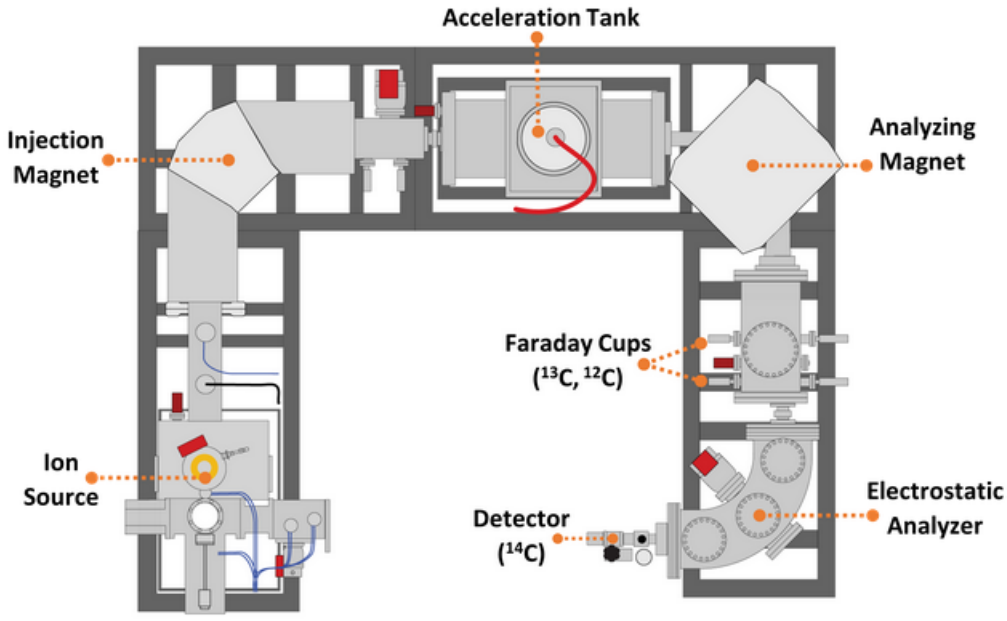

Figure 8: Layout of the Accelerator Mass Spectrometry Equipment (The Chrono Centre., 2024)

spectrometry (AMS). The samples in this study were sent to the 14Chrono Centre for Climate, the Environment Chronology in the School of Natural and Build Environment at Queen's University Belfast and the MICADAS lab at the University of Zurich for AMS dating (Fig. 8).

AMS dating uses a mass spectrometer to distinguish between different types of atoms from their atomic weight by measuring the abundance of ^{14}C relative to ^{13}C and ^{12}C by converting it to graphite and inserting it into an ion source (The Chrono Centre., 2024). Here they are hit with caesium (Cs^{+}) ions which creates negatively charged carbon atoms which are then accelerated out of the source as an ion beam and down a beamline where it then come into contact with helium atoms and the ions are then converted from negative to positive by removing electrons. The ions are then accelerated further down the beamline which has bends where the lighter isotope ^{12}C bends the most followed by the slightly heavier ^{13}C and finally the heaviest of the three ^{14}C. This means that the abundance of all three isotopes in the sample can be measure relative to each other and the ration of ^{14}C to ^{13}C and ^{12}C is the result that is measured to calculate the age of the sample to those of a known standard.

Three samples were taken from Core 1192 in December 2022 and sent to the 14Chrono Centre for Climate, the Environment Chronology in the School of Natural and Build Environment at Queen's University Belfast and later four samples spread across Core 1168 and Core 1192 were sent to the Laboratory of Ion Beam Physics: MICADAS Lab at the University of Zurich.

Shell fragments were used for the first three samples sent to Belfast, however for the other four the planktic foraminifera species *Neogloboquadrina pachyderma* (sinistral) from the size fraction 100-500µm were picked to be sent off to the University of Zurich. The specimen needed to be clean with no attached or infilled sediment, they also needed to show no evidence of transportation, such as broken or damaged tests. One sample included a mix of benthic and planktic specimen were used to make up the weight requirement as the number of *N. pachyderma* was low.

3.3.3.4.1. ^{14}C AMS Radiocarbon Calibration Curves

Once the raw ^{14}C ages were provided by the labs, they then needed to be calibrated from ^{14}C ages to calendar years BP using the software *Calib8.10* (Stuvier and Reimer., 2020). In order to do this, there is a process where decisions have to be carefully made.

The process of carbon exchange into the ocean means that carbon measurements in marine organisms give different results to terrestrial organisms. The time it takes for carbon in the atmosphere to reach the deep ocean means that it will appear different from their true age and so a marine calibration curve needs to be applied to the raw ^{14}C dates in order to give the best estimate of changes in the ^{14}C measurements in the ocean.

For this project three calibration curves were considered; Marine20 (Heaton et al., 2020), IntCal20 (Reimer et al., 2020) and Normarine18 (Brendryen et al., 2020). All three calibration curves have their own merit and so the decision was made eventually to use Marine20 as the results of the second batch of radiocarbon samples returned with results outside of the capabilities of the Normarine18 curve and so it was removed from consideration for the sake of consistency and the IntCal20 for reasons that will be explained.

In addition to this the ages had to be calibrated from the BC provided ages to BP and so a correction to the year 1950 was added as that is the standard for year 0.

3.3.3.4.2. Marine Reservoir Effect

The next consideration for calibrating ages is the Marine Reservoir Effect (ΔR) value. A variety of ΔR values have been created across the global oceans, and for the sake of this specific project only ones concerned with the Arctic were considered. Because the ΔR values are different, a selection of three values was considered (Table 2). These were values which were geographically close to the study location and have been used in previous research papers, and a newer study (Pieńkowski et al., 2022) which could be

Source	ΔR	±	Calibration Curve
Mangerud and Svendsen., (2017)	70	30	Marine20
Knies et al., (2018)	0	0	Marine20
Pieńkowski et al., (2022)	-61	37	Marine20
Brendryen et al., (2020)	0	0	Normarine18

Table 2: The different calibration curves and ΔR values considered in this study.

used to compare with foraminiferal radiocarbon ages but only used with Marine20 (and so this was the reason IntCal20 was not used).

An investigation into the ΔR that was decided for this study can be found in the results section of this report.

3.3.3.5. Calculation of Sedimentation Rates

The ^{14}C AMS radiocarbon dates only give dates of the exact samples that were taken and so in order to calculate the rate of sedimentation it has to be assumed that the undisturbed sediment above the dated samples were deposited at the same rate through time. This results in a linear sedimentation rate which can be used to find, for example, the total number of cm per thousand years or the total number of years per cm.

4. Results

4.1. Location and Characteristics

4.1.1. Location of the Slide and Cores

The Hinlopen slide is located at 80 degrees North on the continental shelf edge on the northwestern Svalbard Margin. The main headwall has an amphitheatre shape and reaches a maximum width of 60,000m in length and sits at a water depth of approximately 200m. The escapement area reaches northwest approximately 25,000m where it narrows into a bottleneck with minimum width of 20,000m at its narrowest point.

The height of the headwalls varies greatly in height, from approximately a couple of hundred metres on the eastern side of the headwall to over 1,500m on the furthers western lobe.

Bathymetric data shows seafloor characteristics that alight with the observations taken by Vannest et al (2006). The site can be broken down into the Western Headwall Area, the Eastern Headwall area and the Intermediate Slide Area (Fig. 9).

4.1.2. Western Headwall Area

The Western headwall area (has the deepest scarp measurements, over 1,500m from continental slope to inner scarp measurements however it is separated into a step-like shelf at approximately 1,000m where there is a mostly flat base with the occasional blocky deposits grouped together that are likely slump deposit. The flat shelf then steeply drops to the maximum depth of the escapement zone of over 1,500m.

East of this first lobs is a second lobe which differs from the rest of the slide lobes. This is at the location where the Hinlopen Strait feeds into the continental shelf waters and the trough mouth feeds past the continental shelf edge. The characteristics of this particular lobe are that it has the gentlest gradient and no clear continuous backwall.

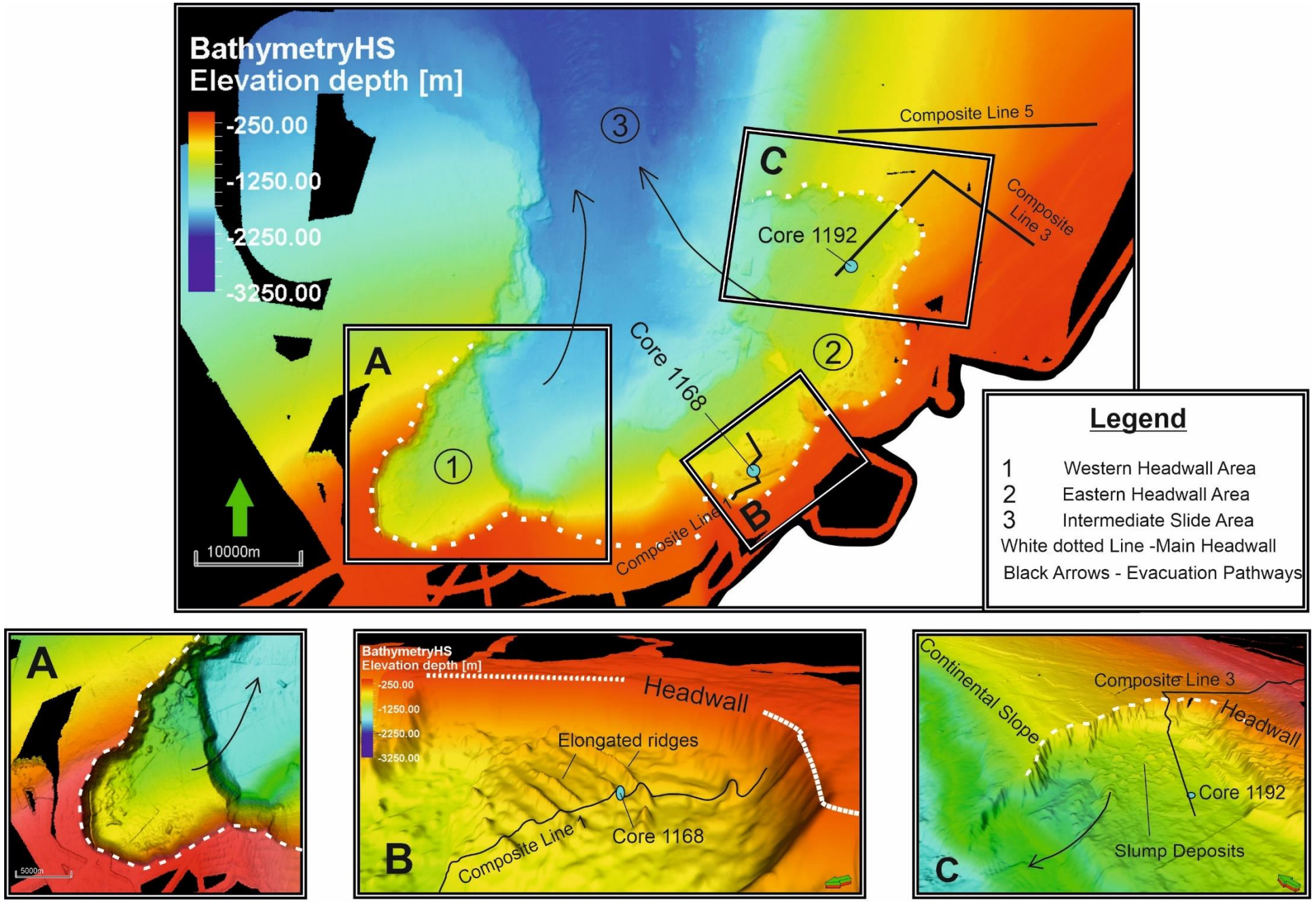
BathymetryHS
Elevation depth [m]
-250.00
-1250.00
-2250.00
-3250.00
10000m
A
B
C
1
2
3
Core 1168
Core 1192
Composite Line 1
Composite Line 3
Composite Line 5
Legend
1 Western Headwall Area
2 Eastern Headwall Area
3 Intermediate Slide Area
White dotted Line -Main Headwall
Black Arrows - Evacuation Pathways
5000m
Headwall
Elongated ridges
Continental Slope
Slump Deposits

Figure 9: Location of the study area showing the main headwall location of the Hinlopen Slide. The location of the two sediment cores are marked with green circles and areas of discussions have been separated into sections A, B and C.

There are no present indicators of slide material here, other than the continuation of features the can be traced back into the Western headwall area.

4.1.3. Eastern Headwall Area

The Eastern Headwall area can be broken down into two locations for this project. Location 1 is immediately east of the gentle lobe from the easter headwall area and is separated by a sediment wall of the continental shelf that had not succumbed to failure. This area is characterised by ridges that protrude from the seafloor mostly parallel with he backwall and each other. There are five main ridges that are most noticeable, the largest of which measures 3,000m in length and protrudes approximately 145m. Smaller intact blocks are also present and are potentially continuations of large ridges after breakage. The distance from the back all to the furthest block is 4,000, into the slide scar and the distance between each ridge is mostly consistent, measuring on average 520m from peak to peak. Core 1168 was taken at this location along the outer rim of one intact ridge (Figs. 9 and 10).

Location 2 is the furthers northeast of the headwall and is technically a southern lobe and a northern lobe. The southern lobe is separated from Location 1 by a smaller sediment wall and characteristically has similar ridges. However, the ridges in this location are disturbed and non-continuous, broken into blocks rather than elongated. Like the previous location the are almost parallel with the backwall and each-other and progress into the escapement area. The longest collection of blocks measures approximately 4,500m and they become more chaotic with distance from the backwall. This location shows multiple step-like surfaces which reach out into the escapement area, the largest of which measures 15,000m in distance from the backwall and is shared with the northern lobe.

The northern lobe is the final site in this investigation and has the smallest measurement of backwall height of only a couple of hundred metres as it resides in the deepest water depth of approximately 600m. This location is likely a continuation of the southern lobe however its morphology differs greatly as there are no protruding ridges and the backwall mostly drops to the shares shelf-step to the southern lobe. There are large blocks clustered together at this location however they show no main orientation and are likely slump material. Core 1192 has been taken at this location within the slump material of the northern lobe.

4.1.3.1. Sub-Bottom Profile

Sub-bottom profile data has been collected and compiled to present high resolution analysis of the seafloor and shallow penetration to show sub-surface characteristics. Recordings of the slide materials show high backscatter and recordings of sediment beneath the seafloor surface do not show much penetration (Fig. 10). However, using this data the quality recordings close to the core locations can be analysed better than with only the bathymetric data and have been outlined and interpreted in Figure 24.

Three main composite lines have been used for investigation. Composite line 1 is taken in the Eastern Headwall area, Location 1 and shows the presence of the elongate ridges where ore 1168 was taken. The relationship between each ridge Is clearer here and their orientation in relation to the shelf and the escapement direction is clearer also. The mostly horizontal slide plane surface can be inferred from the way the ridges protrude upwards are indicative of retrogressive slumping. The profile data clearly shows how the ridge have less height with distance from the backwall and extent into the inner slide escarpment where they then stop.

Composite line two is taken in the northern lobe of Location 2. This clearly shows the relationship between the transition from slope to slide. This location has the best penetration results of the sub-bottom profile data. The slope material at the transition position clearly shows parallel bedding ranging from 1035ms to 1055ms in two-way-travel time (TWT). This parallel lamination is continuous for NE-SW trending segment of

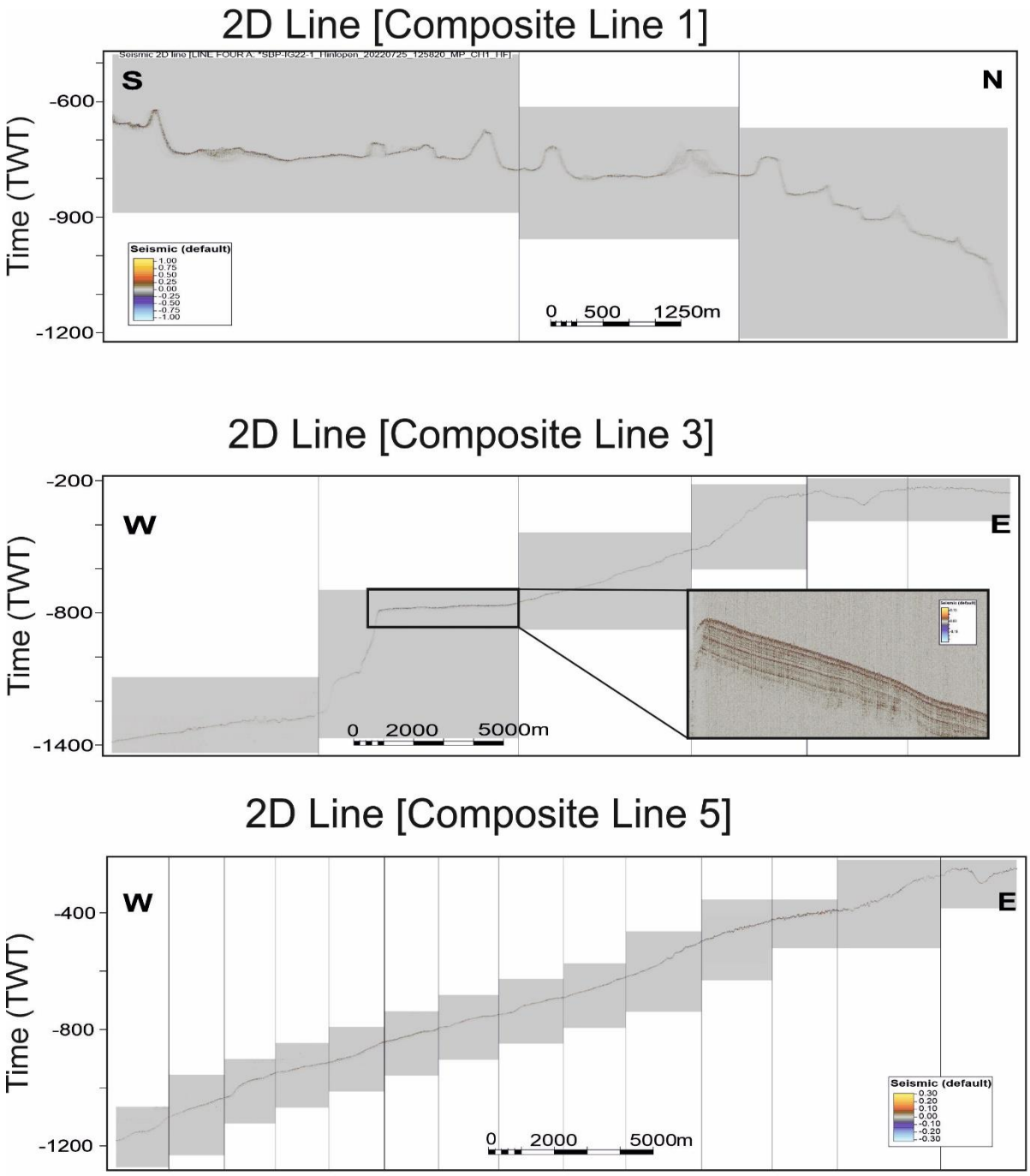

Figure 10: Three composite lines of SBP data merged from multiple single SBP lines to create a continuous transition from continental shelf into slide deposits and down the continental slope. The locations of these composite lines can be found in Fig. 9.

the composite line, however it does not appear to extend in the SW-NE trending continental slope. This is not an indicator that the bedding does not continue and is a result of recording equipment.

Composite line 3 is the final sub-bottom investigation in the area and it taken away from the slide location. It is, at minimum 5,500m north of the eastern headwall and extends approximately 26,000m E-W and records the continental slope undisturbed from the

slide event. This line shows the continuous morphology of the continental slope indicating a very undisturbed nature. The eastern extent of this line shows the seafloor is rocky and disturbed and a deep groove approximately 40m deep.

4.2. Lithological investigation

The two sediment Cores 1168 and 1192 mainly comprise of a large homogenous silty-clay deposit (Fig. 11). The cores have been separated into lithological units which will be discussed shortly. The lithological results will be determined from a combination of visual analysis, X-ray imagery and digital photography (Figs. 12 and 14). It should be noted that in the X-ray images a darker response indicated coarse grained material and the lighter response is finer grainer materials, and the colour of the cores varies from visual analysis and digital imagery so for clarification, any reference to specific Munsell Colour gradients are in reference to in-person analysis.

4.2.1. Core 1168 Lithology

4.2.1.1. Core 1168: Unit 1

Core 1168 taken contains two lithological units. Unit 1 is a large homogenous unit composed of silty-clay, showing clear lamination in X-ray. The lamination is disturbed by coring and as such appears to have a higher angle of deposition towards the base of the unit. This is not the case and so will not be used in any interpretation of the unit. The grain size variation in this unit is mostly consistent, with over 90% of recoded material measuring <60μm except for the top 10 cm which has a higher proportion of larger sediment at 3% each for 63-100μm, 100-500μm and >500μm. There is no visible

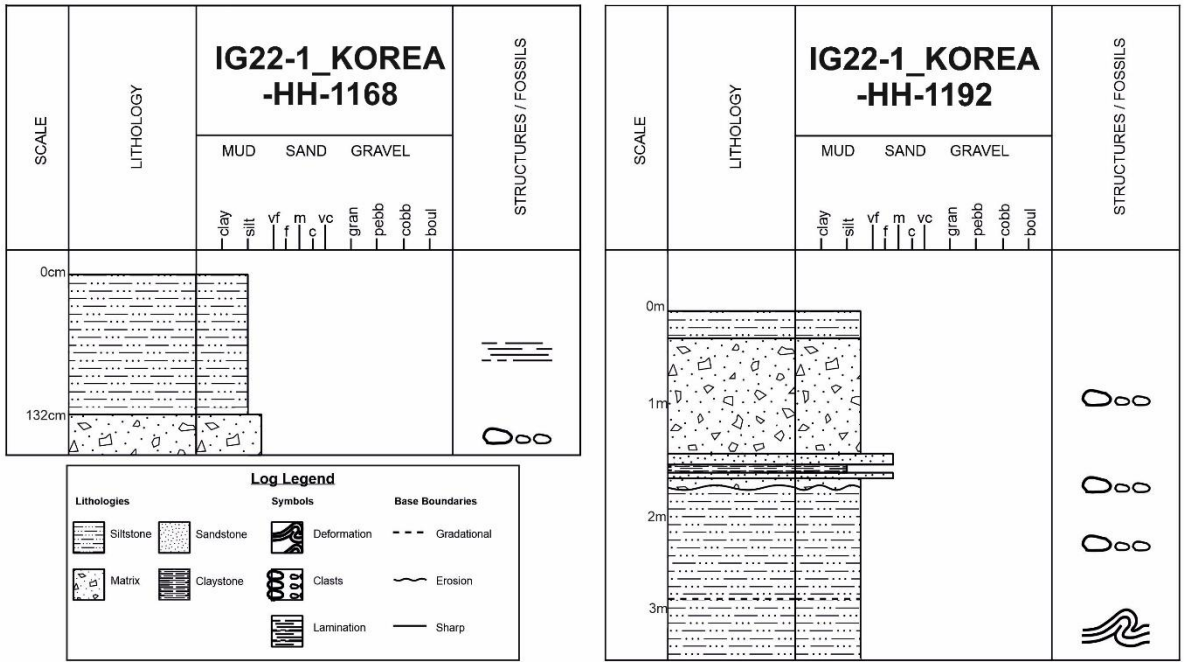

Figure 11: Lithological logs of both Core 1168 and Core 1192.

bioturbation or disturbance of the unit and so it is massively cohesive. The top 12cm of the unit contains small-medium pebbles measuring approximately 1cm and smaller. The colour of this unit reads as 5Y 4/3 towards the top 12cm and 5 Y 4/2 for the rest of the massive unit.

4.2.1.2. Core 1168: Unit 2

Unit 2 exists solely in the second metre of the sediment ore and is cut off by the base and so can be inferred to extend to an unknown depth. In the core it measures from 136cm to 176cm and has a clear mostly sharp surface boundary transitioning into a silty-clay mud matrix containing a large number of small to very large pebbles. The larges pebbles measure approximately 5x5cm in size and the smallest are <1cm. The overall grain size of this unit is >60% sediment <63µm in size with an increase in the 100-500µm fraction up to 16% and the >500µm fraction up to 19% in addition to the pebbles (Fig. 13). There is no clear orientation of the pebbles present in this unit,

Figure 12: Larger material from the disturbed turbidite material in Core 1168 (right) and 1192 (left).

however it appears that the majority of the largest are limited to the upper 15cm of the unit. The smaller debris and pebbles (1-<1cm) continue within the silty-clay to the base of the core. This unit is slightly darker in colour, reading as 5Y 4/1, however the digital photograph shows a black like appearance, this is likely due to the core exposure and cleaning of the core so it is not suitable to indicate that the unit was entirely this colour as this was not the case.

4.2.2. Core 1192

Core 1192 has a maximum core length of 376cm split into four sections. This project is investigating one specific slide event and so the entire core has been logged and the units investigated for the sake of consistency. However further detail in later sections of this report will focus on the top 102cm of the core.

4.2.2.1. Core 1192: Unit 1

Unit 1 of Core 1192 is the smallest, measuring from 0-26cm. It contains very fine silty-clay material and it Is difficult to determine If lamination is present or a result of artefacts

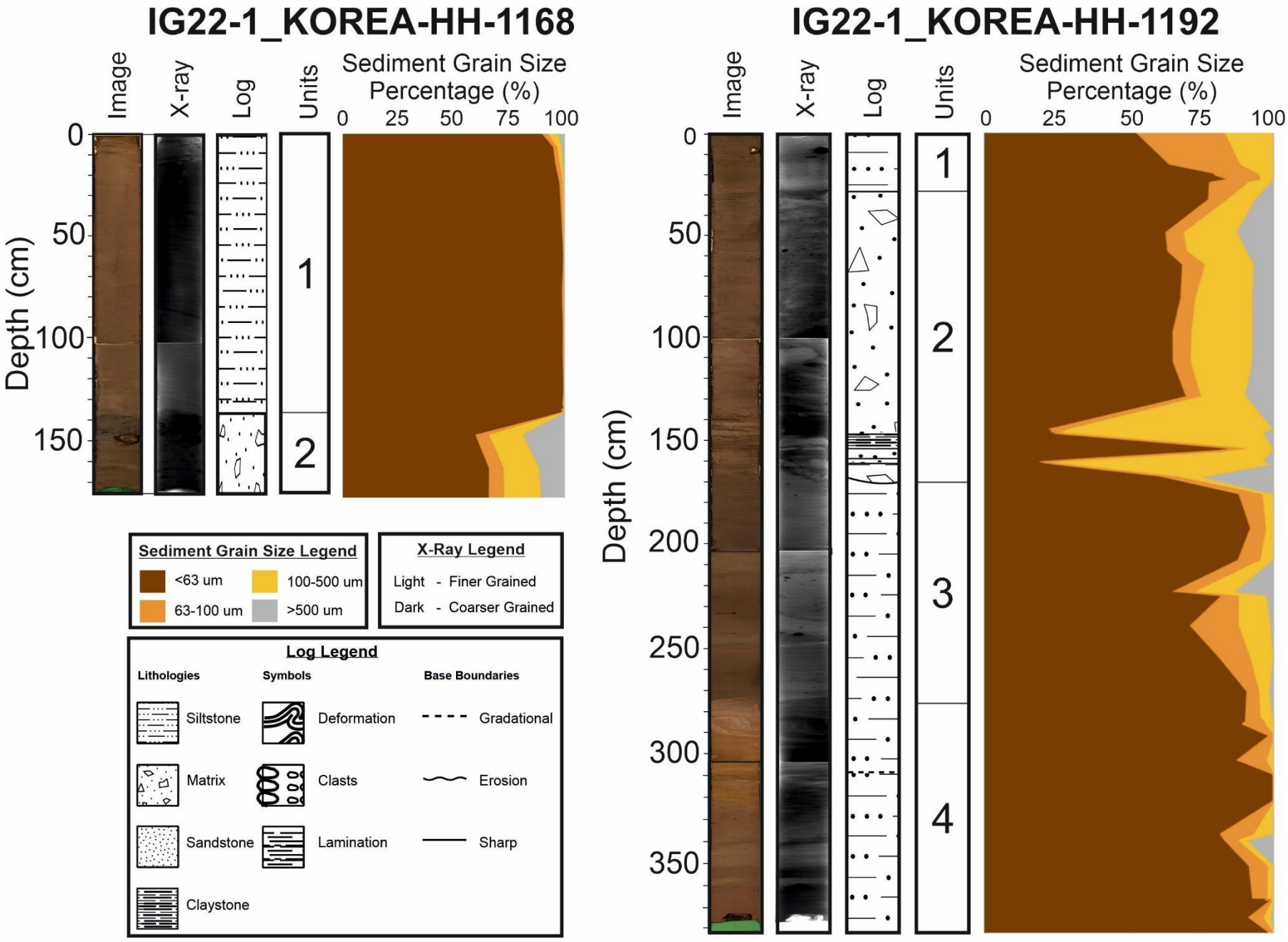
IG22-1_KOREA-HH-1168
Image
X-ray
Log
Units
Sediment Grain Size Percentage (%)
0
25
50
75
100
Depth (cm)
0
50
100
150
1
2
Sediment Grain Size Legend
<63 um
63-100 um
100-500 um
>500 um
X-Ray Legend
Light - Finer Grained
Dark - Coarser Grained
Log Legend
Lithologies
Siltstone
Matrix
Sandstone
Claystone
Symbols
Deformation
Clasts
Lamination
Base Boundaries
Gradational
Erosion
Sharp
IG22-1_KOREA-HH-1192
Image
X-ray
Log
Units
Sediment Grain Size Percentage (%)
0
25
50
75
100
Depth (cm)
0
50
100
150
200
250
300
350
1
2
3
4

Figure 13: Cores 1169 and 1192 where lithology has been compared with grain size downcore.

from coring in the X-ray. Visually there is no indication of lamination. The grain size values for this unit has a range of 80-50% of sediment<63µm followed by a range of 30-10% for the 63-100µm fraction, 17-5% for the 200-500µ fraction and 1.09-0.06% of sediment >500µm. In addition to this there are two individual pebbles present at approximately 8cm and 10cm, the pebble at 8cm measure approximately 3x4cm in size and the one at 11cm is thinly elongated measuring approximately 0.5-3cm in size. There is no disturbance of this unit, and the material is cohesive. The X-ray imagery shows a mostly continuous density response, however, there appear to be a gradient of light to dark response from 26cm to 8cm which could indicate slight grading. This compared to the grain size investigation indicates there could potentially be normal grading in this area of the unit shown by an increase in percentage of grain sizes in the 63-100µm and 100-500µm fractions. The colour of this unit reads as 5Y 4/1.

4.2.2.2. Core 1192: Unit 2

Unit 2 of Core 1192 is the largest unit in the core. It measures from 26cm to 167cm and characteristically has a mix of lithologies as well as frequent changes in colour, grain size and X-ray response. The surface of this unit is clearly defined in X-ray imaging however difficult to see visually. It is marked by a dark x-ray response and a complete change in internal structure. The grain size for this unit is mostly disturbed silty clay with a large number of small pebbles that measure <1cm in size and few that measure >1cm. a range from 76-16% of the sediment in this unit is <63µm, 7.9-3.8% is 63-100µm, 75-7% is 100-500µm and 26.6-0.7% is >500µm. This drastic difference from finer silty-clay material into fine-medium grained sand material is unique to this deposit and appears in two layers, one at 138-148cm and another at 155-160cm, both are separated by a fine silty-clay mud layer which contains no clear disturbance. The base of this unit is angled, and unlike Core 1168 it is not likely an error due to coring and do the base is erosively intruding into Unit 3 below. The colour gradients for this unit vary but on average it reads as 5Y 4/2.

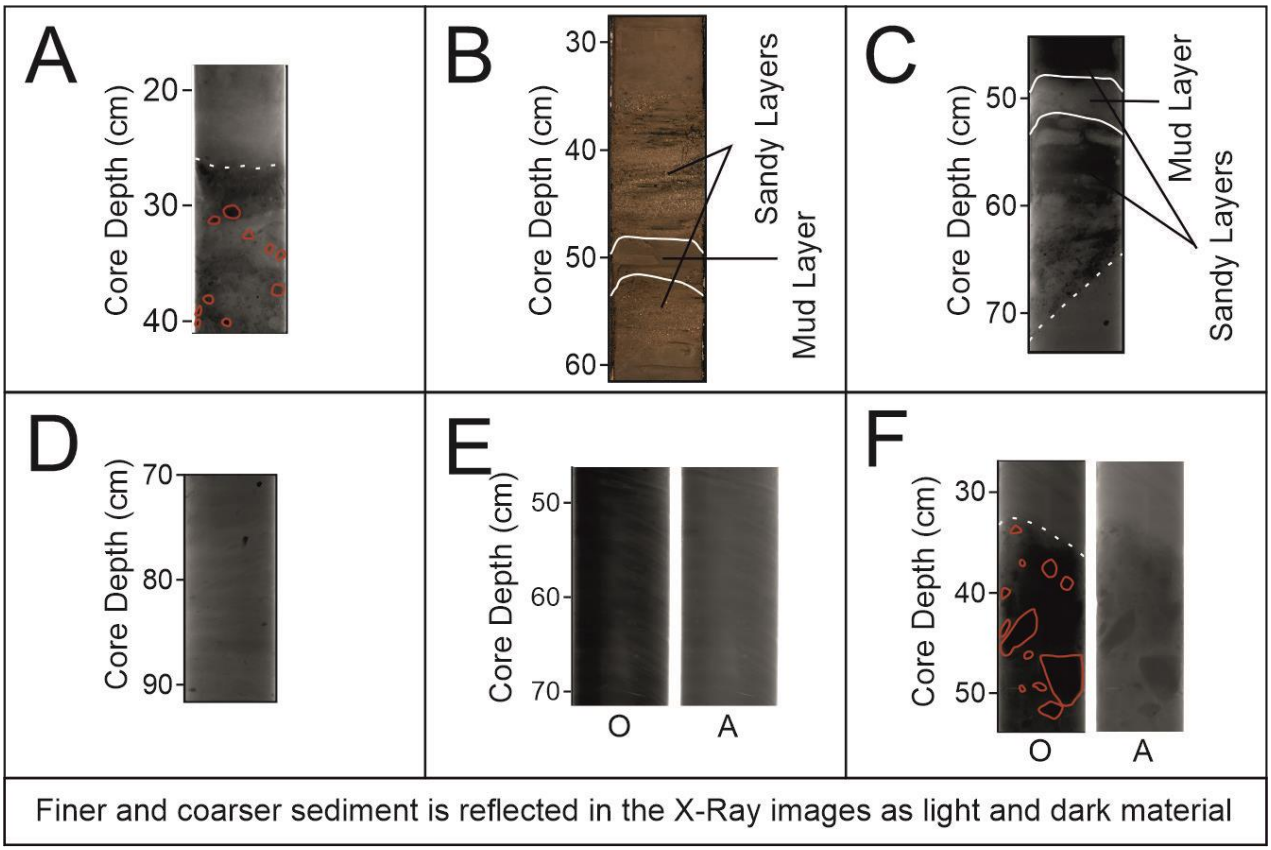

Figure 14: Zoomed in areas of both sediment cores to show fey features. A = 1192-01 (Unit 1 to Unit 2 boundary), B=1192-02 (grain size variation in Unit 2), C=1192-02 (Base of Unit 2, Unit 2 to Unit 3 boundary), D=1192-02 (laminated sediment in Unit 1, The quality of the x-ray is reduced with size of the figure and so an Original (O) and Adjusted (A) version are provided where lamination is clearer), E=1168-01, and F=1168-02 (the Unit 1 to Unit 2 surface boundary, again an Original (O) and Adjusted (A) version are provided). The red drawings outline large clasts within the sediment.

4.2.2.3. Core 1192: Unit 3

This is the most cohesive unit of the core. Unit 3 measures from the angled base of Unit 2 at 167cm to 278cm. It is a largely homogenous silty-clay unit with thin lamination and the occasional pebble/dropstone. The grain size variations here reflect the large homogenous unit that it appears in X-ray, with 97-63% sediment in the <63µm fraction,

10.8-2.6% in the 63-100µm fraction, 14.2-0.17% in the 200-500µm fraction and 14.4-0% in the >500µm fraction. There are three thin layers where the presence of pebbles/dropstones are most frequent, at 211-213cm, 242-244cm and 263-265cm. A

sample was taken at 211-213cm which relatedly shows an increase in grain size at this depth where the percentage of sediment in the 100-500μm and >500μm fractions reach 14%. The colour of this unit is 5Y 4/1.

4.2.2.4. Core 1192: Unit 4

The final unit of this core measures from 278cm to the base at 376cm. This unit shows the clearest evidence of lamination and there is banding present ranging from 280-290cm which could be indicative of soft sediment defamation. This unit is characterised by the smallest range in <63μm grain size at only 99-80%, therefore the following three fractions, 63-100μm, 100-500μm and >500μm have the small ranges at 12-0.13%, 6.9-0.08% and 9.7-0% respectively. The unit shows frequent changes in colours, most evident in the digital image of the core, the top 35cm of the unit is much lighter in colour, showing a gradient range that is more red and orange and in person the colour of the top section reads as 5Y 2.5/1 and the base returns to the core average of 5Y 4/1.

4.2.3. Lithological summary

The two sediment cores both mostly contain a silty-clay lithology differentiated by grain sizes, lamination and presence of debris and other material such as drop stones. It is possible that Unit 1 in Core 1168 and Unit 1 in Core 1192 are the same lithological unit, however, the presence of lamination in Core 1168 and the variation in grain size, where Core 1168 has a <63μm percentage range of 90-80% and core 1192 has a range of 80-50%, means that further detailed investigation would be necessary to completely accept or write off this theory. Both cores have a unit which contains a large collection of debris and are characterised by an increase in overall grain size and the presence of small-to-very large pebbles. These are Units 2 in both 1168 and 1192.

Unit 2 in Core 1168 does not have a base due to the length of the core, however, it is clear from the immediate transition from a matrix containing very large-medium sized pebbles into a continuous thinly laminated silty-clay unit with no disturbance that this is the unit identifying the submarine landslide. The disturbed material with no clear orientation and

inclusion of these pebble clasts which have clearly been transported marks the boundary of the landslide in this core at approximately 136cm.

Unit 2 in Core 1192 has a base which has eroded into the sediment beneath, and a surface appears to almost immediately transition into the silty-clay unit above. The inclusion of debris is chaotic with no orientation. The unit also contains sand layer of a max depth of 15cm with a thin mud layer between the two. The interpretation of this unit is that it is the landslide deposit signified form the chaotic nature of the debris within the sediment that has been transported from elsewhere and the presence of the sandstone layers indicate that the base of the unit is the base of the landslide however it is possible that a smaller event occurred previously and that is the reasoning for the two sandy layers separated by the thin mud layer.

4.3. Foraminiferal Identification

The complete counts of foraminiferal analysis for Cores 1168 and 1192 can be found in Appendices. Each sediment core shows their own species abundance however the two most abundant species in both cores are *Melonis barleeanus* and *Cassidulina reniforme*.

4.3.1. Core 1168

4.3.1.1. Benthic Foraminifera

A total number of 42 benthic foraminifera species have been identified within this core. The results of the most abundant species are plotted in Fig. 15. The most abundant species is *C. reniforme* which Is present in every sample and the most dominant species in all but the 7cm and 29cm sample where it is exceeded by *Cibicides lobatulus* and *M. barleeanus* respectively. The overall trend of *C.* reniforme is decreasing with time towards the top of the core. It is highest in abundance at 104cm and 93cm.

The second most abundant species is *M. Barleeanus* which has an overall abundance of 15-20% in every sample besides 29cm where it increases to 24% and is the most

IG22-1_KOREA-HH-1168: Foraminifera

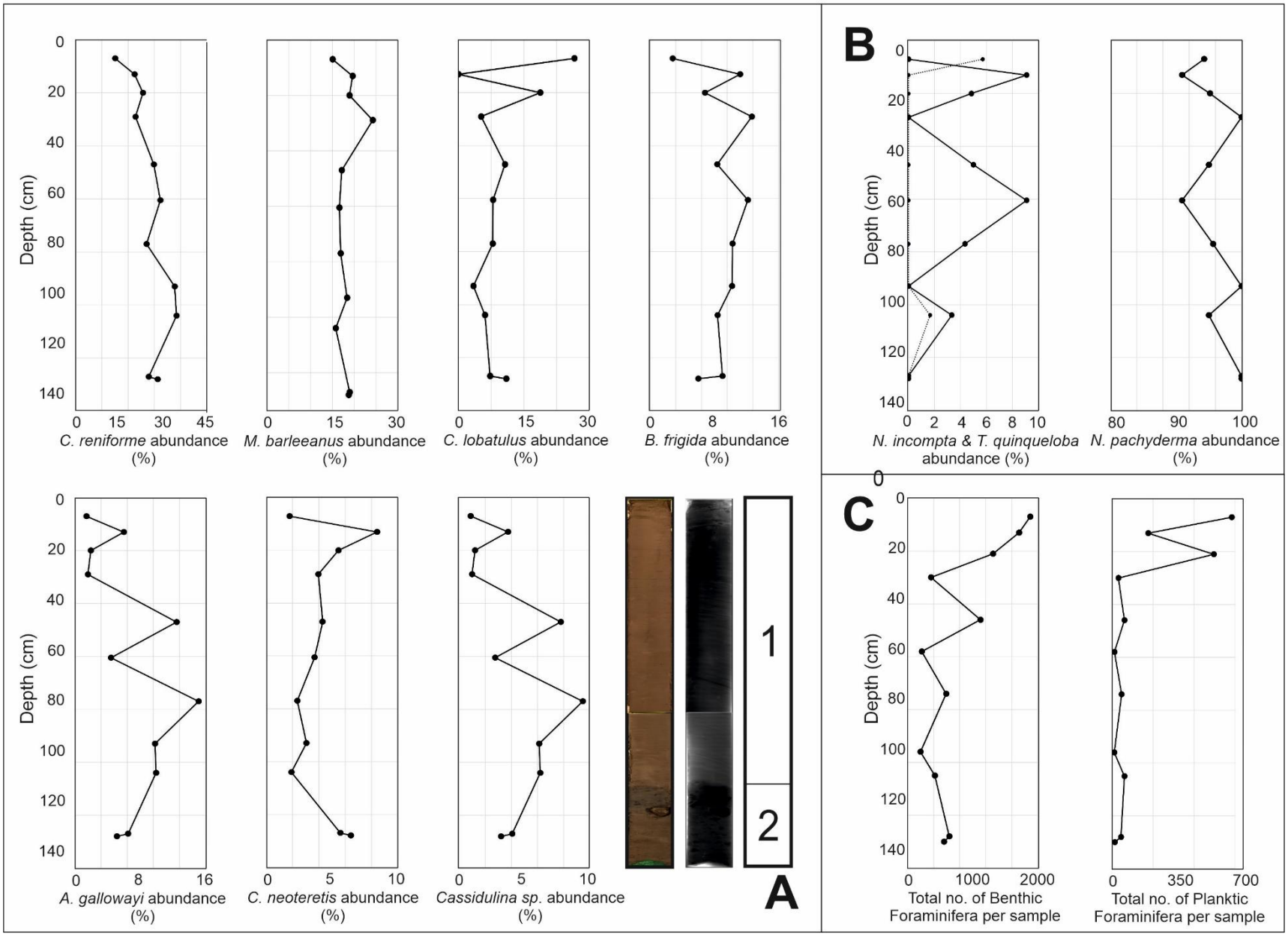

Figure 15: Graphs of the most abundant foraminiferal species found in Core 1168 compared with the imaged cores and the x-rays. A = Benthic Foraminifera, B = Planktic Foraminifera, and C = Total number of benthic and planktic species per 100-500µm sample.

dominant species. *M. barleeanus* has a steady trend and is overall consistent throughout the entire core.

Two other species which are common in the core are *C. lobatulus* and *Buccella frigida*. Interestingly these species appear to mirror each other, where a decrease In *C. lobatulus* is met with an increase in *B. frigida*. *C.lobatulus* is present in every sample except 13cm and is mostly consistent but decreases slightly from the base to 93cm and then increases to 29cm where it then begins to fluctuate. *B. frigida* has an overall increasing trend from the base to 60cm where it then begins to fluctuate.

It should be noted however, that *C. lobatulus* has its highest abundance towards the top of the core, however these samples, where the species is present, includes a high count of species with broken or deformed tests which are indicative of transportation and so this should be considered when discussing the abundance in these two samples (7cm and 20cm).

Other species of interest include *Astronium gallowayi* and *Cassidulina neoteretis*, the former of which has a fluctuating abundance throughout the core and has its highest percentages at 47cm and deeper. *C. neoteretis* decreases from 128 to 104cm and then has a steady increasing trend to 13cm but then dramatically drops to its lowest count at 7cm.

The most diverse samples are the deepest and oldest samples which also correlates with samples which have some of the fewest individuals per gram. Interestingly, the sample with the most foraminifera per gram (7cm) has the lowest count of the most abundant species (where *C. lobatulus* is the only exception).

The total number of foraminifera per sample ranges from the lowest count of 810 individuals at 7cm to 8211 at 128cm, however as Figure 15 displays, this is in no way

indicative of an overall trending increase downcore.

4.3.1.2. Planktic Species

Every sample in this core is dominated by *Neogloboquadrina pachyderma* (sinistral) which never drops below 90% of a sample and counts for 100% in four occasions. In five instances (13cm, 20cm, 60cm, 77cm and 104cm *Neogloboquadrina incompta* (also referred to as *N. pachyderma* dextral, however in this report it has be referred to as *N. incompta*) is present. One other species which appears very infrequently is *Turborotalida quinqueloba* at 7cm and 104cm.

The total number of planktic foraminifer per gram is incredibly low throughout most of the core where the entirety of the sediment 100-500um fraction was used to identify specimen. However, it does see a rapid increase from 20cm and upwards where the overall grain size of each sample also increased.

4.3.1.3. Test Composition

The composition of the foraminiferal tests shows a majority percentage of test are hyaline where over 90% of individuals belong to this group (Table 3). Following this, the next abundant are Milioloids, these species are present in over half of the samples, however there is only one sample where there is more than one species present at a time (60cm where there are two). Milioloids are not present in the three samples at the top of the core.

The final test composition is the agglutinate tests and these only account for 2.4% of the overall specimen found and they are only present in one sample, 47cm.

Core	Test Composition Percentage (%)		
	Hyaline	Miliolina	Agglutinated
1168	90.5	7.1	2.4
1192	87.5	10	2.5

Table 3: Table showing the percentage of test composition for the sediment cores.

4.3.2. Core 1192

4.3.2.1. Benthic Foraminifera

A total number of 40 individual species have been identified in Core 1192 and the results of the most abundant species are plotted in Figure 16. The most abundant species in this core is *M. barleeanus* which is the most dominant species in four samples and has high recordings for samples taken in Unit 1 above the landslide deposit. It has its highest recordings at 226cm however in samples where it is not the most dominant species it mostly accounts for 10% or less of the overall species in a sample.

The second most abundant species is *C. reniforme*. This species is the most averagely abundant throughout the core with recordings of >13% in all but four samples and never falls beneath 5% of a sample. The percentage of *C. reniforme* decreases from the base of Unit 1 to the top of the core. Beneath the landslide deposit of Unit 2 *C. reniforme* has an increase in percentage when *M. barleeanus* decreases.

The third species to not in this sample is *C.neoteretis*. This species has its highest abundance at the base of the core, and decreases to 226cm and then rise and falls around 182cm. The lowest recordings of this species can be found post-landslide in Unit 1. The trend of this species appears to mirror that of *M. barleeanus* where an increase in *C. neoteretis* percentage is matched with a decrease in *M. barleeanus*.

C. lobatulus is consistently low throughout Unit 3, and peaks post landslide in Unit 1. *Islandiella norcrossi* and *Cassidulina laevigata* both show similar trends peaking between 168cm and 186cm. Individuals identified as *Cassidulina sp.* also follow a similar trend, however, have a higher percentage towards the base of the core. *A. gallowayi* remains consistent up-core except for at 3cm where it reaches its peak.

Overall, the total number of foraminifera per sample ranges from less than 1,000 individuals at 241cm to over 85,000 individuals at 286cm. Besides the recording at

IG22-1_KOREA-HH-1192: Foraminifera

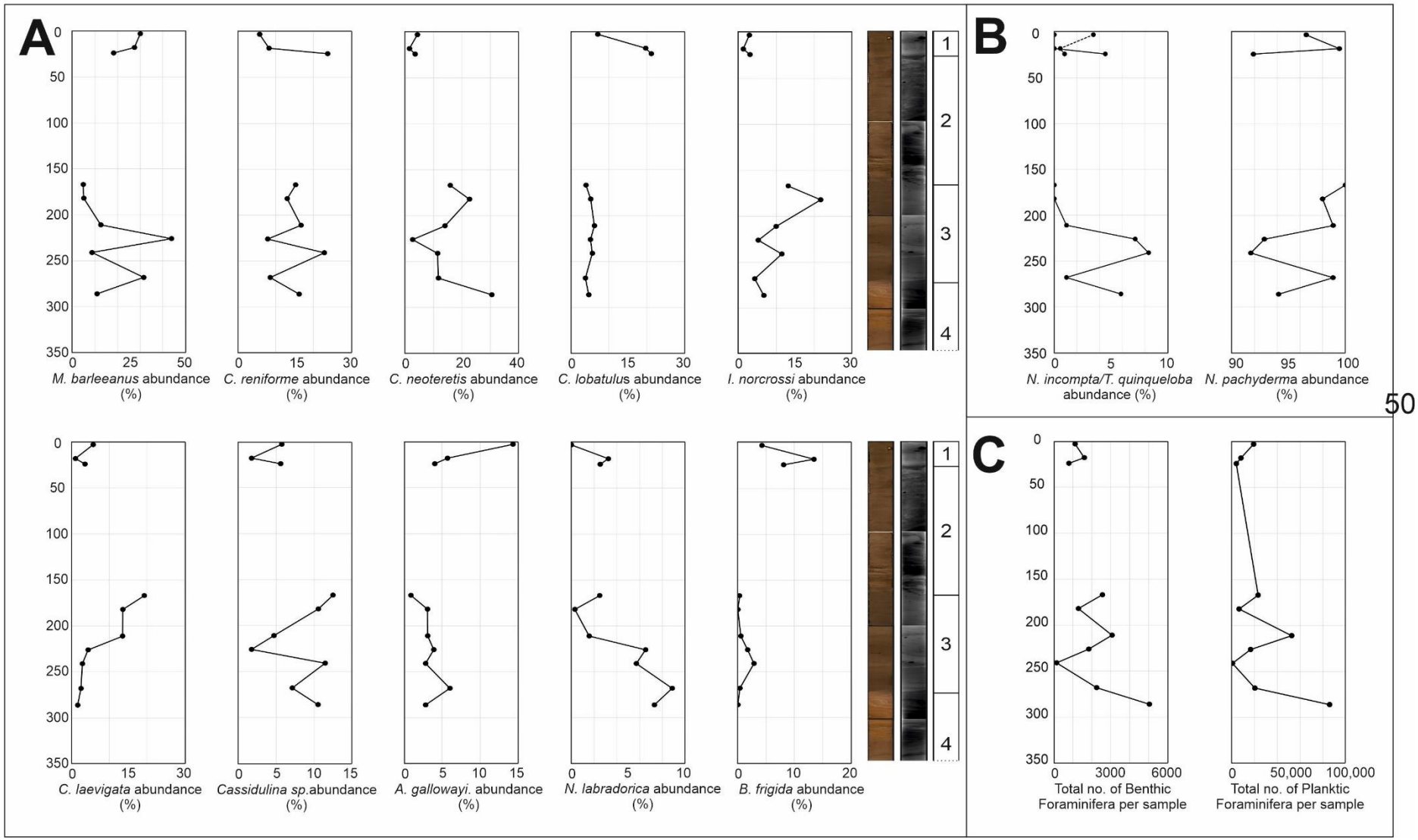

Figure 16: Graphs of the most abundant foraminiferal species found in Core 1192 compared with the imaged cores and the x-rays. A = Benthic Foraminifera, B = Planktic Foraminifera, and C = Total number of benthic and planktic species per 100-500µm sample.

249cm, samples taken in Unit 1are incredibly low compared to the number of individuals found pre-landslide in Unit 3.

4.3.2.2. Planktic Foraminifera

The most abundant planktic species found in this core is *N. pachyderma* which accounts for >90% of individuals in every sample and 100% in one (4 down). There is a higher frequency of individuals in the samples taken above the landslide deposit compared to those found below.

N. incompta are also found more frequently in samples beneath the landslide deposit however they are not found in samples at 7cm, 167cm and 185cm. Some planktic individuals in this core proved difficult to identify from the quality of their tests and so these have simply been classified as *Neogloboquadrina sp. T. quinqueloba* is also present in the three youngers samples but absent throughout the rest of the core.

An increase in the total number of planktic foraminifera per sample corresponds with an increase in the total number of benthic foraminifera pr sample.

4.3.2.3. Test Composition

The most dominant test type in this core is foraminifera with Hyaline tests, followed by Milioloids and then agglutinated species (Table 3). Milioloids are found in four samples, all in Unit 3 before the landslide event. One of these four samples has three individual species of Milioloid whereas the other three all only have one species present. The only sample with an agglutinated foraminifera is 211cm which also has the highest percentage of Milioloids.

4.4. X-Ray Fluorescence and Multi Sensor Core Logging

The elemental and geochemical analysis has been undertaken and the results presented as natural log ratios in order to minimise error. Natural log ratios of Ca/Fe, Ca/Ti, Ca/Si have been used as indicators of marine-to-terrestrial elemental inclusion and natural logs of Ca/K, Zr/Al, Ti/Al and Si/Al have also been analysed as potential indicators of grain size change throughout the cores.

4.4.1. Core 1168

The elemental analysis for this core varies in its reflection of the transition between lithological units that have been identified in Section 4.2.1. of this report.

Recordings of ln(Ca/Ti), ln(Ca/Fe), ln(Ca/K) and ln(Ca/Si) all correlate to one another nicely. They show a mostly continuous recording throughout the silty-clay Unit 1 with a slight discrepancy in the top 12cm where the material is slightly more disturbed. There is an obvious decrease in each recording at the boundary between Unit 1 and Unit 2, however the recording of ln(Ca/Fe) does appear to increase slightly at the transition zone and then increase again approximately 15cm into Unit 2. This same position is marked by a change in fluctuation between the other three Ca ratios (showing a decrease in ln(CA/Ti) and ln(Ca/Si), and an increase in ln(Ca/K)).

There are similar trends in the recordings of ln(CA/Si), ln(Ti/Al) and ln(Zr/Al) which is present in the high fluctuations between 30-70cm and then a continuous steady reading until the transition zone between Unit 1 and Unit 2. A peak can be seen in all three at 130cm and as a the Unit 1 and Unit 2 interface is not as prominent in ln(Ti/Al) and ln(Zr/Al), however both are characterised by a higher amount of fluctuation and ln(Ti/Al) does experience a small increase.

The measurements of ln(Si/Al) in this core show the most consistency with depth. Overall the ratio has an increasing trend downcore with a most noticeable increase at 150cm which correlates with a decrease in ln(Ca/Fe), ln(Ca/K), ln(Ca/Si) and ln(Zr/Al), and an increase in ln(Ca/Fe).

IG22-1_KOREA-HH-1168 XRF and MSCL

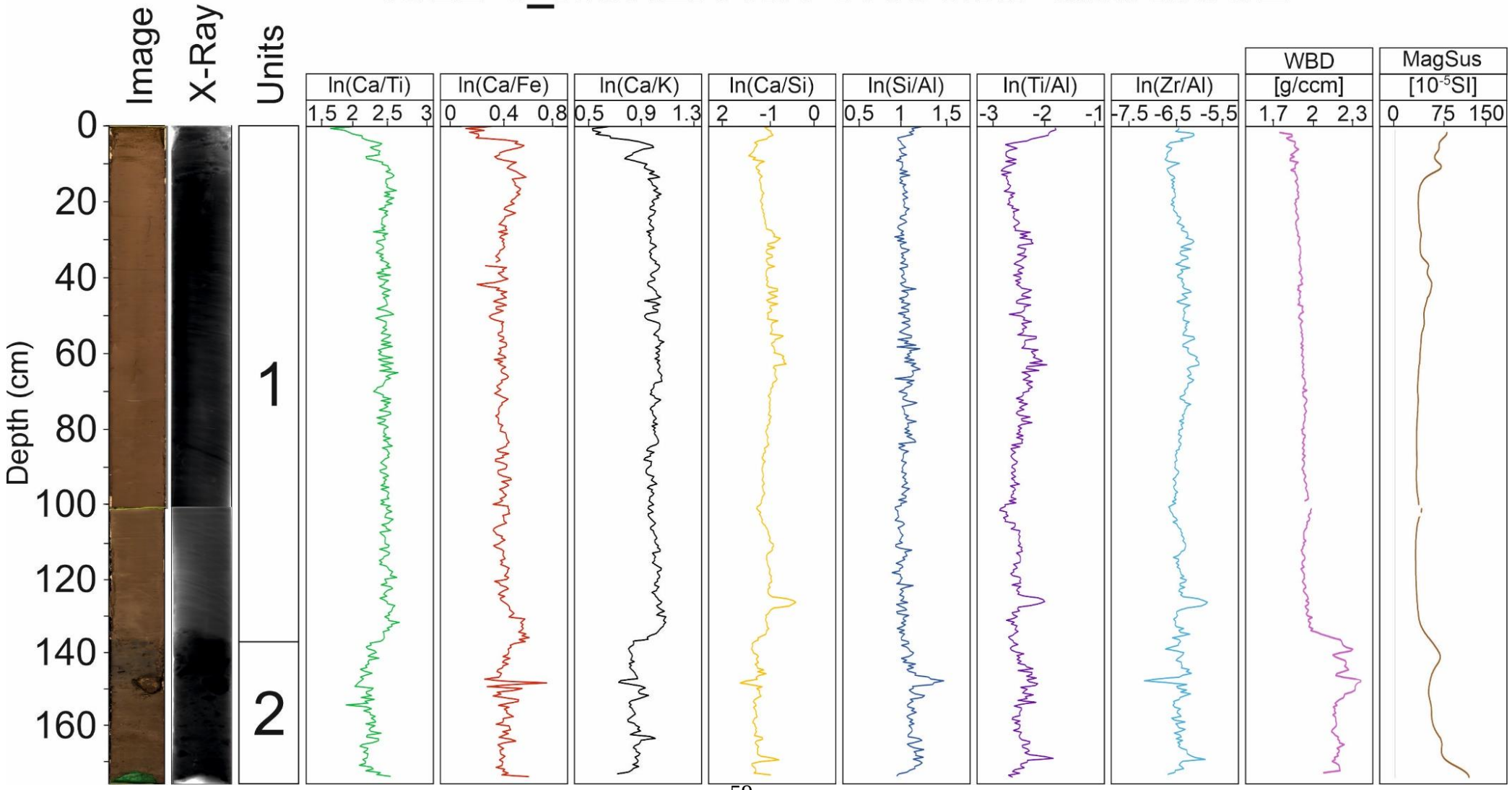

Figure 17: Core 1168 XRF data analysis, ln ratios are measured in ‰.

The MSCL measurements for this core show the clearest boundary between the two units. The WBD shows a consistent recording that has a very slight increase from 1.86g/cm^3 to 1.99cm^3 which compared to the rapid increase to 2.3g/cm^3 at 139cm makes for a drastic transition. The WBD for Unit 2 fluctuates but remains high until the base of the core.

The magnetic susceptibility readings for this core also show an peak at the Unit 1 and Unit 2 boundary and then decreased in the top 15cm which aligns with the decrease in Ca ratios in the same position. A peak can be seen at 39-46cm which correlates with higher fluctuation levels in ln(Ca/Si) and ln(Ca/Fe).

4.4.2. Core 1192

The response of XRF readings in Core 1192 define the changes in lithological units much clearer than the previous core (Fig. 18).

Much the same as Core 1168, the Ca ratios (ln(Ca/Ti), ln(Ca/Fe), ln(Ca/K), and ln(Ca/Si) all have matching trends downcore, with an increase from the top of the core until the boundary separating Unit 1 and Unit 2 where the recordings all the drop for approximately 10cm. The top half of Unit two has a very stead recording with little fluctuation only limited to the top 40cm of Unit 2. The second half of Unit 2 (in Section 02 of Core 1192) shows much higher levels of fluctuation which aligns with the changes in density recordings present in the X-ray images. The base of Unit 2 is marked in these ratios as a return to steady readings lower than those within Unit 2.

The recording of ln(Si/Al) is much like the recording in the previous core, being consistent downcore. However, the ln(Si/Al) is marked by an increase at 135cm to approximately

158cm where there are two main peaks. These peaks correlate with the presence of the clay-mud layer sandwiched between two layers of sandy material.

The recordings for ln(Ti/Al) and ln(Zr/Al) again correlate to one another, and much the same as the Ca ratios, they do not show much change in the top half of Unit 2 but an increase I the lower half with the mid-grey X-ray recording between 115-136cm. The bottom half of Unit 2 which shows the most colour and grainsize change also has a slight increase in recordings of ln(Ti/Al) and ln(Zr/Al) and the base of Unit 2 is marked by the recordings dropping to the same measurements as in the top half of Unit 2.

Much the same as Core 1168, the MSCL readings identifies the lithological units nicely. There is a decrease from the top of the core through Unit 1 to the Unit 2 boundary where the recordings of both the WBD and the Magnetic susceptibility increase, interestingly, the WBD is shows a small peak before the boundary and the magnetic susceptibility shows the opposite. Much like the XRF readings, the top half of Unit 2 does not show much change in either WBD or magnetic susceptibility and the peak and drop that can be seen at 100cm is an artefact from the recordings and should not be taken as a true recording of the internal features of the core. The WBD shows two peaks which align with the ln(Si/Al) peaks and the sand-mud-sand layers at 135-158cm. The magnetic susceptibility shows a decrease in recordings at this position in the core. The Unit 2 to Unit 3 boundary Is marked by a drop in WBD however the magnetic susceptibility increases to its highest recording (excluding the artificial peak at 100cm).

4.4.3. Elemental Analysis Summary

Overall, the elemental analysis of Core 1168 shows a decrease in Ca ratios when transitioning into the landslide deposit of Unit 2 and the massive Unit 1 does not show much variation in anything downcore.

On the other hand, Core 1129 shows a much wider variety of recordings and the distinction of units and grain size changes can be clearly identified throughout both Sections 01 and 02 in Units 1, 2 and 3. Interestingly, the recordings of Ca ratios are

IG22-1_KOREA-HH-1192 XRF and MSCL

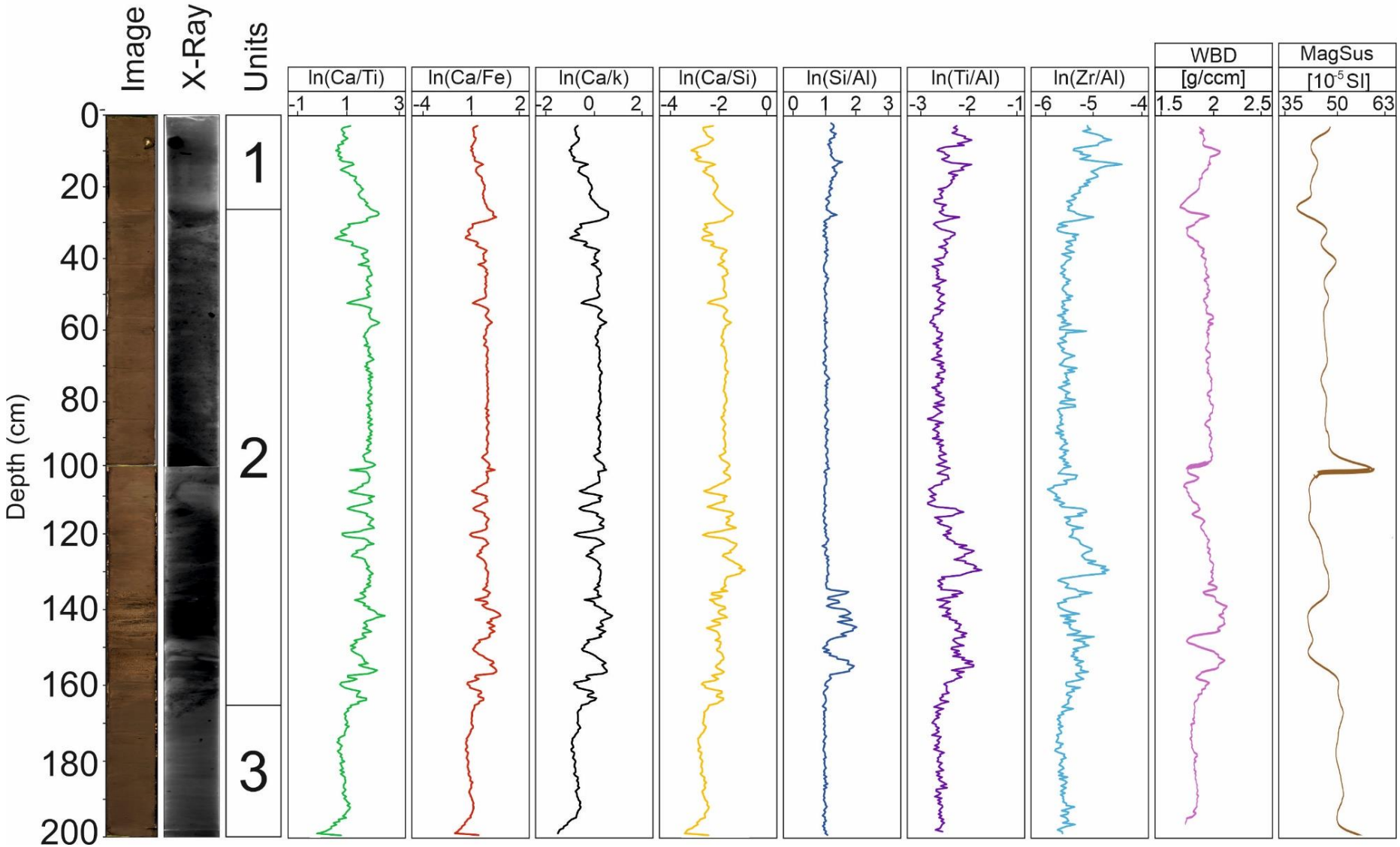

Figure 18: Core 1168 XRF data analysis, ln ratios are measured in ‰.

highest within the landslide deposit of this core, opposite of what can be seen in Core 1168).

Measurements for grain size are clearest in the ln(Si/Al) ratio and WBD for Core 1192, where the presence of the sandy lays is emphasised. The overall grain size for Core 1168 does not fall below 89% of the <63µm fraction and the recordings of ln(Si/Al) in this core is consistent with this.

4.5. Stable Isotope Analysis

Stable isotope analysis for $\delta^{18}O$ and $\delta^{13}C$ were determined from both sediment cores ranging from 7-130cm in Core 1168 and 3-286cm in Core 1192. These values can give an insight into the oceanographic and climatic changes throughout time and down core.

The in-house standard for precision of replication at the University of Bergen for $\delta^{18}O$ was ±0.04‰ with a 1 σ standard deviation. The recording of one sample (*C. reniforme*

at 3cm) was flagged as less reliable with lower precision, however the result was considered suitable and has therefore been included.

The $\delta^{18}O$ measurements were corrected for two separate ice volume corrections, one being Fairbanks, (1989) (referred to here as ‘FIV’) and the other being Shackelton et al., (2023) referred to here as ‘SIV’). The results of these analyses can be found plotted against the depths at which the samples were taken.

Foraminifera Species	**Correction**
Melonis barleeanus	0.41 (Duplessy et al., 1980)
C. reniforme	0
N. labradorica	-0.2 (Duplessy et al., 2005)
C. neoteretis	0
N. pachyderma	0

Table 4: Foraminiferal species and their disequilibrium correction.

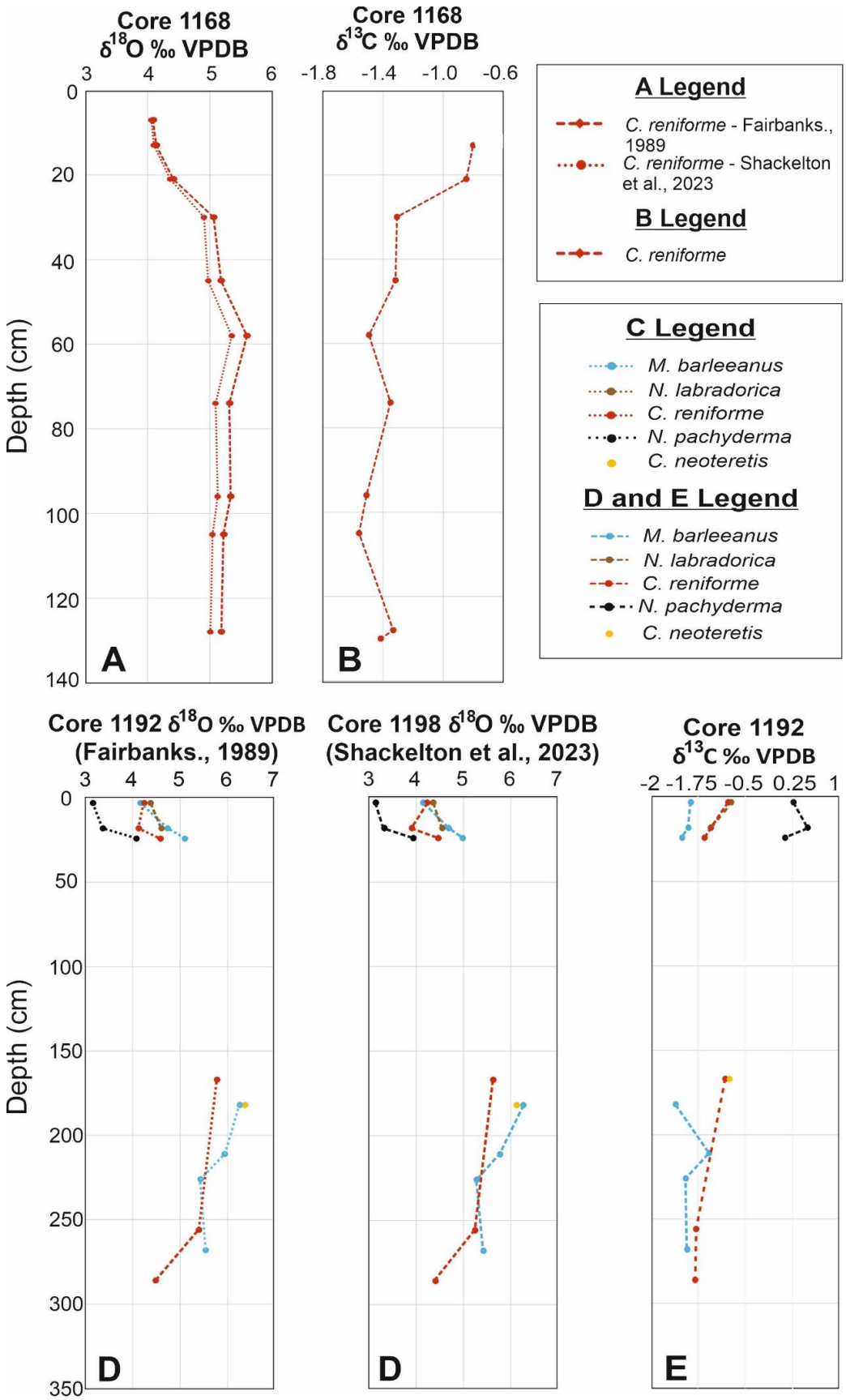
Core 1168
δ18O ‰ VPDB
3 4 5 6
Core 1168
δ13C ‰ VPDB
-1.8 -1.4 -1.0 -0.6
Depth (cm)
0 20 40 60 80 100 120 140
A
B
A Legend
C. reniforme - Fairbanks., 1989
C. reniforme - Shackelton et al., 2023
B Legend
C. reniforme
C Legend
M. barleeanus
N. labradorica
C. reniforme
N. pachyderma
C. neoteretis
D and E Legend
M. barleeanus
N. labradorica
C. reniforme
N. pachyderma
C. neoteretis
Core 1192 δ18O ‰ VPDB (Fairbanks., 1989)
Core 1198 δ18O ‰ VPDB (Shackelton et al., 2023)
Core 1192
δ13C ‰ VPDB
3 4 5 6 7
3 4 5 6 7
-2 -1.75 -0.5 0.25 1
Depth (cm)
0 50 100 150 200 250 300 350
D
D
E

Figure 19: δ18O and δ13C stable isotope results.

Different foraminiferal species were used in this investigation and as such it needs to be considered that different marine organisms will reflect different isotope values. Table 4 shows the species and the correction (if any) that was applied to the lab results.

4.5.1. Investigation into $\delta^{18}O$

4.5.1.1. Core 1168

The species *C. reniforme* were of quality to be measured continuously throughout the core. The FIV and SIV show a maximum and minimum variation in results of 0.38‰ and 0.051‰ respectively. Both results show an increase in value from 13cm to 74cm with 4.8- 5.60‰ (FIV) and 4.5-5.011‰ (SIV). The $\delta^{18}O$ values then decrease in every sample through time from 73cm to 130cm from 5.094‰ to 5.011‰ (FIV) and 5.32‰ to 5.18‰ (SIV).

4.5.1.2. Core 1192

The specimen in this core were not of consistent quality throughout and an emphasis was put on recordings of different foraminiferal specimen $\delta^{18}O$ ratios and so four foraminiferal species *(M. barleeanus, N. labradorica, C. reniforme* and *C. neoteretis)* were used throughout this core, some acting as the only species capable of being preserved well enough to be the only species in a sample. The results of the FIV and SIV measurements have been plotted in Fig. 19 and show similar but slightly different results.

C. reniforme decreases from 3cm to 18cm reading as 4.13‰ (FIV) and 3.91‰ (SIV). The readings at 167cm records a higher value of 5.78‰ and 5.63‰ (FIV) and (SIV). At 256cm it decreases to 5.40‰ and 5.25‰ and at 286cm it measures 4.49‰ and 4.41‰.

The $\delta^{18}O$ results of *M. barleeanus, N. labradorica* and *C. reniforme* all show almost identical recordings at 3cm falling within 0.19‰ (FIV) and 0.15‰ (SIV) of each other.

The measurements of *N, labradorica* aligns quite well with the recordings of *M. barleeanus* for the first two samples at 3cm and 18cm. The FIV recordings of *N. labradorica* and *M. barleeanus* here are 4.38-4.61‰ and 4.17-4.74‰ respectively and the SIV recordings measure 4.36-4.56‰ and 4.15-4.69‰. *M. barleeanus* measures much higher in Unit 3 than in Unit 1 where it peaks at 182cm with a reading of 6.26‰ (both FIV and SIV value) and then decreases downcore.

The one recording of *C. neoteretis* in this sample at 182cm shows a difference of 0.11 (FIV) and 0.14 (SIV) between the recording of *M. barleeanus* in the same sample.

N. pachyderma is a planktic species and although it is on the same graphs it does not signify the same responses as the other benthic species. The Fairbanks., (1989) and Shackelton et al., (2023) results for this planktic species show the same trend for their presence in the top two samples, showing an increase from 3-24cm where the change from 3-18cm was much less significant than the change between 18cm and 24cm.

4.5.2. Investigation into $\delta^{13}C$

4.5.2.1. Core 1168

The $\delta^{13}C$ values in Core 1168 were taken from *C. reniforme* throughout the entire core. Values show a decreasing trend over time, reflecting almost the opposite response. The highest value being recorded as -1.35‰ at 7cm. The $\delta^{13}C$ results show from 7cms the $\delta^{13}C$ ratio decreases, has a peak to -1.35‰ at 74cm, decreases again to 105cm (-1.56‰), has another small peak at 128cm (-1.33‰) and decreases in the final sample to -1.4‰ at 130cm.

4.5.2.2. Core 1192

The $\delta^{13}C$ values in Core 1192 were taken from *M. barleeanus, N. labradorica, C. reniforme* and *C. neoteretis*. The measurements for *N. labradorica* and *C. reniforme* for the first two samples provide similar results (-0.72--1.04‰ and -0.77--1.05‰ respectively). *C. reniforme* shows an increase from Unit 1 to Unit 3 at -1.14--0.81‰, the latter of which

closely correlates with the result of *C. neoteretis* from the same sample at -0.74‰. *C. reniforme* shows little change from 256cm (-1.28--1.3‰).

The $\delta^{13}C$ values for *M. barleeanus* shows a slight decrease from 3cm-24cm and then an increase from 167-182cm BP (to -1.07‰) and then a somewhat increase from -1.45 - -1.4‰ 226-268cm.

The $\delta^{13}C$ values for *N. pachyderma* show an increase from 3-24cm (0.28-0.5‰) and then a decrease to 0.14‰ at 24cm.

4.5.2.3. Stable Isotopes Summary

The recordings for Core 1168 show the clearest and most cohesive response as a result species consistency downcore. The results of $\delta^{18}O$ and $\delta^{13}C$ for Core 1168 have an opposing trend downcore where $\delta^{18}O$ increases as $\delta^{13}C$ decreases.

In Core 1192 all the species present reflect an increase in $\delta^{18}O$ from 3-24cm, reflecting a change in both benthic and planktic environment as the presence of *N. pachyderma* is present. All values are then taken at the next undisturbed interval in Unit 3 where they are all then higher than the previous values.

The $\delta^{13}C$ results again show that as $\delta^{18}O$ increases then $\delta^{13}C$ appears to decrease, however the $\delta^{13}C$ ratio for *C. reniforme* is slightly higher in Unit 3 than it is in Unit 1.

4.6. ^{14}C AMS Radiocarbon Dating and Sedimentation Rates

A total of seven samples across the two sediment cores were selected to under ^{14}C Radiocarbon dating, one sample from Core 1168 and six samples from Core 1192 (Table. 5). The samples have to be corrected for the marine reservoir effect and so a variety of ΔR values were considered (Table 2).

First, a ΔR value of 70±30 was considered (Mangerud and Svendsen., 2017). This was determined using the Calib.org (2024) 14CHRONO Marine20 Reservoir (Heaton et al., 2020) to find the closest available ΔR values. A second ΔR value of 0±0 (Knies et al., 2018)

was also considered due to their close geographical location to the study area. A final ΔR value of -61±37 (Pieńkowski et al., 2022) was considered, as a new publication in a high latitude location.

The overall calibrated values for each sample can be found in Appendices. Four out of seven samples show ΔR=70±30 resulted in the youngest calibrated age and ΔR-61±37 giving the oldest values. However, the rang of date in comparison with the ΔR values shows no consistency in youngest, middle, or oldest calibrated age. The age range given in Core 1168 ranges from 39,661 ± 606 cal yrs BP (ΔR=0±0) to 40,928 ± 601 (ΔR-61±37) with a difference of 1,267 cal years. This is the largest calibrated age range across all seven samples.

The age range for the topmost sample of Core 1192, determining the upper age boundary of the landslide deposit shows a range of 72 cal years from the oldest calibrated age (13,258 ± 171cal yrs BP, ΔR=-61±37) to the youngest 13,186 ± 113 (ΔR70±30). The bottommost sample in Core 1192 measures the oldest possible date for the landslide to have occurred and has a range of 167 cal years (15,211 ± 173 and ΔR=-61±37 to 15,044 ± 171cal yrs BP and ΔR70±30). The samples between these taken from within the slide deposit date material that has already been transported, however it is important to analyse any potential input to the project and the range of these samples vary from 160 to 464 cal years between the calibrated ages.

A decision had to be made to decide which marine reservoir effect correction should be used in this project and due to its close proximity to the study location ΔR=70±30 was chosen. However, because of the close calibrated age ranges, the overall results of the dating in this study does not differ in a way that would change the overall interpretation of these results.

Core	Section	Depth (cm)	Material	^{14}C age	ΔR	±	Calibrated age	Lab Code
1192	1	25	N. pachyderma	11,926 ± 90	70	30	13,186 ± 113	ETH. Nr.142104.1.2 - 1
1192	1	42	Shell fragments	12.908 ± 43	70	30	14,783 ±177	UBA-49899
1192	2	132	Shell fragments	13,226 ± 57	70	30	14,985 ± 128	UBA-49901
1192	2	139	N. pachyderma	19,357 ± 49	70	30	22,859 ± 613	ETH. Nr. 142104.1.2 – 2
1192	2	148	Shell fragments	12895 ± 39	70	30	14,401 ± 171	UBA-49902
1192	2	167	N. pachyderma	13,273 ± 101	70	30	15,044 ± 171	ETH. Nr. 142106.1.2 - 3
1168	2	127-130	N. pachyderma and benthic formainifera mix	36,968 ± 781	70	30	40,803 ± 612	ETH. Nr. 142107.1.1 - 4

Table 5: The ^{14}C AMS radiocarbon ages and the calibrated ages using Marine20 and ΔR=70±30 (Mangerud and Svendsen., 2017).

4.6.1. Core 1168

The age determined for Core 1168 using ΔR=70±30 dates 27-30cm as 40,803 ± 612 cal yrs BP (Table 5). This dates the landslide event beneath as older than this in age, given the unsampled sediment beneath the dated sample and the surface of the landslide deposit.

Assuming the sedimentation rate is continuous and linear, then Core 1168 has a linear sedimentation rate of 3.137cm/kya and add on years of 318.773 yrs/cm downcore. (Table 7).

4.6.2. Core 1192

As mentioned previously, 25cm marks dates the sample using ΔR70±30 as 13,258 ± 171cal yrs BP (Table 4) and the bottommost sample at 167cm marks the base of the landslide as 15,044 ± 171 cal yrs BP. This gives a failure window of approximately 1,786 cal years.

Dates have been taken from within the landslide material which fall between these ages (14,401 ± 171 cal yrs BP at 148cm to 14,783 ± 177 cal yrs BP at 42 cm). One sample at 139cm reads as an outlier at 22,895 ± 613 cal yrs BP within the landslide. This result is not coherent with the rest of the recordings and so it will not be discussed as a potential date for the landslide.

The sedimentation rate for Core 1192 is calculated as 1.896cm/kya assuming the rate is linear and therefore the calculated add on years are 5.27.44yrs.cm downcore (Table 7).

Core	Depth (cm)	Δ Depth (cm)	Age (cal yrs BP)	Δ Age (cal yrs BP)	Linear Sed. Rate (cm/kya)	Add on yrs (yrs/cm)
1168	127	0-127	40,803	40,803	3.137	318.773
1192	25	25	13,186	13,186	1.896	527.44

Table 6: Difference in age with depth for both Core 1168 and 1192. The linear sedimentation rate has been calculated determined from the difference between the dated depth and the top of the core measuring 0cal yrs BP.

5. Discussion

In this section the results will be discussed and interpreted with current literature to determine accurate age analysis and to compare the results of this study with well referenced literature. This section will also have a section dedicated to the multiproxy investigation of material outside of the limits of the landslide to compare environmental parameters to see if this matches with the radiocarbon and calibrated ages.

5.1. Slide Investigation History and Age Investigation

In 1987, Pfirman and Milliman investigated the morphology and oceanography of the Hinlopen Strait and Trough. They noted partial faulting along the strait but none at the trough and comment on the lack of sediment accumulation where they expected to see a trough mouth fan and therefore state it 'presumably little or no sediment was discharged into the Arctic slope from the Hinlopen Trough'.

The first proper investigation into the Hinlopen Slide was by Cherkis et al., (1999) who used Multi-Beam Echo sounding off northwestern Svalbard to present a detailed investigation into the bathymetry from the northern Svalbard margin and the deep embayment at, what they referred to as the Malene Bukta embayment. This investigation highlights the bathymetric detail of the 'U shaped erosional profile' that occurred where the Hinlopen Trough meets the continental shelf. They present a detailed analysis of the escarpment areas and determine the landslide scar was the result of repeated slumping events, the youngest of which had to have occurred no later than the end of the Weichselian as the younger slumps showed little sign of burial. The end of the Weichselian would have seen sea levels begin to rise, the amount of material deposited to the location would therefore be limited as the ending of glacial erosion would lead to less deposition. The lower rate of deposition is therefore the reason why the walls are so steep.

An investigation into detailed mapping of the Hinlopen Slide was undertaken by Vanneste et al., (2006). In this study, swath bathymetry data showed high resolution mapping of a landslide scar at the mouth of the Hinlopen Trough and the morphometry of the turbidite

flow that resulted from the landslide even was. They estimated that a total volume of at least 1,350km3 of sediment had been evacuated into the Nansen Basin. This study also made use of high-resolution seismic profiles to which shows horizontal laminated material at the continental shelf, stacked glaciogenic debris flow deposits in the intermediate area of the slide beyond the bottle neck and post landslide sediment accumulation in the slide scar. In this study, no direct form of dating was investigated, however the seismic profile across the southernmost escarpment scar shows post landslide sediment accumulation. This sediment load is up to 150m thick and therefore contains a significant recollection of glacial material. They assume this to be glaciogenic debris flow deposition which would have occurred when the Hinlopen Strait was an area of ice transport during glacial times and as such they state the assumption that the slide even has to be older than the Holocene and possibly pre-dates the Last Glacial Maximum.

Finally, an investigation into the timing of the Hinlopen Slide was undertaken by Winkelmann et al., (2007). In this investigation they collected material from the distal part of the run-out zone in the Sofia Basin and took PARASOUND profiles from this location to investigate the shallow seafloor at higher resolution. Winkelmann et al., came to the conclusion that there were two acoustic facies to the landslide runout, an acoustically layered unit of normal hemipelagic glaciomarine sediment and the slide debris unit which was acoustically opaque and showed almost no penetration beneath the seafloor.

In Winkelamnn et al's., study, sediment was carefully selected from a site in the Sofia Basin (Fig. 20) and sediment taken from below the turbidite deposit dated to 42,340 ± 2020 ^{14}C years and sediment directly on top of the deposit dated to 25,390 ± 220 ^{14}C years. These results prove the hypothesis Vanneste et al., (2006) that the slide event was pre-LGM, as well as Cherkis et al., (1998) as this dates it to the Kapp Ekholm Interstadial of MIS 3 (Mangerud et al., 1998).

Since this study by Winkelmann et al., (2007) further research into the Hinlopen Slide has not involved the dating of further sediment. It was discussed by Cherkis et al., that a

number of events would have taken place based on the characteristics of the bathymetric data. Vanneste et al., also discussed this when reviewing the escarpment scars at the headwall.

As such the following section will focus on the results of the sediment core analysis, the radiocarbon dating of the two landslide deposits located at the Hinlopen Slide headwall and the environmental conditions at the time of the events. It will also discuss the multi-proxy results to analyse the environmental conditions in the sediment surrounding the turbidite deposits to look for indicators of environmental changes what could support the dates provided.

5.2. Age results from this study

As mentioned previously there are multiple dates that have been determined from two sediment cores. One of which is from Core IG22-1_KOREA-HH-1168. This sediment core is taken from the southernmost slide lobe just off where the Hinlopen Trough reaches into the deep ocean. The location of the core is important to understand, as the core was taken along one of the elongated protruding ridges that stand out high above the surrounding sediment (Fig. 24). These elongated ridges run parallel to the escarpment wall behind and are staggered in size becoming smaller the further from the headwall. Cherkis refers to these ridges as 'Depositional mass flow ridges' and no further investigation into their formation has occurred. The results of the SBP data shows the acoustic reflections to have some backscatter but no penetration and so no theory about these ridges can effectively be discussed with any merit.

A mix of benthic foraminifera and the planktic species *Neogloboquadrina pachyderma (sinistral)* were used to date the landslide deposit at this event with a resulting age of 36,968 ± 781 ^{14}C yrs BP calibrated to 40,803 ± 612cal yrs BP. There is no base date as the sediment core only penetrated a maximum of 40cm into the landslide material. This date opens the discussion about a slide event preceding the event investigated by Winkelmann et al., (2007). It has been the understanding since the initial investigation from Cherkis et al., (1999) that the Hinlopen Slide was one large event followed by

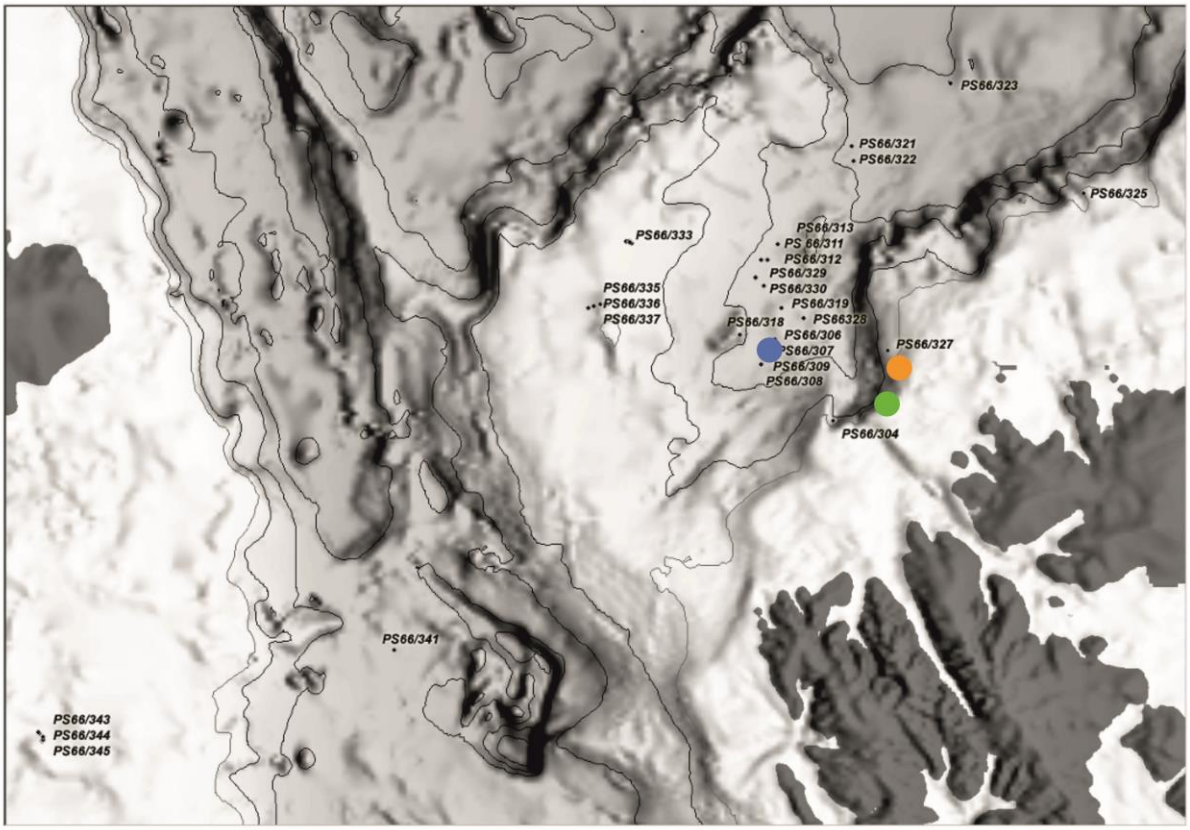

Figure 20: Map showing the location of the dated core samples. Winkelmann et al., (2006) is orange, Core 1168 is green, and Core 1192 is orange. Image taken from Stein., 2005.

several smaller ones based on their bathymetric investigation and then Vanneste et al., (2006) supported this theory.

Winkelmann et al., (2007) discuss the slide event in their study as the main event that resulted in the largest removal or material from the continental shelf. However, now with the understanding that there is an event which occurred even earlier that the one they investigated, it can then be reasonably argued that the main slide event is the one dated in Core 1168.

The location of the dated material from Winkelmann et al., (2007) gives no indication to the location in the headwall of where the landslide came from. Using the Marine20 calibration curve and the same ΔR value as used in these studies their ^{14}C dates have been calibrated to 28,701 ± 253 cal yrs BP above the turbidite and 44,249 ± 1508 cal yrs

BP beneath. This does not change the overall understanding that the material is older than the landslide they are investigating is younger than the material found above the turbidite in Core 1168.

Therefore, at this point of this study, there are two landslide events, one dating to ca. 40ka BP and another at 30ka BP.

The second core investigated in this study is IG22-1_KOREA-HH-1192. This core is taken from the eastern headwall area on the outer proximity of a collection of blocky slump materials. This core is over twice the length of Core 1168 and with it clearly shows a unit of landslide debris.

Shell fragments were taken from within the landslide. These dates provide similar ages of ca. 14.5ka yrs BP. The consistency with these dates suggest material came from the same location during the same period of transportation. However, within the base of the landslide unit is three layers that suggest there could be more than one situation occurring at this stage of the core. The presence of two coarser grained sandy layers that sandwich a layer of silty-mud what differs internally on the X-ray imaging to the rest of the landslide material above it (Fig. 14). There is no coarse material in this mud layer, no small pebbles and no lamination, the x-ray imagery shows the boundaries between these units are not sharp, but they clearly show alternation between deposition of medium grained sand which signifies higher energy or turbidity levels, the mud layer signifying the energy levels decreasing rapidly, the presence of the sand layer again followed by the rest of the huge landslide unit. The base of this unit is angled and erodes into the cohesive silty clay hemipelagic glaciomarine material beneath, which is interesting compared to the sand and mud layers which are mostly horizontally deposited.

This area has been dated, where the material above the top sand layer dates to 14,985 ± 128 cal yrs BP and the mud layer dates to 14,401 ± 171 cal yrs BP. Later, foraminiferal analysis of the sand layer gives a date of 22,859 ± 613 cal yrs BP. The interpretation of this series of events is that the age given for the sandy layer is dating material that has

been transported for a longer period of time than that of the silty-clay mud units that makes up the rest of the landslide deposit.

As Core 1192 shows both the surface of the turbidity deposit and the erosive base, foraminiferal samples using *N. pachyderma* were dated to establish a window for this event. The raw ^{14}C ages of 11,926 ± 90 cal yrs BP and 13,273 ± 101 cal yrs are calibrated to 13,186 ± 113 cal yrs BP and 15,044 ± 171 cal yrs BP. These dates give a narrow window of less than 2ka years where this landslide took place.

5.3. Age Summary and Sequence of Events

In this section, there are now three separate landslide events that are confirmed to have taken place at the Hinlopen Slide Complex. The initial wasting event appears to have taken place in the southern area of the slide, an event which would have evacuated most of if not all of the material in the trough mouth fan. Following this is the event which resulted in the material to the western distal area of the run-out zone into

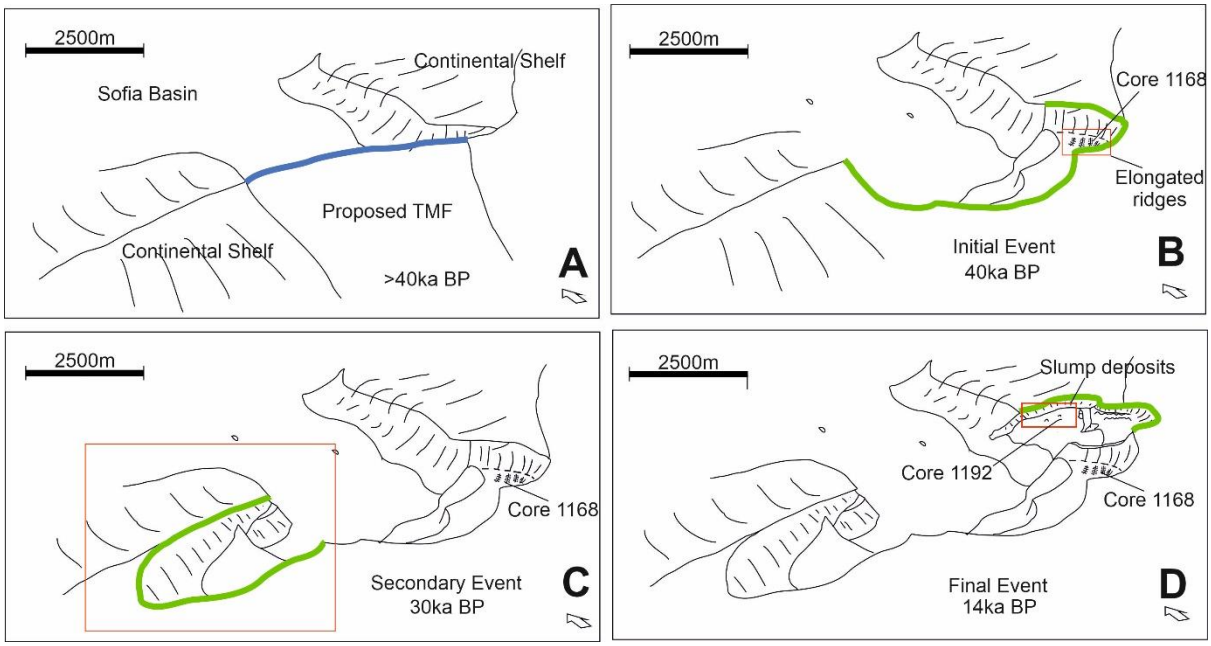

Figure 21: An interpretation of the sequence of failure events of the Hinlopen Slide. The blue line marks the proposed trough mouth fan extent, the green lines represent the newest scar wall and the red boxed identify key areas.

the Sofia Basin. The youngest event occurred from the eastern headwall area over 15ka after the second. Figure 21 shows an interpretation of the sequence of events.

Knowing the location of the youngest event occurred to the western headwall area, then it is safe to presume that the eastern headwall area was the source for the second event. It is possible that the debris flow would have escaped through the bottle neck and spread out laterally over the gentle gradient of the slope just north of the eastern headwall area and into this section of the Sofia Basin. This is supported by seismic imagery analysis of both Vanneste et al., (2006) and Geissler et al., (2016). The slope material in this location shows clear stacked debris flow units towards the deeper slope in Vanneste et al., (2006) and Geissler et al's., (2016) interpretation of the slope on the northeastern side of the bottle neck shows similar debris flow deposits.

5.4. Conditions During Failure

The first and second landslide event both occurred within the Kapp Ekholm interstadial (Mangerud et al., 1998; Winkelmann et al., 2007). This was a warm interglacial period where glaciers on Svalbard would have been similar size to those of present day and waters show higher abundances of organisms that have a preference for warm waters (Mangerud et al., 1998).

The overall understanding that the first main slide event occurred during an interglacial period does not change with the introduction of an older event. What does change however, is that now, the first instance of failure was not at the transition between interglacial-to-glacial climate changes but mid interstadial where any climatic changes occurring from deglaciation (such as glaciotectonic activity, water temperature increasing and sea levels rising) are all now considerable factors leading to the cause of failure.

The youngest slide event confirms both the theories by Cherkis et al, (1999) and Vanneste et al., (2006) as the slide events did occur pre-Holocene and no later than during the Weichselian. This event occurred during the Bølling-Allerød Interstadial, a time of rapid

deglaciation where the glaciers on west Spitsbergen retreated from the continental shelf to the mouth of Isfjorden from ca. 15-14.1ka (Jessen et al., 2020; Svendsen et al., 2004).

The occurrence of this event at this time period can be correlated to the sediment analysis undertaken by Winkelmann et al., (2007) (Fig. 22). The sediment log created shows the turbidite sequence as having occurred at approximately a depth of 2m for a maximum of 80cm. Dates above and below this are known. Also at this location, another date has been taken in the first 1m of the core. This date when calibrated dates to 18,057 ± 123 cal yrs BP. Directly above this dated sample shows an increase in grainsize, however nothing that stans out has having been the result of a second event burying the first. As such it is possible that the evacuation for this third event did not follow the same evacuation pathway which, considering the bottleneck characteristic of the intermediate headwall location is an interesting consideration and the result could potentially be that this last slide event was smaller and the run out was significantly decreased as a majority of material had already been removed for the easter headwall area from the first main event. This could have been the result of the continental shelf towards the east being unsupported of returning to an equilibrium that was lost during the earlier events.

The rapid warming event was the result of changes to the Atlantic Meridional Overturning Circulation which then in turn has a knock on effect worldwide (Rosen et al., 2014). The B-A interstadial can be see in the results of the Greenland Ice Core (GRIP Members., 1993), seen by a significant rise in $\delta^{18}O$ values at around 14.7ka BP (Fig. 23). This signifies that the likely cause of failure for this event was the result of rapid cooling of temperatures into the LGM and then a rapid rise in temperature during the B-A Interstadial, which would have had glaciotectonic repercussions as material at the seafloor adjusted to the changes in temperature, sea level and ice cover.

A comparison of the dated slide material has been compared with the $\delta^{18}O$ results of the Greenland ice core and each date is located after a rapid increase in $\delta^{18}O$ values. An increase in $\delta^{18}O$ values is a signifier of warmer conditions, as less of the lighter ^{18}O is trapped in ice. This describes the fact that all three slide events have occurred during

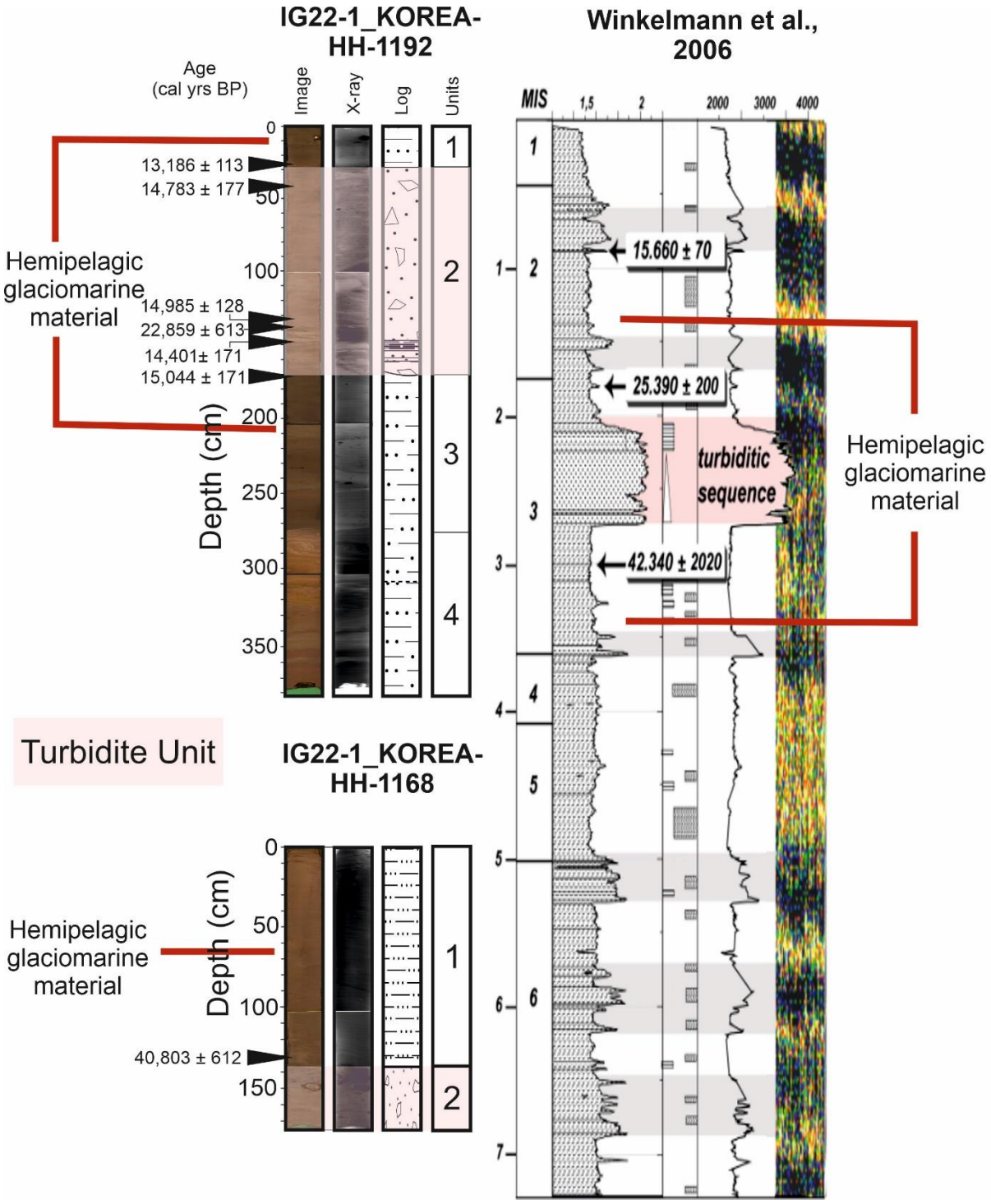

Figure 22: Sediment gravity cores from this study compared to the stratigraphic log in Winkelmann et al., (2007).

periods of warmer global climates, during interstadials and deglaciations. A date that does not fall with this trend is the date taken from beneath the landslide in Core 1192 which is understandable, as this was a pre-slide date and if the failure mechanisms are somehow connected to the increasing temperature then its position in this graph is in order with this studies understanding of the slide events. The base date from Winkelmann et al., (2007) does occur after an increase in $\delta^{18}O$, however the time between peak $\delta^{18}O$ and the date is over 2ka, as opposed to the three other dates that all fall within 1ka years. (Fig. 23).

The response of deglaciations on the surrounding continental shelf would have had a variety of impacts which could have lead to an eventual failure.

During Cherkis et al's., (1988) investigation, they regarded the possibility that buried gas could have had some influence on failure. The gas hydrate stability zone can be seen in seismic imaging and Bottom Simulation Reflections (marking the location of buried gas in the sediment) could be seen in the continental shelf surrounding the headwall. They proposed that as the slide falls within the Gas Hydrate Stability Zone (GHSZ) that during periods of lower sea levels or warmer temperatures, the depth at which both of these things can be found will change (being influenced by temperature and pressure) and so gasification of hydrates is a possibility which could then move up partially faulted glaciomarine deposits and weaken the material support. This was also investigated by Geissler et al., (2016). They located the BSR at a depth of approximately 240m, the depth at which Vanneste et al., (2006) suggested could have been the depth of the failure plane. No confirmation of the BSR has been seen in seismic reflections directly beneath the slide scar (Winkelmann et al., 2007) however Geissler et al., (2016) and Winkelmann et al., (2007) believe that this is a strong possibility of being at least part of the cause of failure as gas flares have been identified both to the continental shelf to the north and south of the slide scar. It is believed that the gas would have escaped through existing fault planes as there is no evidence of pockmarks or explosive action anywhere in the vicinity of the scar.

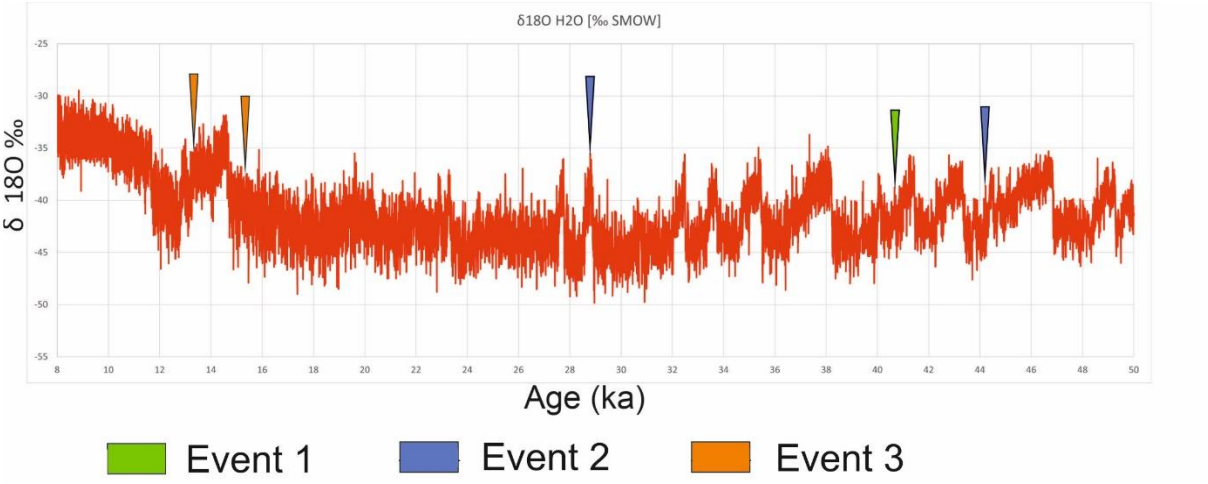

Figure 23: Results of the Greenland Ice Core δ18O values going back the last 50ka years (GRIP Members., 1993). The dates of the three landslide events have been marked by arrows.

5.5. Lithological comparisons

PARASOUND and seismic data collected during past investigation into the Hinlopen Slide shows the presence of two acoustic facies; one being the slide debris which is acoustically opaque and shows no internal structures of any kind, and the other being hemipelagic glaciomarine sediments which appear as acoustically layered units with somewhat deep penetration (Winkelman et al., 2007). These two facies can also be seen in the SBP data used in this study (Figs. 10 and 24).

The SBP Composite lines seen in Fig. 24. Show the variation in morphology of the seafloor landscape at the two core locations (A and B) and the 'undisturbed' continental slope to the north. Only one of the SBP lines showed any penetration beneath the seafloor at all across the Hinlopen Slide and that was the line trending N-S trough the in the W-E transect (the location of the composite lines are marked in Fig. 9). The seismic data from Winkelmann et al., then proves that the horizontally laminated deposits are

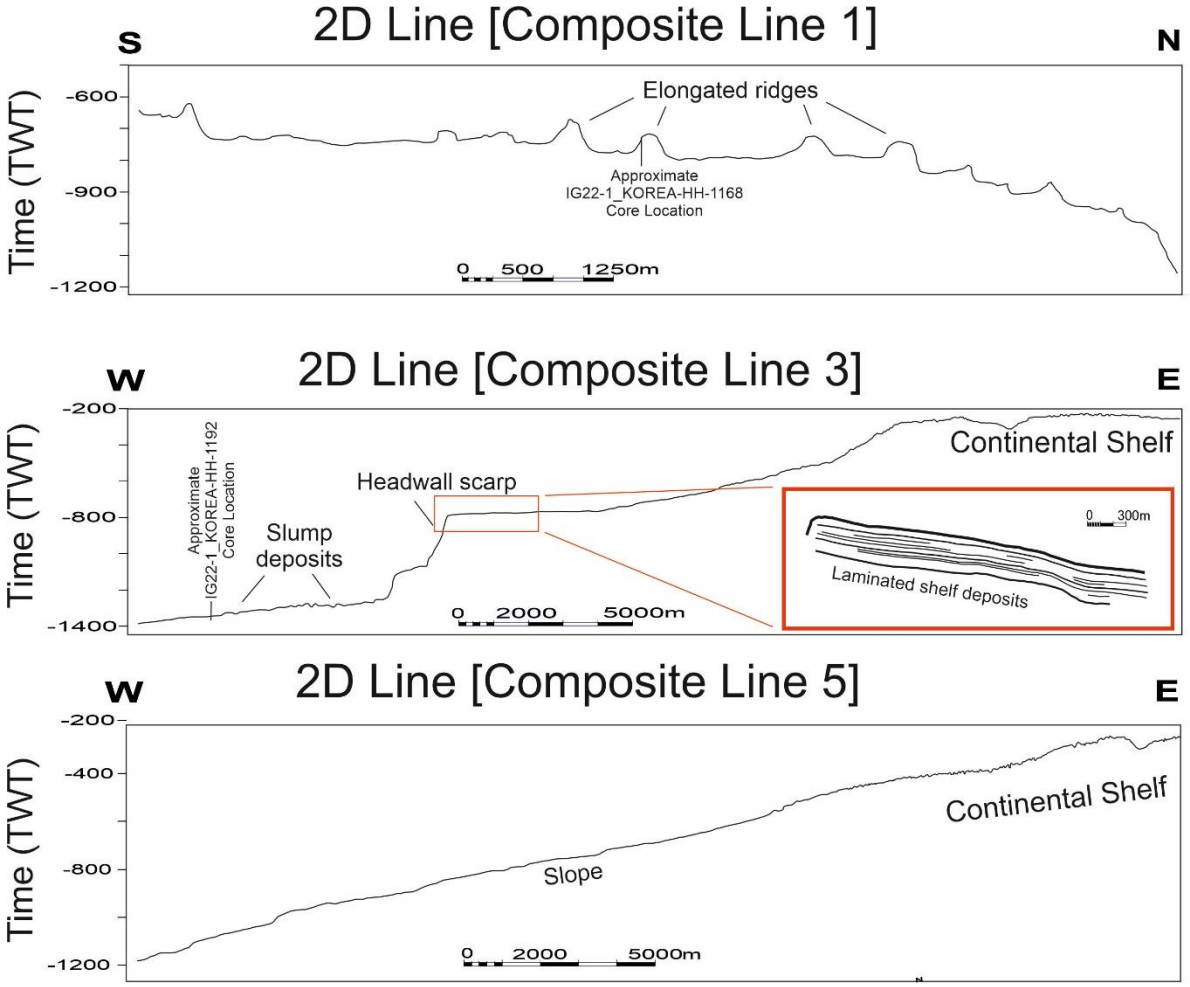

Figure 24: Three composite lines inspired from the SBP composites showing the different characteristic of the locations of the two sediment cores and the undisturbed continental slope.

continuous across the shelf. The slide embayment results in no penetration and there have been no seismic data taken from the deeper ocean part of the headwall scar area. Seismics in the distal location, however, show that the thickness of the slide unit is at least 200m thick in some places (Winkelmann et al., 2007).

The sediment cores that have been taken and investigated in this study both contain a top unit of hemipelagic glaciomarine silty-clay which is undisturbed. In Core 1168 this unit is approximately 136cm thick and in Core 1192 it is only 26cm thick. The landslide unit in both cores show different internal characteristics in X-ray and was the initial though for multiple slide evens as Core 1168 contains a much darker x-ray unit with large pebbles and clasts showing no orientation and little variation in grain size outside of

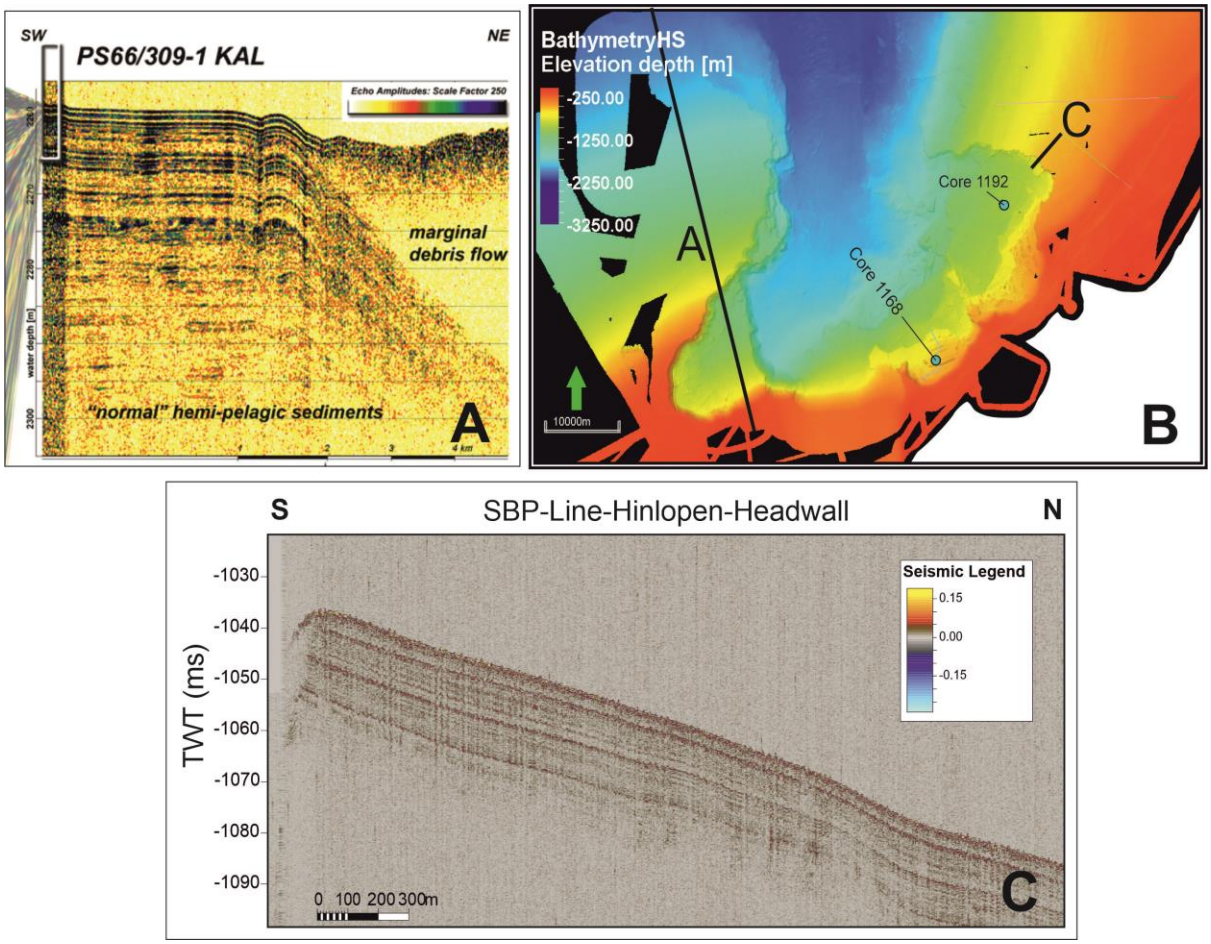

Figure 25: Comparison between the PARASOUND results of Winkelmann et al., (2007) (A) with the SBP data used in this study (C).

these larger clasts. On the other hand, Core 1192 turbidite did not contain such large clasts and contained mostly a thick layer of small pebble debris throughout as well as the layers of sand and mud mentioned previously. The different characteristics of these two units indicated, before being dated, that the material likely came from two different events (examples of the pebbles and coarser material can be seen in Fig. 12).

A comparison has been made of the two sediment cores in this study with the sediment log taken from Winkelmann et al., (2007) seen in Figure 22. Their log shows the turbidite sequence as being a period of graded material sandwiched between finer grained hemipelagic muds. The same comparison can be made with Core 1192, where the grain size variation from Units 1, 2 and 3 do not differ too greatly however there is a significant

amount of coarser material to be found withing the landslide deposit. The Core 1168 shows the same trend as the top boundary between the landslides in Winkelmann et al., log and the Core 1192. Both Winkelmann et al., and Core 1192 show a thick unit beneath the landslide of fine silty-clay material with the occasional intersection of higher percentage of coarser grained material (Fig. 13). Winkelmann et al., sedimentary log does show greater variation in lithology and grain size compared to those in this study but in terms of comparison, the log and Core 1192 show very similar aspects.

5.6. Failure Mechanisms

As discussed in the previous section, there have been a variety of theories over the years as to what failure mechanism led to the Hinlopen Slide event. It appears to be accepted that there is no one singular mechanism that triggered the event and it was likely the result of a variety of environmental and climatic factors.

Cherkis et al., (1998) first introduced the theory that the influence of gas present at the continental shelf at the location of the headwall could have some factor in the failure. They suggested that hydrate-gas decollement mechanism has the potential to occur as a result of sea level changes, temperature increase and abnormally high pulses of gas flowing up towards the surface. There is no evidence in the slide location of pockmarks or explosive action, so unless this occurred within the material that was evacuated there is no evidence to confirm a rapid expulsion of gas to be a trigger.

It is much more likely that if gas and the GHSZ had a role to play in the failure of the slide that gas would have escaped through partially faulted sediment on the continental shelf (Geissler et al., 2016; Vanneste et al., 2010).

Another possible mechanism that has been discussed in literature is tectonic activity and faulting. The location of the study area near the Molloy Ridge means that the surrounding area is partial to tectonic faulting. However, the study location itself does not show any evidence of faulting directly near the headwall location. The Moffen Fault runs across the continental shelf between the shelf edge and Svalbard however there is no evidence that the fault has been reactivated during the periods that the slide event

occurred, and no evidence has been introduced that any large scale earthquakes have occurred in the proximity to the study location over the Weichselian. It has been argued, however that the sediment walls separating escapement lobes are the result of vertical fault planes (Winkelmann et al., 2007) instead of partially faulted sediment. Seismic investigation into the continental shelf north or the slide scar show multiple instances of internal deformation and shear zones of strongly deformed sediment (Geissler et al., 2016).

There is the potential for glacio-tectonic activity to have been a factor in the triggering the landslide failure events. The repeated change between glaciated and deglaciated margins means as a result that the sediment at the seafloor undergoes repeated cycles of ice loading and release. An increase in ice volume increases the pressure on the seafloor below and at this location the ice loading is asymmetrical across the shelf at the Hinlopen trough (Winkelman et al., 2007). As the material undergoes a cycle f loading and unloading it is common for weaknesses to form which could contribute to the eventual failure.

As all three slide events occurred during warmer interstadial and deglacial conditions, it is not unreasonable to assume that a large factor towards failure was a collective contribution to conditions that act as a result of a warming climate, such as unloading following glacier melt, increase in ocean temperatures, and as such, a change in the location of the GHSZ and the BSR. During or after glacial loading, it is possible that some material experienced faulting to relieve pressure and during the interstadial as the loading was reduced the material failed along these planes of weakness. As there has been no identified slide event which aligns with colder glacial periods then it could be suggested that those are more likely favourable conditions that ensured higher levels of stability. It is also possible that the warmer temperatures changed the location of the GHSZ and BSR and so hydrates at shallower depths melted to do warmer conditions and wither the pore pressure changed or the gas escaped, both of which could be potential factors.

5.7. Multi-Proxy analysis

5.7.1. Foraminifera Ecological Environments

This section will focus on the results of foraminiferal analysis from samples taken in undisturbed sediment down both cores. Samples have been identified when possible to species level, however in some instances it has only been possible to specify to genera level and the individual will then be referred to as, for example, *Cassidulina sp.*, if it is not possible to identify further.

In order to undertake this investigation a variety of sources have been used to identify as accurately as possible, these include the World Register of Marine Species (WoRMS Editorial Board., 2024), and Kujawa et al., (2021). The most abundant species of foraminifera will be outlined and discussed below.

5.7.1.1. Benthic Foraminifera

5.7.1.1.1. *Cassidulina reniforme* (Uchio, 1960)

Cassidulina reniforme is an infaunal benthic foraminiferal species which live in the topmost layer of sediment along the seafloor and are a common species found in the arctic due to their preference for colder temperatures (Hald and Vorren., 1987). It is a common species which is found in glaciomarine environments, found to thrive in laminated mud deposits with low turbidity, and is known to inhabit environments where cold bottom waters are present, specifically the cooler Atlantic Waters (Hald and Korsum., 1997HT). The tolerance for this species is an environment where there is seasonal sea-ice cover, a temperature of less than 2°C and low salinity (Hald and Korsun., 1997; Polyak et al., 2002 HT).

5.7.1.1.2. *Melonis barleeanus* (Williamson., 1958).

Melonis barleeanus (accepted name: *Melonis affins* (Reuss., 1851) but referred to throughout this study as *M.* barleeanus)is an infaunal benthic foraminifera species which live in the topmost layer of the sediment along the seafloor and are a common arctic-subarctic species (Jennings et al., 2004 T; Corliss 1991HT) preferring cooler waters and found in areas with absent or seasonal sea-ice in areas with high sedimentation rates in

fine and muddy sediment in shelf depressions and on continental slopes (Hald and Steinsund., 1992; Korsund and Hald., 1998HT).

It is a species which indicates productivity as it feeds on organic matter and prefers a steady supply of food (Hald and Steinsund., 1992), although it can adjust its living parameters to persevere through unfavourable conditions due to their tolerance of a range of environmental conditions (Linke and Lutz., 1993).

With an organic food source the presence of this species has been higher in sediments with a higher percentage of organic matter which show the sign of partial dissolution and transportation from shallower marine environments (Polyak and Mikhailov., 1996).

Melonis barleeanus is therefore a species which can be used to distinguish times of higher productivity, input of cooler Atlantic Water, and changes in levels or organic carbon.

5.7.1.1.3. *Cibicides lobatulus* (Kanmacher. ,1798)

Cibicides lobatulus (accepted name: *Lobatula lobatula* (Kanmacher., 1978) but referred throughout this study as *C. lobatulus*) is a benthic foraminifera that attaches itself to substrate, coarse grained sediments, shells etc. and lives above (Hald and Vorren., 1987; Polyak et al., 2002), and within the very top sediment layer (Zajączkowski et al., 2010) this means they are commonly found in sediments with a larger grain size (Korsund and Hald., 1998; Sejrup et al., 1981; Polyak et al., 2002) and therefore prefers environments with higher levels of turbidity and energy such as colder more turbulent Atlantic water inflow (Hald and Steinsund., 1992; Wollenburg and Mackensen., 1998).

C. lobatulus is found in shallow marines with a preference for glacially distal environments (Hald and Korsum., 1997; Polyak et al., 2002). However, as it is a species which attaches itself to sediment withing areas with higher levels of turbidity and so can be used as an indication of strong bottom water currents. It is also prone to high levels of transportation and bioturbation when looking for food (Zajączkowski et al., 2010; Ivanova et al., 2008) and as such should be used carefully if specimen show signs of

transportation. In terms of temperature, *C. lobatulus* is known to indicate warmer or colder waters.

5.7.1.1.4. *Buccella frigida* (Cushman., 1922)

Buccella frigida are an arctic species which are either epifaunal or shallowly infaunal (Rosoff et al., 1992). It prefers colder temperatures however it is known to survive in environments slightly warmer and so can be widely distributed through low-moderate temperatures (Polyak et al., 2002). *B. frigida* feed on algal blooms which occur at the sea ice edge and respond to the availability of food in these locations (Seidenkrantz., 2013; Polyak et al., 2002).

This species is usually found in coarser grained sandy sediment and is not tolerable in areas of high turbidity (Zajączkowski et al., 2010). As a species which is distributed by abundance of food it can be used as an indicator of productivity.

5.7.1.1.5. Other Benthic Species Ecological Indicators

Species	Species preferences and environmental indicators
A. gallowayi (Loeblich and Tappen., (1953)	Epifaunal (Wollenburg and Mackensen., 1998), higher turbidity and coarser material (Jennings et al., 2004), on continental shelves, similar distribution as *C. lobatulus* (Polyak et al. 2002).
C. neoteretis (Seidenkrantz., 1995)	Glaciomarine sediments (Mackensen and Hald., 1988), colder chilled Atlantic waters (Polyak and Mikhailov., 1996), on continental shelves and slopes, seasonal ice-free conditions (Wollenburg and Mackensen., 1998).
C. laevigata (d'Orbigny., 1826)	Preference for warmer and relatively saline waters, can indicate the presence of warmer Atlantic waters (Mackensen

	and Hald., 1988), glaciomarine environment (Steinsund and Hald., 1994).
N. labradorica (Dawson., 1860)	Sometimes epifaulnal and feeds on buried organic matter, an indicator of high productivity, indicates proximity to the Polar Front (Polyan and Mikhailov., 1996), can indicate the transition from glaciomarine (Hald and Vorren., 1987).

Table 7table : Species preferences and environmental indicators for secondary benthic foraminifera species in this study.

5.7.1.2. Planktic Foraminifera

5.7.1.2.1. *Neogloboquadrina pachyderma* (Ehrenberg., 1861)

Neogloboquadrina pachyderma (commonly referred to as *Neogloboquadrina pachyderma (sinistral)* is the most dominant planktic foraminifera species to be found in the Arctic (Bé and Tolderlund., 1971). This is a polar species which is an indicator of cold waters and acts as an indicator temperature and sea ice indications as well as other climate variation factors and as such changes in abundance through time reflect the changing climates (Broecker et al., 1990).

5.7.1.2.2. *Neogloboquadrina incompta* (Cifelli., 1961)

The species *Neogloboquadrina incompta* is commonly referred to as *Neogloboquadrina pachyderma (dextral)* as it is looks morphologically similar to *N. pachyderma (sinistral)* however the coiling direction of the test is to the right (dextral) instead of to the left (sinistral). This species will be referred to as *N. incompta* throughout this study.

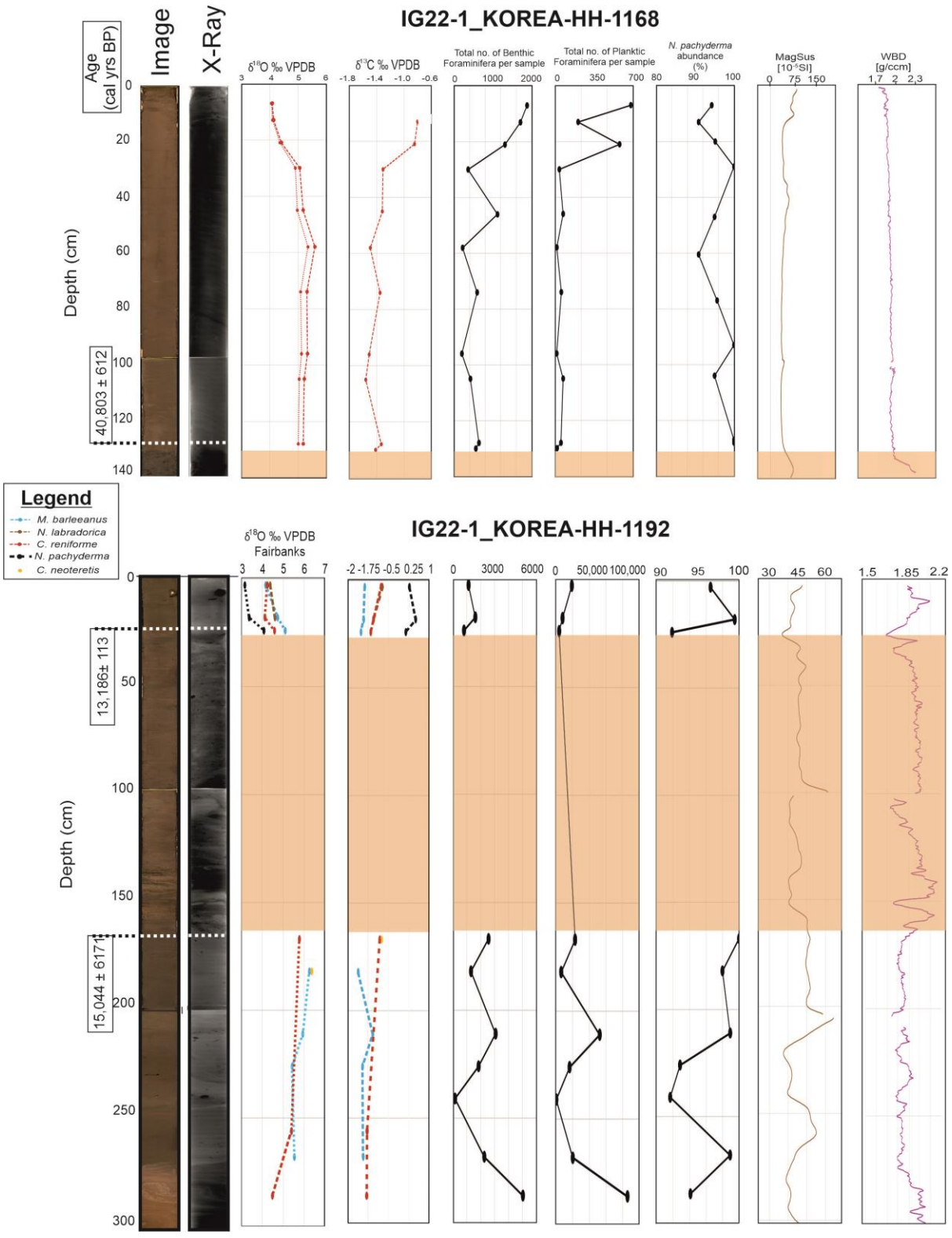

Figure 26: A comparison between the stable isotope results, foraminiferal results and MSCL results.

N. incompta is a planktic species that prefers warmer waters and has the opposite environmental preferences as *N. pachyderma* and so can be used in collaboration to determine changes in temperature and to show the influence of warmer Atlantic Water inflow (Bé and Tolderlund., 1971).

5.7.1.2.3. *Turborotalita quinqueloba* (Natland., 1983)

Turborotalita quinqueloba is a planktic species which is sound in sub-polar waters and is associated with the oceanic fronts (Bé and Tolderlund., 1971; Johannessen et al., 1994). It is a species abundant in Atlantic surface waters (Rasmussen and Thomsen., 2010) and can be an indicator of Atlantic water inflow after colder glacial events (Bauch., 1994).

5.8. Foraminiferal abundance comparison

The most abundant species found in Core 1168 are species with a preference for cold waters such as *C. reniforme, M. barleeanus, C. neoteretis, N. labradorica* and *B. frigida* however there is also an interesting abundance of *C. lobatulus* in younger sediment. *C. lobatulus* prefers warmer waters and *B. frigida* has a preference for colder waters and an interesting correlation between these two species shows than in samples with higher amounts of *C. lobatulus* the abundance of *B. frigida* is lower and vice versa. *M. barleeanus* has very similar abundances throughout the unit and as an indicator for productivity this could signify a constant stream of food supply. Another species that acts as an indicator for productivity is *B. frigida* which shows more variation towards the younger samples.

Over 90% of every sample has *N. pachyderma* as the most abundant planktic species. This species being the most common arctic species is unsurprising. The presence of *N. incompta* and *T. quinqueloba* in some samples shows a slight species diversity, however, when regarding the actual number of individuals, the increase in percentage of these species in this core are typically the result of one individual within a sample with a small number of specimens.

The most abundant species in Core 1192 are similar to those in Core 1168 *(C. neoteretis, M. barleeanus, C. lobatulus, N. labradorica)* however the presence of *Islandiella norcrossi* and *C. laevigata*. *I. Norcross* is another cold-water species which is inclined towards higher productivity locations and this along with *N. labradorica* imply that the levels of productivity pre-slide event was much higher than those post-failure.

C. laevigata is a warm water indicator and usually the variation between them and *C. neoteretic* can be used as indicators of temperature change. In this location the distribution of *C. laevigata* is low in the deepest samples, however this is also the sample that has the highest abundance of *C. neoteretis*.

5.9. Stable Isotopes $\delta^{18}O$ and $\delta^{13}C$

Results of stable isotope analysis in Core 1168 shows a slight increase in $\delta^{18}O$ from the base of the hemipelagic glaciomarine unit to about halfway up the core. This marks the peak $\delta^{18}o$ value and from this point on the readings decrease. In the sample with peak $\delta^{18}O$ values, the total number of benthic foraminifera actually decreases compared to the samples surrounding it, planktic foraminifera is also in low abundance, however the percentage of cold water planktic species *N. pachyderma* does decrease in this sample. There is no change in magnetic susceptibility or wet bulk density that can indicate any parameters involved here. A decrease in $\delta^{18}O$ is matched with an increase in $\delta^{13}C$. The total number of benthic foraminifera show the same trends and peaks as the $\delta^{13}C$. This is also the case for planktic foraminifera however the scale is just much smaller. The δ13 increase is a signifier to an increase in productivity and so matching trends between the two are a good signifier to that degree.

Core 1198 shows $\delta^{18}O$ values in pre- and post-landslide material. In the top glaciomarine unit, there is a decrease in $\delta^{18}O$ from 24cm to the topmost sample at 3cm. much the same as Core 1168, this is also matched with an overall increase in $\delta^{13}C$ which also aligns with an increase in planktic and benthic foraminifera. In this core, the trend of benthic and planktic foraminifera match very well with the $\delta^{13}C$ values for *M. barleeanus* beneath

the slide deposit and interestingly the trend in Unit 1 above the landslide the total number of benthic foraminifera match up with the $\delta^{13}C$ values from *N. pachyderma*.

N. pachyderma was only used in Core 1192 above the landslide deposit for isotope analysis but values for the $\delta^{18}O$ and $\delta^{18}O$ follow similar trends as the benthic species indicating that there is no such disparity between the two environments.

5.10. Tsunami Generation

The quick onset and offset of the colder Younger Dryas period into the modern Holocene did not result in sediment evacuation that has been discovered so far, however it is an important fact to consider regarding the future of exploration in the Arctic.

The scale of the material transported during the Hinlopen Slide Complex was so immense that it is almost certain that an evacuation would result in exchanges of enough energy and displace so much water that it would have generated a tsunami. Research using the dates provided by Winkelmann et al., (2007), Vanneste et al., (2011) investigated the geomorphology of the slide and simulate potential tsunami occurrences. In their simulations, they reveal that it is likely the main event only took place over the period of one hour. That is an incredibly large volume of sediment to move in such short a time and a tsunami propagation as a result would not be surprising. Simulations show a potential tsunami that would have reached the eastern coast of Greenland within one hour of failure (Fig. 27) and propagate across the entirety of the Arctic Ocean within three hours of the failure event.

The location of the site means that propagation into the North Atlantic would have been diminished by Greenland and Svalbard and the Barents Sea would not have been affected until over six hours later. The sea surface elevation would have increase by 10m and decreased by 2m from the peak and trough of the tsunami waves.

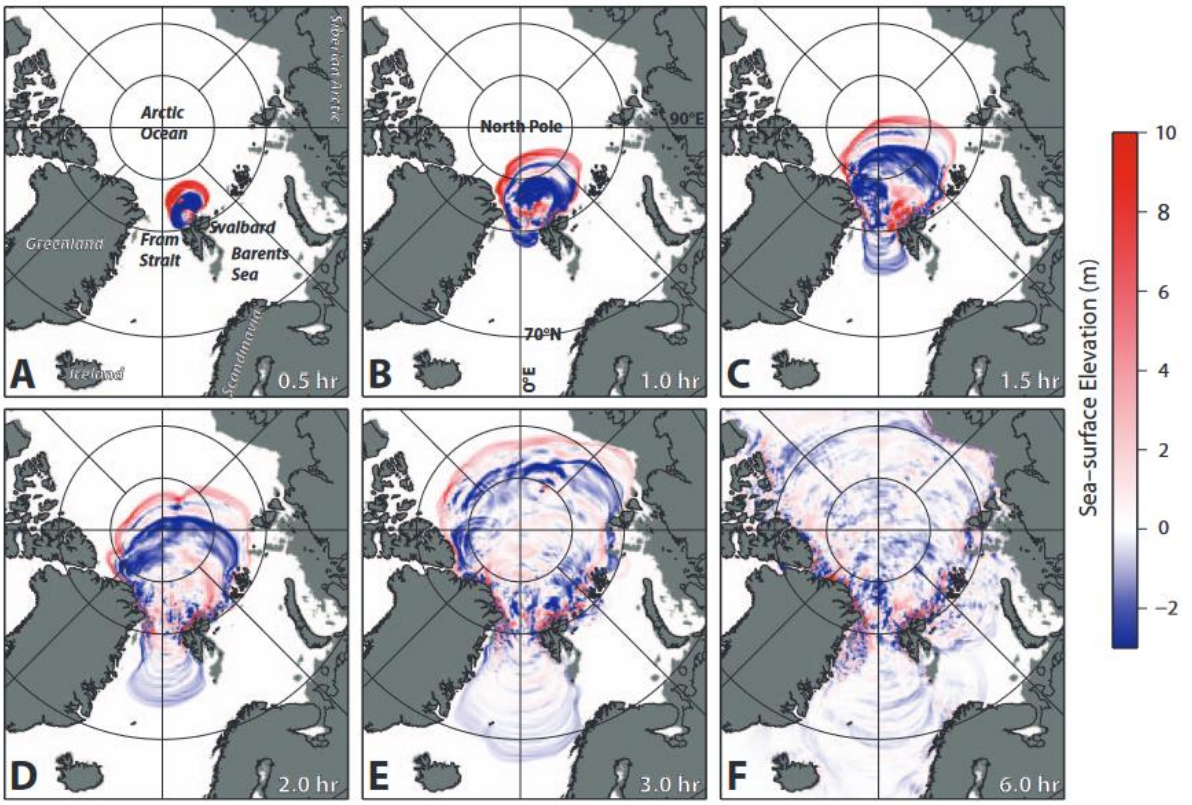

Figure 27: Tsunami generation simulation for the main landslide event (Vanneste et al., 2010).

5.11. The Future

The three landslide events that are now known to have occurred in the Hinlopen Slide Complex are dated to ca. 40ka, 30ka, and 14ka. Investigations into a variety of factors such as dating, geomorphology, seismic investigation, and overall mapping indicate that interest in this landslide location is an area of interest, especially being the largest landslide formation in the Arctic (Cherkis et al., 1996; Vanneste et al., 2006; Winkelmann et al., 2007; Winkelmann et al., 2007; Winkelmann et al., 2008;Geissler et al., 2016). However, one investigation brings up an important factor to consider to the future stability of this site. It can be seen in the bathymetry in the slope surrounding the slide

scar that there is evidence of surface cracks trending NE-SW (Figs. 9; Geissler et al., 2016). Seismic investigation into this area shows that internally within the

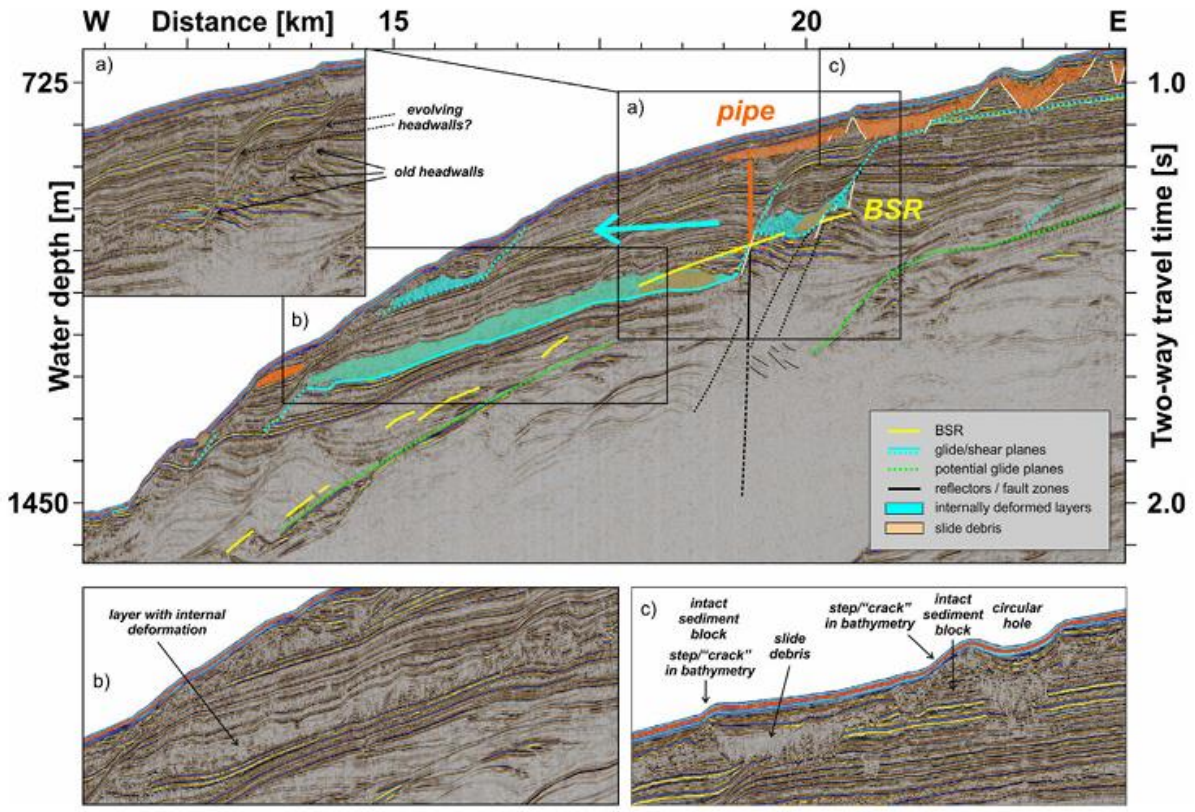

Figure 28: Interpretation of a seismic profile taken from north of the scar location with interpretations from Geissler et al., 2016). The location of this seismic profile is similar to that of Composite Line 5.

sediment there is frequent occurrence of slide debris and internal deformation (Fig. 28). The presence of these internally deformed structures in a location where there has been multiple large-scale landslide event introduces the possibility that the failure event could be incomplete and that an unknown time in the future could see another failure event on the northern side of the existing scar.

The quick onset and offset of the colder Younger Dryas period into the modern Holocene did not result in sediment evacuation that has been discovered so far, however it is an important fact to consider regarding the future of exploration in the Arctic.

It is no surprise from the scale of the material transported during the Hinlopen Slide Complex that an evacuation would result in exchanges of energy and generate a tsunami. Research using the dates provided by Winkelmann et al., (2007), Vanneste et al., (2011) investigated the geomorphology of the slide and simulate potential tsunami occurrences. In their simulations, they reveal that it is likely the main event only took place over the period of one hour. That is an incredibly large volume of sediment to move in such short a time and a tsunami propagation as a result would not be surprising. Simulations show a potential tsunami that would have reached the eastern coast of Greenland within one hour of failure (Fig. 27.) and propagate across the entirety of the Arctic Ocean within three hours of the failure event.

The location so far north means that the impact of such an event occurring again should the remaining material to the north of the slide scar fail means that the social and economic impact will be much smaller than, for instance, a repeat of the Storegga tsunami (Vanneste et al., 2010; Geissler et al., 2016)

Although it is unlikely that as much material will be transported I such a manner again, this was, after all, an investigation into the first largest event, even if the secondary events also resulted in tsunamis, there is no guarantee that they would have the same impact.

6. Conclusion

In conclusion, a total of two sediment gravity cores were analysed in this study to determine the age and investigate the Hinlopen Megaslide. The sediment cores show two different lithological turbidite deposits, one containing large pebbles and debris and the other having smaller debris particles and internal layering of coarser sand-mud-sand layering.

Two different landslide events have been identified, one from the southern lobe dating to the Middle Weichselian Kapp Ekholm Interstadial at 40ka yrs BP and the second event was taken from the eastern headwall area and a time window from 15-13ka has been confirmed.

These dates, along with the results of Winkelmann et al., (2007), totals the number of slide events to three at current. The understanding that the 30ka yrs BP slide event dated by Winkelmann et al., was the main slide event has now been challenged by the results of this study.

All three slide events occurred during warmer climatic events, the Kapp Ekholm Interstadial and the Bølling-Allerød Interstadial. This implies that the effect of a warmer climate has a large impact of the stability of the material at the continental slope in this location.

The results of Geissler et al., (2016) highlights the possibility of future failure events due to the presence of strongly internally deferment sediment in the continental slope just north of the slide scar and repeated evidence of slump deposits. As a result, although a landslide here would not have too much of a social or economical impact it is something to be considered for further research in the Arctic.

7. References:

Allaart, L., Patton, H. and Esteven, M., (2023). *Chapter 50: The Eurasian Arctic: glacial landforms from the Younger Dryas(12.9-11.7ka)*. In: Palaceios, D., Hughes, P.D., Garcia-Ruiz J.M. and Andrés N., (2023) *European Glacial Landscapes*. Elsevier. 473-479.

AMAP and Icelandic Marine Research Institute., (2016). *Arctic Ocean Current Circulation*. [Image Online] Available at: https://arcticportal.org/maps/download/maps-arctic-sea-ice/2447-arctic-currents. Through: *Arctic Portal*. [Accessed: 10/02/24].

Armstrong, H.A. and Brasier, M.D., (2004). *Chapter 4: Microfossils, Stable Isotopes and Ocean-Atmosphere History*. In: Howard, A., Armstrong, H.A., and Brasier, M.D., (2004) *Microfossils*. 2nd Ed. Blackwell Publishing Ltd. Oxford. 25-34.

Batchelor, C.L., Dowdeswell, J. and Hogan, K.A., (2011). *Late Quaternary ice flow and sediment delivery through the Hinlopen Trough, Northern Svalbard margin: Submarine landforms and depositional fan*. Marine Geology. (284). 13-27.

Bauch, H.A., (1994). *Significance of variability in Turborotalita quinqueloba (Natland) test size and abundance for palaeoceanographic interpretations in the Norwegian-Greenland Sea*. Marine Geology. (121) 1-2. 129-141.

Bé, A. and Tolderlund, D., (1971). *Distribution and ecology of living planktonic foraminifera in surface waters of the Atlantic and Indian Oceans*. The Micropalaeontology of Oceans. 105-149.

Boggild, K., Mosher, D., Travaglini, P., Gebhardt, C. and Mayer, L., (2020). *Mass wasting on Alpha Ridge in the Arctic Ocean: new insights from multibeam bathymetry and sub-bottom profiler data*. Geological Society, London. Special Publications. 500.

Bondevik, S., Svendsen, J.I. and Mangerun, J., (1997). *Tsunami sedimentary facies deposited by the Storegga Tsunami in shallow marine basins and coastal lakes, western Norway*. Sedimentology. (44). 1115-1131.

Brendryen, J., Haflindason, H., Yokoyama, Y., Haaga, K.A. and Hannisdal, B., (2020). *Eurasian Ice Sheet Collapse was a major source of Meltware Pulse 1A 14,6000 years ago*. Nature Geoscience. (13). 363-368.

Butt., F.A., Elverøi, A., Solheim, A. And Forsberg, C.F., (2000). *Deciphering Lare Cenozoic development of the western Svalbard Margin from the ODP Site 986 results*. Marine Geology. (169) 3-4. 373-390.

Calib.org (2024). *14CHRONO Marine20 Reservoir Database*. [Online] Available at: http://calib.org/marine/ [Accessed 09/05.24].

Canals, M., Lastras, G., Urgeles, R., Casamor, J.L., Mienert J., Cattaneo, A., De Batis, M., Haflidason, H., Imbo, Y., Laberg, J.S., Locat, J., Long, D., Longva, O., Masson, D.G., Sultan, N., Trincardi, F. and Bryn, P., (2004). *Slope failure dynamics and impacts from seafloor and shallow*

sub-seafloor geophysical data: case studies from the COSTA project. Marine Geology. (213). 9-72.

Cherkis, N.Z., Max, M.D. and Vogt, P.R., (1999). *Large scale mass wasting on the north Spitsbergen continental margin, Arctic Ocean*. Geo-Marine Letters. (19). 131-142.

The Chrono Centre., (2024)., *About Radiocarbon Dating: About AMS*. [Online} Available at: https://14chrono.org/radiocarbon-dating/about-ams/ through 14Chrono, Queens University Belfast. [Accessed 11/05/24].

Cifelli, R. (1961). *Globigerina incompta, a new species of pelagic foraminifera from the North Atlantic*. Contributions from the Cushman Foundation for Foraminiferal Research. (12). 83-86.

Corliss, B.H., (1991). *Morphology and microhabitat preferences of benthic foraminifer from the northwest Atlantic Ocean*. Marine Micropalaeontology. (17) 3-4. 195-236.

Craig, H., (1953). *The geochemistry of Stable Carbon Isotopes*. Geochimica et Cosmochimica Acta. (3) 2-3. 53-92.

Cuffey , K.M. and Marshall, S.J., (2000). *Substantial contribution to sea level rise during the Last Interglacial from the Greenland Ice Sheet*. Naure. (404). 591-594.

Cushman, J. A. (1922). *Results of the Hudson Bay Expedition. I. The Foraminifera*. Contributions to Canadian Biology. (1921) 9. 133-147.

Dawson, J. W., (1860). *Notice of Tertiary fossils from Labrador, Maine, etc., and remarks on the climate of Canada in the newer Pliocene or Pleistocene period*. Canadian Naturalist and Geologist, Montreal. (5). 188-200.

Dimakis, P., Elverhøi, A., Høeg, K., Solheim, A., Harbitz, C., Laberg, J.S., Vorren, T.O. and Marr, J., (2000). *Submarine slope stability on high latitude galciatd Svalbard-Barents Sea margin*. Marine Geology. (162). 303-316.

Dallmann, W.K., (2015). *Chapter 8: Tectonic and tectonothermal events: 8-3 Long Lived Faults*. In: Dallmann, K.D. (2015). *Geoscience Atlas of Svalbard, Report Series No. 148*.Norsk Polarinstitutt. 181-185.

Duplessy, J.C., Moyes, J. and Pujol, C., (!980). *Deep water formation in the North Atlantic Ocean during the las ice age*. Nature. (286). 479-482.

Duplessy, J.C., Cortijo, E., Ivanova, E., Khusid, T., Labeyrie, L., Levitan, M. and Paterne, M., (2005). *Palaeoceanography of the Barents Sea during the Holocene*.

Ebbsen, H. and Hald, M., (2004).*Unstable Younger Dryas climate in the northeast North Atlantic*. Geology. (32) 8. 673-676.

Ehrenberg., (1961): Hayward, B.W.; Le Coze, F.; Vachard, D.; Gross, O. (2024). *World Foraminifera Database*. *Neogloboquadrina pachyderma* (Ehrenberg, 1861). [Online]. Accessed through: World Register of Marine Species at: https://www.marinespecies.org/aphia.php?p=taxdetails&id=113458 on 2024-05-14. [Accessed 13.05/24].

Eiken, O., (1994). *Seismic Atlas of Western Svalbard: A selection of regional seismic transects. Research Report. Meddelesler No. 130.* Norsk Polarinstitutt, Oslo.

Elger, J., Berndt, C., Krastel, S., Piper, D.J.W., Gross, F., Spielhagen, R.F. and Meyer, S., (2014). *The Fram DSlide: A submarine landslide on a low-sedimentation-rate glacial continental margin.* Journal of the Geological Society. (172). 153-156.

Elverhøi, A., Dowdeswell, J.A., Funders, S., Mangerud, J. and Stein, R., (1998).*Glacial and Oceanic History of the Polar North Atlantic Margin: An Overview.* Quaternary Science Reviewa. (17). 1-10.

Forwick, M., Laberg, J.S., Husum, K. and Gales, J.A,. (2016). *Submarine Mass Wasting on Hovgaard Ridge, Fram Strait, European Arctic*. In: Lamarche, G. et al., Submarine Mass Movements and Their Consequences. Advances in Natural and Technological Hazards Research. Vol 41. Springer.

Geissler, W.H. and Jokat, W., (2004). *A geophysical study of the northern Svalbard continental margin.* Geophysical Journal International. (158). 50-66.

Geissler, W.H., Gebhart, C.A., Gross, F., Wollenburg, J., Jensen, L., Schmidt, M.C., Krastel, S,. Elger, J. and Osti, G., (2016). *Arctic megaslide at presumed rest.* Scientific reports. (6). 38529.

GEOTEK Ltd., (2016). *Multi Sensor Core Logger Manual.*

Google Earth., (2024). *Overview globe showing the North Pole over continental Northern Europe [online]. Available at: https://earth.google.com/web/@79.65581214,14.16124473,-7253.36048464a,8779709.12278175d,35y,-8.06139998h,39.46363139t,0r. [Accessed 14/05/24].*

Glaser, B,. (2005). *Compound specific stable-isotope (δ13C) analysis in soil science.* Journal of Plant Nutrition and Soil Science. (168) 5. 633-648.

GRIP Members., (1993). *Climate instability during the last interglacial period recorded in the GRIP ice core.* Nature. (364). 203-207.

Gudmundssen, A., (1999). Postglacial crustial doming, stresses and fracture formation with application to Norway. Technophysics. (307). 407-419.

Hald, M. and Korsun, S., (1997). *Distribution of modern benthic foraminifera from fjords of Svalbard, European Arctic.* The Journal of Foraminiferal Research. (27) 2. 101-122.

Hald, M. and Steinsund, P.I., (1992). *Distribution o surface sediment benthic foraminfiera in the southwestern Barents Sea.* The Journal of Foraminiferal Research. (22) 4. 347-362.

Hald, M., and Vorren, T.O., (1987). *Stable isotope stratigraphy and palaeoceanography during the last deglaciation on the continental shelf off Troms, northern Norway.* Palaeoceanography. (2) 6. 583-599.

Haflidason, H., Lien, R., Sejurp, H.P., Forsberg, C.F, and Bryn, P., (2005). *The dating and morphometry of the Storegga Slide.* Marine and Petroleum Geology. (22). 123-136.

Heaton, T.J., Köhler, P., Butzon, M., Bard, E., Reimer, R.W., Austin, W.E.N., Bronk Ramsey, C., Grootes, P.M., Hughen, K.A., Kromer, B., Reimer, P.J., Adkins, J., Birk, A., Cook, M.S., Olsen, J. and Skinner, L.C., (2020). *Marine20 – The marine radiocarbon age calibration curve (0-55,000 cal BP).* Radiocarbon. (62). 848-875.

Hesjedal Wiberg, D., Haflidason, H. and Laberg, J.S., (2023). *An updated Weichselian framework for the Kongsfjorden Trough Mouth Fan and its implications for the glacial history of Svalbard*. BOREAS. (51) 3. 667-683.

Hogan, K.A., Dowdeswell, J. and Mienert, J., (2013). *New insights into slide processes and the seafloor geology revealed by side-scan imagery of the massive Hinlopen Slide, Arctic Ocean margin*. Geo-Marine Letters. (33). 325-343.

Hormes, A,. (2015). *Chapter 6: Historical Geology: 6-11 Neogene and Quaternary.* In: Dallmann, K.D. (2015). *Geoscience Atlas of Svalbard, Report Series No. 148.*Norsk Polarinstitutt. 181-185

Ingólfsson, O. and Landevik. J.Y., (2013). *The Svalbard-Barents sea ice-sheet – Historical, current and future perspectives*. Quaternary Science Reviews. (64). 33-60.

Innomar., (2024). *Innomar Deep-36: Parametric Sub-Bottom Profiler Product Flyer*. [Online] Available at: https://innomar.com/innomar-flyer/Innomar-deep-36.pdf. [Accessed 12/05/24].

Ivanova, E.V., Ovsepyan, E.A., Risebrobakklen, B., and Vetrov, A.A., (2008). *Downcore distribution of living calcareous foraminifera and stable isotopes in the western Barents Sea*. The Journal of Foraminiferal Research. (38) 4. 337-356.

Jakobsson, M., Mayer, L.A., Bringensparr, C., Castro, C.F., Mohammad, R., Johnson, P., Ketter, T., Accettella, D., Amblas, D., An, L., Arndt, J.E., Canals, M., Casamor, J.L., Cauche. N., Coakley, B., Danielson, S., Demarte, M., Dickson, M.L., Dorschel, B., Dowdeswell, J.A., Drutter, S., Fremand, A.C., Gallant, D., Hall, J.K., Hehemann, L., Hodnesdal, H., Hong, J., Ivaldi, R., Kane, E., Klaucke, I., Krawczyk, D.W., Kristoffersen, Y., Kuipers, B.R., Millian, R., Masetti, G., Morlighem, M., Noormets, R., Prescott, M.M., Rebesco, M., Rignot, E., Semiletov, I., Tate, A.J., Travaglini, P., Velicogna, I., Weatherall, P., Weinrebe, W., Willis, J.K., Wood, M., Zarayskaya, Y., Zhang, T., Zimmermann, M. and Zinglersen, K.B., (2020). *The International Bathymetric Chart of the Arctic Ocean Version 4.0*. Scientific Data. (7). 176.

Jennings, A.E., Weiner, N.J. Helgadottir, G. And Andrews, J.T., (2004). *Modern foraminiferal faunas of the southwestern to northern Iceland shelf: oceanographic and environmental controls*. The Journal of Foraminiferal Research. (34) 3. 180-207.

Jessen, S., Rasmussen, T.L., Nielsen, T. and Solheim, A., (2010). *A new Late Weichselian and Holocene marine chronology for the western Svalbard slope 30,000-0 cal years BP*. Quaternary Science Reviews. (29). 1301-1312.

Johnsen, S.J., Clausen, H.B., Dansgaard, W., Further, K., Gundestrup, N., Hammer, C.U., Iversen, P., Jousei, J., Stauffer, B. and Steffensen, J.P., (1992). *Irregular glacial interstadials in a new Greenland ice core*. Nature (359). 311-313.

Jokat, W., (2005). *The Sedimentary Structure of the Lomonosov Ridge between 88N and 80N*. Geophysical Journal International, (163) 2. 698-726.

Jouzei, J., Stauffer, B. And Steffensen, J.P., (1992). *Irregular glacial interstadials recorded in a new Greenland ice core*. Nature. (359). 311-313.

Kaarkinen, A., Salonen, V-P., Kubischta, F., Eskola, K. And Oinonen, M., (2009). *Weichselian glacial stages in Murchisonfjorden, Nordaustlandet, Svalbard*. Boreas. (38). 718-729.

Kanmacher F., (1798). *Essays on the microscope*. The Second Edition, with considerable additions and improvements. Dillon & Keating, London. xvii + [7 unnumbered] + 724 pp., 32 pl.

Kim, j., Løvholt, F., Issler, D. And Forsberg, C.F., (2019). *Landslide material control on tsunami genesis – The Storegga Slide and tsunami (8100 y BP)*. Journal of geophysical Research: Oceans. (124). 3607-3627.

Kireenko, L., Tikhonova, A., Kozina, N. And Matul, A., (2022). *Image dataset of benthic foraminifera taxa from Denmark Strait sediments on the northwestern Iceland Slope (North Atlantic Ocean*. Data in Brief. (42). 108040.

Knies, J., Matthiessen J., Vogt, C., Laberg, J.S., Hjelstuen, B.O., Smelror, M., Larsen, E., Andressen, K., Eidvin, T. And Vorren, T.O., (2009). *The Plio-Pleistocene glaciation of the Barents Sea-Svalbard region; a new model based on revised chronostratigraphy*. Quaternary Science Reviews. (28). 812-829.

Knies, J., Köseoğlu, D., Rise, L., Beaten, N., Bellec, K., Bøe, R., Klug, M., Panieri, G., Jernas, P.E. and Belt, S.T., (2018). *Nordic Seas polynyas and their role in preconditioning marine productivity during the Last Glacial Maximum*. Nature Communications. (9). 3959.

Koç, N., Klitgaard-Kristensen, D., Halse, K., Forsberg, C.F. and Solheim, A., (2002). *Late glacial palaeoceanography of Hinlopen Strait, Northern Svalbard*. Polar Research. (21) 2. 307-314.

Korsun, S. and Hald, M., (1998). *Modern benthic foraminifera off Novaya Zemlya tidewater glaciers, Russian Arctic*. Arctic and Alpine Research. (30) 1. 61-77.

Kristoffersen, Y., Coakley, B.J., Hall, J.K. and Edwards, M., (2007). *Mass wasting on the submarine Lomonosov Ridge central Arctic Ocean*. (243). 132-142.

Kristoffersen Y., Hall, J.K., Hunkins, K., Ardai, J., Coakley, B.J., Hopper, J.R. and Healy 2005 Seismic Team. (2009). *Extensive local seabed disturbance, erosion, and mass wasting on Alpha Ridge, Central Arctic Ocean: possible evidence for an extra-terrestrial impact?*. Norwegian Journal of Geology. (88) . 313-320.

Kujawa, A., Łącka M., Szymańska, N., Pawłowska, J., Teleiński, M.M. and Zajączkowski, M., (2021).*Could Norwegian fjords serve as an analogue for the future of the Svalbard fjords? State and fate of high latitude fjords in the face of progressive "atlantification."* Polar Biology. (44). 2217-2233.

Laberg, J.S. and Vorren, T.O., (1993). *A Late Pleistocene submarine slide on the Bear Island Trough Mouth Fan,* Geo-Marine Letters. (13). 227-234.

Laberg, J.S., and Vorren, T.O., (2000a). *The Trænadjupet Slide, offshore Norway – Morphology, evacuation and trigger mechanisms*. Marine Geology. (171). 95-114.

Laberg, J.S., and Vorren, T.O., (2000b). *Flow behavior of the submarine glacigenic debris flows on the Bear Island Trough Mouth Fan, Western Barents Sea*. (47). 1105-1117.

Laberg, J.S., Kawamura, K., Amundsen, H., Baeten, N., Forwick, M., Rydningen, T. and Vorren, v.o., (2014). *A submarine landslide complex affecting the Jan Mayen Ridge, Norwegian-Greenland Sea: slide scar morphology and processes of sediment evacuation*. Geo-Marine Letters (34). 51-58.

Laberg, J.S., Vorren, T.O., Dowdeswell, J.A., Keynon, N.H. and Taylor, J., (2000). *The Andøya Canyon, north- eastern Norwegian-Greenland Sea*. Marine Geology. (162). 259-275.

Landvik, J.Y., Bondevik, S., Elverhøi, A., Fjeldskaar, W., Mangerud, J., Salvigesn, O., Siegert, M.T., Ingesvendsen, J. and Vorren, T.O., (1998). *The last Glacial Maximum of Svalbard and the Barents Sea area: Ice sheet extent and configuration*. Quaternary Science Reviews. (17) 43-75.

Lindberg, B., Laberg, J.S. and Vorren, T.O., (2004). *The Nyk Slide – morphology. Progression and age of a partly buried submarine landslide offshore northern Norway*. Marine Geology. (213) 1-4. 277-289.

Linke, P. and Lutze, G.F., (1993). *Microhabitat preferences of benthic foraminifera – a static concept or a dynamic adaptation to optimise food acquisition?* Marine Micropalaeontology. (20) 3-4. 215-234.

Loeblich, A.R.; Tappan, H. (1953). Studies of Arctic foraminifera. Smithsonian miscellaneous collections. 121 (7):1–150., available online at https://biodiversitylibrary.org/page/27011009 page(s): p. 90, pl. 17, Figs. 4–7

Lokrantz, H. and Sohlenius, G., (2006). *Ice marginal fluctuations during the Weichselian glaciation in Fennoscandia, a literature review – Technical Report TR-06-36*. Geological Survey of Sweden (SGU).

Longva, O., Janbu, N., Blikra, L.H. and Bøe, R., (2003). *The 1996 Finneidfjord Slide; Seafloor failure and slide dynamics*. In: Locat, J., Minert, J. and Boisvert, L., (eds) *Submarine Mass Movement and Their Consequences*. Advances in Natural and Technological Hazards Research. (19). Springer, Dordrecht.

Mackensen, A. and Hald. M., (1998). *Cassidulina teretis Tappan and C. laevigata d'Orbigny; their modern and late Quaternary distribution in northern seas*. The Journal of Foraminiferal Research. (18) 1. 16-24.

Mangerud, J. and Svendsen, J.I., (1992). *The last interglacial-glacial period on Spitsbergen, Svalbard*. Quaternary Science. (11) 6. 633-664.

Mangerud, J. and Svendsen, J.I., (2017). *The Holocene Thermal Maximum around Svalbard, Arctic North Atlantic; molluscs show early and exceptional warmth*. The Holocene. 1-9.

Mangerud, J., Dokken, T., Hebbeln, D., Heggen, B., Ingólfssen, O., Landvik, J.Y., Mejdahl, V., Svendsen, J.I. and Vorren, T.O., (1998). *Fluctuations of the Svalbard-Barents Sea Ice Sheet during the Last 150,000 years*. Quaternary Science Reviews. (17). 11-42.

Mercer, J.H., (1978). *West Antarctic Ice Sheet and CO2 greenouse effecr: a threat of disaster*. Nature. (271). 321-325.

Mosher, D., Shimeld, J., Hutchinson, D., Lebedeva-Ivanova, N. and Chapman, C.B., (2012). *Submarine landslides in Arctic Sedimentation: Canada Basin*. Pages 147-158 in: Yamada et al., (2012). *Submarine mass movements and their consequences: Advances in Natural and Technological Hazards Research*. (31).

Myhre, A.M., Eldholm, O. and Sundvor, E., (1982). *The margin between Senja and Spitsbergen fracture zones: Implication from plate tectonics*. Tectonophysics. (89). 33-50.

Natland, M. L., (1938)., *New species of Foraminifera from off the west coast of North America and from the later Tertiary of the Los Angeles basin*. Bulletin of the Scripps Institution of Oceanography of the University of California, technical series. (4) 5. 137-163.

Orbigny, A. D. d'. (1826). *Tableau méthodique de la classe des Céphalopodes*. Annales des Sciences Naturelles. (7) 96-169, 245-314.

Osti, G., Franek, P., Forwick, M. and Laberg, J.S., (2017). *Submarine slope stability on high latitude glaciated Svalbard-Barents Sea margin*. Marine Geology. (162). 2-4. 303-316.

Pfirman, S. And Milliman, J.D., (1987). *Morphology, geology and oceanography of the Hinlopen Strait and Trough, Svalbard, Norway*.Polar Research. (5) 3. 297-298.

Pieńkowski, A.J., Coulthard, R.D. and Furze, M.F.A., (2023). *Revised marine reservoir offset (ΔR values for molluscs and marine mammals from Arctic North America*. Boreas. (52)145-167.

Polyak, L., Korsun. S., Febo, L.A., Stanovoy, SV., Khusid, T., Hald, M., Paulsen, B.E. and Lubinski, D.L., (2002). *Benthic Foraminiferal Assemblages from the Southern Kara Sea, A river influenced Arctic Marine Environment*. The Journal of Foraminiferal Research. (32) 3. 252-273.

Polyak, L. and Mikhailov, V., (1996). *Post-glacial environments of the southeastern Barents sea: foraminiferal evidence*. Geological Society of London. Special Publications. (111) 1. 323-337.

Reimer, P.J., Austin, W.E.N., Bard, E., Bayliss, A., Blackwell, P., Ramsey, C.B., Butzin, M., Cheng, H., Edwards, R.L., Friedrich, M., Grootes, P.M., Guilderson, T.P., Hajdas, I., Heaton, T.J., Hogg, A.G., Hughten, K.A., Kromer, B., Manning, S.W., Muscheler, R., Palmer, J.G., Pearson, C., Plichy, J.v.d., Reimer, R.W., Richards, D.A., Scott, E.M., Southon, J.R., Turney, C.S.M., Wacker, L., Adolphi, F., Büntgen, U., Capano, M., Fahrni, S.M., Fogtmann-Schultz, A., Friedrich, R., Köhler, P., Kudsk, S., Miyake, F., Olsen, J., Reinig F., Sakamoto, M., Sookdeo, A., Taalamo, S., (2020). *The IntCal20 Northern Hemisphere Radiocarbon age Calibration Curve (0-55 cal kBP)*. Radiocarbon. (62) 4. 725-757.

Rise, L., Ottesen, D., Longva, O., Solheim, A., Andersen, E.S. and Ayers, S., (2006). *The Sklinnadjupet slide and its relation to the Elsterian glaciation on the mid-Norwegian margin*. Marine and Petroleum Geology. (23). 569-583.

Rise, l., Chand, S., Hjelsteun, B.O., Haflindason, H. And Bøe, R., (2010). *Late Cenozoic geological development of the south Vøring margin, mid-Norway*. Marine and Petroleum Geology. (27). 1789-1803.

Rosen, J., Brook, E.J., Severinghaus, J.P., Blunier, T., Mitchell, L.E., Lee, J.E., Edwards, J.S. and Gkinis, V., (2014). *An ice core record of near-synchronous global climate changes at the Bølling transition*. Nature Geoscience. (7) 6. 459-463.

Rosman, K.J.R., and Taylor, P.D.P., (1998). *Isotopic compositions of the elements 1997*. Pure and Applied Chemistry. (70) 1. 217-235.

Rothwell, R.G., (2006). *New techniques in sediment core analysis*. Geological Special Publication. (267).

Reuss, A. E. (1851). *Ueber die fossilen Foraminiferen und Entomostraceen der Septarienthone der Umgegend ,von Berlin*. Zeitschrift der Deutschen Geologischen Gesellschaft. (3) 1. 49-92.

Safronova, P.A., Laberg. J.S., Andreassen, K., Shlykova, V., Vorren, T.O. and Chernikov, S. (2017)., *Late Pliocene-early Pleistocene deep-sea basin sedimentation at high latitudes: mega-scale submarine slides of the north western Barents Sea margin prior to the shelf edge glaciations*. Basin Research. (29). 537-555.

Salvigsen, O. and Nydal, R., (1981). *The Weichselian glaciation in Svalbard before 15,000 B.P*. BOREAS. (10) 4. 433-446.

Schlager, U., Jokat, W., Weigelt, E. And Gebhardt C., (2021). *Submarine landslides along the Siberian termination of the Lomonosov Ridge, Arctic Ocean*. Geomorphology. (328). 107696.

Schmitter, A., Bostock, H.C., Cartapanis, O., Curry, W.B., Filipsson, H.L., Galbraith, E.D., Gottschalk, J., Herguera, J.C., Hoogakker, B., Jaccard, S.L., Lisiecki, L.E., Lund, D.C., Martínez-Méndez, G., Lynch-Stieglitz, J., Mackensen, A. Michel, E., Mix, A.C., Oppo, D.W., Peterseon, C.D., Repschläger, J., Sikes E.L., Spero, H.J., and Wealbroeck, C., (2017). *Calibration of the carbon isotope compostioion (δ13C) of benthic foraminifera*. Paleoceanography. (32). 512-530.

Seidenkrantz, M.-S. (1995). Cassidulina teretis Tappan and Cassidulina neoteretis new species (Foraminifera): stratigraphic markers for deep sea and outer shelf areas. Journal of Micropalaeontology. (14) 2. 145-157.

Seidenkrants, M.S., (2013). *Northern meltwater pulses, CO2, and changes in Atlantic convection*. Science. (331) 6014. 156-158.

Sejrup, H.-P., Fjaeran, T., Hald, M., Beck, L., Hagen, J., Miljeteig, I., Norvik, I. and Norvik, O., (1981). *Benthonic foraminifera in surface samples from the Norwegian continental margin between 62 degrees N and 65 degrees N*. The Journal of Foraminiferal Research, 11(4), 277–295.

Shackelton, N.J., (1974). *Attainment of isotopic equilibrium between ocean water and the benthonic foraminifera genus Uvigerina: isotopic changes in the ocean during the Last Glacial*. Les methods quantitatives d´étude des vatiations du climat au cours du Pléistocéne, Colloques Inernationaux du C.N.R.S. (219). 203-209.

Shackelton, S., Baggenstos, D., Menking, J.A., Dyonisus, M.N., Bereiter, B., Bauska, T.K., Rhodes, R.H., Brook, E.J., Petrenko, V.V., McConnell, J.R., Kellerhals, T., Häberli, M., Schmitt, J., Fischer,

H. and Severinghaus, J.P., (2020). *Global ocean heat content in the Last Interglacial*. Nature Geoscience. (13). 77-81.

Sierstad, I.K., Johnsen, S.J., Vinther, B.M. and Olsen, J., (2005). *The duration of the Bølling-Allerød period (Greenland Interstadial 1) in the GRIP ice core*. Annals of Glaciology. (42). 337-344.

Sjundfjord, A., Gerland, S., Pavlov, V., Pavlova, O., (2015). Chapter 3: *Ocean and Sea Ice*. In: Dallmann, W.K. (2015). *Geoscience Atlas of Svalbard, Report Series No. 148.*Norsk Polarinstitutt. 31-34.

Skagseth, Ø, Furevik, t., Ingvaldsen, R., Loeng, H., Mork, K.A., Orvik, K.A. and Ozhigin, V., (2008). *Volume and heat transports to the Arctic Ocean via the Norwegian and Barents Seas*. In: Dickson, R.R., Meincke, J., and Rhines, P., (eds) *Arctic-Subarctic Ocean Fluxes*. Springer, Dordrecht.

Smith, D.E., Shi, S., Cullingford, R.A., Dawson, A.G., Dawson, S., Firth, C.R., Foster, I.D.L., Fretwell, P.T., Haggart, B.A., Holloway, L.K. and Long, D., (2004). *The Holocene Storegga Slide tsunami in the United Kingdom*. Quaternary Science Reviews. (23). 2291-2321.

Solheim, A., Berg, K., Forsberg, C.F. and Bryn, P., (2005). *The Storegga Slide complex: Repetitive large sliding with similar cause and development*. Marine and Petroleum Geology. (22). 97-107.

Stein, R. (Ed.). (2005). *Scientific Cruise Report of the Arctic Expedition ARK-XX/3 of RV ‘‘Polarstern’’ in 2004: Fram Strait, Yermak Plateau and East Greenland Continental Margin*. Berichte. Polarforsch. Meeresforsch. Alfred-Wegener-Institute, Bremerhaven, Germany. (517).

Steinsund, P.I., and Hald, M., (1994). *Recent calcium carbonate dissolution in the Barents Sea: Palaeoceanographic application*. Marine Geology. (117) 1-4. 303-316.

Stirling, C.H., Esat, T.M., Lambeck, K. and McCulloth., (1998). *Timing and duration of the Last Interglacial: Evodence for a restricted interval of widespread coral reef growth*. Earth and Planetary Science. (160). 745-762.

Stuiver, M. and Reimer, P.J., (2020). *Calib Radiocarbon Calibration Program*. Radiocarbon. (35). 215-230.

Sundvor, E., and Austegard, A., (1990). *The Evolution of the Svalbard Margins: Synthesis and New Results*. In: Bleil, U., and Thied, J., (EDS). Geological History of the Polar Oceans: Arctic versus Antarctic. Kluwer Academic Publishers. 77-94.

Sundvor, E. And Eldholm, O., (1976). *Marine geophysical survey on the continental margin from Bear Island to Hornsund, Spitsbergen, Scientific Report, University of Bergen.*Seismilogical Observatory. (3). 29.

Svendsen J.I., Elverhøi, A. and Mangerud, J., (1996). *The retreat of the Barents Sea Ice Sheet on the Western Svalbard Margin*. BOREAS. (25). 244-256.

Svendsen, J.I., Alexanderson, H., Astakhov, V.I., Demidov, I., Dowdeswell, J.A., Funder, S., Gataullin, V., Henriksen, M., Hjort, C., Houmark-Nielsen, M., Hubberten, H.W., Ingólfsson, Ó., Jakobsson, M., Kjær, K.H., Larsen, E., Lokrantz, H., Lunkka, J.P., Lysså, A., Mangerud, J., Matiouchkov, A., Murray, A., Möller, P., Niessen, F., Nikolskaya, O., Polyak, L., Saarnisto, M.,

Siegert, C., Siegert, M.J., Spielhagen, R.F., Stein, R., (2004a). *Late Quaternary ice sheet history of northern Eurasia*. Quaternary Science Reviews 23, 1229-1271.

Svendsen, J.I., (2004b). *The glacial history of the Barents and Kara Sea Region.* In: Ehlers, J. and Gibbard, P.L., Quaternary Glaciations – Extent and Chronology. Part 1: Europe. Developments in Quaternary Science, Elsevier. Amsterdam. 359-368.

Taylor, J., Dowdeswell., J.A. and Kenyoun, N.H., (2003). *Large Scale Slides in the North Norwegian Marign Imaged by GLORIA.* IN: Mienert, T. And Weaver, P.P.E., (2003).*European Margin Sediment Dynamics: Sidescan sonar and seismig images.* Springer-Verlag. Berlin. 37-44.

Uchio, T., (1960). *Ecology of living benthonic foraminifera from the San Diego, California, area*. Special Publications Cushman Foundation for Foraminiferal Research. (5). 1-72.

Vanneste, M., Mienert, J. and Bunz, S., (2006). *The Hinlopen Slide: A giant, submarine slope failure on the northern Svalbard margin, Arctic Ocean.* Earth and Planetary Science Letters. 245 (1-2). 373-388.

Vanneste, M., Harbitz, C.P., Blaso, F. GLIMSDAL, S., Mienert, J. And Elverhøi. (2010). *Hinlopen-Yermak landslide, Arctic Ocean – Geomorphology, Landslide dynamics, and Tsunami Simulations*. In: Shipp, R.C., Weimer, P. and Posamentier, H.W., (2010) *Mass Transport Deposits in Deepwater Settings.* SEPM Society for Sedimentary Geology. (96).

Vermassen, F, O'Regan, M., de Boer, A., Schenk, F., Razmjooei, M., West, G., Cronin, T., Jakobssen, M. and Coxall, H.K., (2023). *A seasonally ice-free Arctic Ocean during the Last Interglacial*. Nature Geoscience. (16). 723-729.

Vorren, O. and Laberg, J.S., (1997). *Trough Mouth Fans: Palaeoclimate and Ice-sheet monitors*. Quaternary Science Reviews. (16). 865-881.

Wagner, B., Bennike, O., Klug, M. And Cremer, H., (2006). *First Indication of Storegga Tsunami Deposits from East Greenland.* Journal of Quaternary Science. (22) 4. 321-325.

Weiberg, D.H., Haflidason, H. and Laberg, J.S., (2022). *An updated Weichselian chronostratigraphic framework of the Kongsfjorden Trough Mouth Fan and its implications for the glacial history of Svalbard.* Boreas. (51) 3. 667-683.

Williamson, W.C., (1858). *On the recent Foraminifera of Great Britain*. The Ray Society, London. 1-107.

Winkelann, D., Jokat, W., Niessen, F., Stein, R. and Winkler, A., (2006). *Age and extent of the Yermak Slide north of Spitsbergen, Arctic Ocean.* Geochemistry, Geophysics, Geosystems. (7) 6. 1-12.

Winkelmann, D., Jokat, W., Niessen, F, Stein, R, and Winkler, A., (2007). *Age and extent of the Yermak Slide north of Spitsbergen, Arctic Ocean.* Geology, Geophysics, Geosystems. (7) 6. 1-12.

Winkelmann, D., Geissler, W., Schneider, J., and Stein, R., (2008). *Dynamics and timing of the Hinlopen/Yermak megaslide north of Spitsbergen, Arctic Ocean*. Marine Geology. (250). 34-50.

Wollenburg, J. E., and Mackensen, A., (1998). *Living benthic foraminifers from the central Arctic Ocean: faunal composition, standing stock and diversity*. Marine Micropaleontology. (34). 153–185.

WoRMS Editorial Board., (2024). *World Register of Marine Species*. [Online]. Available at: https://www.marinespecies.org at VLIZ. [Accessed 13/05/24].

Zajączkowski, M., Szczuziński, W., Plessen, B. and Jernas, P., (2010). Benthic Foraminifera in Hornsund, Svalbard: Implications for palaeoenvironmental reconstructions. Polish Polar Research. (31) 4. 349-375.

Zhu, C., Peng, J., and Jia, Y., (2023). *Marine geohazards: Past, present, and future*. Engineering Goelogy. 323. 107230

8. Appendices:

8.1. Core 1168 - Sediment Grain Size

Section	Core Depth	True depth		Wet + Bag Weight (g)	Wet - Bag Weight (g)	Dry + Bag Weight (g)	Bag Weight (g)	True Weight (g)	<63 µm	63-100 µm	100-500 µm	>500 µm	<63 µm %	63-100 µm %	100-500 µm %	>500 µm %	Total %	Wet Bulk Density	Porosity	Dry Bulk Density	For	Comments
HH22-1168-GC-01	7-8cm	7-8cm	7	64.7702	64.4402	49.917	0.33	49.587	44.35	1.3292	2.3276	1.5801	89.439	2.6806	4.694	3.1866	100	1.6401	0.3781	1.2526	isotope	Samples picked from X-Ray following lamination;
	13-14cm	13-14cm	13	69.8592	69.5292	53.988	0.33	53.658	50.74	0.9929	1.1189	0.8053	94.563	1.8504	2.0853	1.5008	100	1.7696	0.404	1.3556	isotope	Samples picked from X-Ray following lamination;
	21-22cm	21-22cm	20	67.2604	66.9304	51.82	0.33	51.49	49.135	1.0603	0.7104	0.5848	95.425	2.0592	1.3797	1.1357	100	1.7035	0.393	1.3007	isotope	Samples picked from X-Ray following lamination; 21-22:19-20
	30-31cm	28-29cm	29	79.5563	79.2263	60.938	0.33	60.608	59.023	0.9606	0.387	0.2369	97.386	1.5849	0.6385	0.3909	100	2.0164	0.4739	1.5307	isotope	Samples picked from X-Ray following lamination; 30-31:28-29
	45-46cm	45-46cm	47	86.3725	86.0425	66.303	0.33	65.973	64.903	0.5758	0.302	0.1922	98.378	0.8728	0.4578	0.2913	100	2.1899	0.5108	1.6664	isotope	Samples picked from X-Ray following lamination; 49-50:45-46
	58-59cm	58-59cm	60.5	73.3137	72.9837	55.791	0.33	55.461	54.96	0.3648	0.1014	0.0348	99.097	0.6578	0.1828	0.0627	100	1.8576	0.446	1.4004	isotope	Samples picked from X-Ray following lamination; 63-64:58-59
	74-75cm	74-75cm	77	79.1858	78.8558	60.694	0.33	60.364	59.421	0.6963	0.2309	0.0159	98.438	1.1535	0.3825	0.0263	100	2.007	0.4706	1.5246	isotope	Samples picked from X-Ray following lamination; 80-81:74-75
	96-97cm	91-92cm	93	82.2078	81.8778	62.764	0.33	62.434	61.736	0.5327	0.1557	0.0097	98.882	0.8532	0.2494	0.0155	100	2.0839	0.4949	1.5767	isotope	Samples picked from X-Ray following lamination; 96-97:90-91
HH22-1168-GC-02	6-7cm	101-102cm	104	80.0591	79.7291	62.975	0.33	62.645	61.864	0.6482	0.1253	0.0076	98.753	1.0347	0.2	0.0121	100	2.0292	0.4348	1.5836	isotope	Samples picked from X-Ray following lamination; 06-07:00-01
	22-23cm	117-118cm	120	78.7784	78.4484	60.66	0.33	60.33	59.873	0.3758	0.0725	0.0091	99.242	0.6229	0.1202	0.0151	100	1.9967	0.4611	1.524	isotope	Samples picked from X-Ray following lamination; 22-23:16-17
	29-30cm	123-124cm	127	112.001	111.671	91.284	0.33	90.954	89.713	0.9071	0.2396	0.0941	98.636	0.9973	0.2634	0.1035	100	2.8422	0.5273	2.3018	14C	Samples picked from X-Ray following lamination; 29-30:23-24
	30-31cm	124-125cm	128	66.6785	66.3485	55.244	0.33	54.914	54.568	0.2627	0.0682	0.0156	99.369	0.4784	0.1242	0.0284	100	1.6887	0.291	1.3904	14C	Samples picked from X-Ray following lamination; 30-31:24-25
	31-32cm	125-126cm	129	81.9628	81.6328	68.386	0.33	68.056	66.734	0.9359	0.3329	0.0533	98.057	1.3752	0.4892	0.0783	100	2.0777	0.3456	1.7235	14C	Samples picked from X-Ray following lamination; 31-32:25-26
	32-33cm	126-127cm	130	59.7881	59.4581	51.191	0.33	50.861	50.198	0.4924	0.1397	0.0305	98.697	0.9681	0.2747	0.06	100	1.5133	0.2188	1.289	14C	Samples picked from X-Ray following lamination; 32-33:26-27
	42-43cm	137-138cm	140	85.7761	85.4461	78.499	0.33	78.169	46.407	4.8311	12.078	14.853	59.367	6.1804	15.452	19.001	100	2.1748	0.1852	1.9849		Samples picked from X-Ray following lamination; 42-43:36-37
	57-58cm	152-153cm	155	196.173	195.843	94.569	0.33	94.239	61.828	6.2973	14.991	11.124	65.607	6.6823	15.907	11.804	100	4.9845	2.586	2.3339		Samples picked from X-Ray following lamination; 57-58:51-52
	70-71cm	165-166cm	168	76.3968	76.0668	72.639	0.33	72.309	47.366	5.0695	11.99	7.8834	65.505	7.0109	16.581	10.902	100	1.936	0.0956	1.838		Samples picked from X-Ray following lamination; 70-71:64-65

8.2. Core 1192 – Sediment Grain Size

Section	Core Depth	True depth		Wet + Bag Weight (g)	Wet - Bag Weight (g)	Dry + Bag Weight (g)	Bag Weight (g)	True Weight (g)	<63 µm	63-100 µm	100-500 µm	>500 µm	<63 µm %	63-100 µm %	100-500 µm %	>500 µm %	Wet Bulk Density	Porosity	Dry Bulk Density		For
HH22-1192-GC-01	3-4cm	3-4cm	3	66.5789	66.2389	51.0187	0.34	50.6787	26.1453	15.6779	8.7769	0.0786	51.5903	30.9359	17.3187	0.15509	2.082329	0.489160641	1.58094	100	isotope
	18-19cm	18-19cm	18	67.7036	67.3636	50.2485	0.34	49.9085	31.6722	12.3362	5.7884	0.1117	63.4605	24.7176	11.598	0.22381	2.117686	0.548729959	1.55524	100	isotope
	22-23cm	22-23cm	22	52.2134	51.8734	35.8582	0.34	35.5182	27.9387	5.4758	2.0841	0.0196	78.6602	15.4169	5.8677	0.05518	1.630726	0.514152782	1.10372	100	
	23-24cm	23-24cm	23	48.4221	48.0821	32.4205	0.34	32.0805	25.4982	4.8905	1.6559	0.0359	79.4819	15.2445	5.1617	0.11191	1.51154	0.503036781	0.99593	100	
	24-25cm	24-25cm	24	48.269	47.929	32.553	0.34	32.213	26.3524	4.2218	1.6197	0.0191	81.8067	13.1059	5.02809	0.05929	1.506727	0.494058472	1.00032	100	isotope
	25-26cm	25-26cm	25	56.0461	55.7061	40.0832	0.34	39.7432	30.6651	5.5419	3.1038	0.4324	77.1581	13.9443	7.80964	1.08798	1.751213	0.501820182	1.23685	100	
	33-34cm	33-34cm	33	61.5863	61.2463	44.9557	0.34	44.6157	34.2675	3.0303	4.2704	3.0475	76.8059	6.792	9.57152	6.83056	1.925379	0.522810437	1.3895	100	
	48-49cm	48-49cm	48	73.347	73.007	57.0667	0.34	56.7267	35.1779	3.5952	10.4613	7.4923	62.0129	6.33776	18.4416	13.2077	2.295096	0.511798177	1.7705	100	
	57-58cm	57-58cm	57	66.53	66.19	51.8671	0.34	51.5271	32.3422	3.5103	10.7025	4.9721	62.7674	6.81253	20.7706	9.64949	2.080792	0.460952531	1.60832	100	
	63-64cm	63-64cm	63	67.3227	66.9827	51.3766	0.34	51.0366	34.6105	4.0497	8.6385	3.7379	67.8151	7.93489	16.9261	7.32396	2.105712	0.501292047	1.59189	100	
	78-79cm	78-79cm	78	67.704	67.364	52.3428	0.34	52.0028	34.9661	2.6881	10.2772	4.0714	67.2389	5.16914	19.7628	7.82919	2.117699	0.482904747	1.62272	100	
	93-94cm	93-94cm	93	70.7075	70.3675	55.7957	0.34	55.4557	34.9736	3.786	12.1998	4.4963	67.2533	6.82707	21.9992	8.10791	2.212119	0.468777114	1.73162	100	
HH22-1192-GC-02	10-11cm	107.5-108.5cm	107	62.5652	62.2252	48.5851	0.34	48.2451	31.1847	3.0333	10.2174	3.8097	64.6381	6.28727	21.1781	7.89655	1.956152	0.439487583	1.50568	100	
	25-25cm	122.5-123.5cm	122	60.662	60.322	47.4945	0.34	47.1545	32.5293	2.5135	7.2733	4.8384	68.9845	5.33035	15.4244	10.2607	1.896322	0.413942157	1.47203	100	
	40-41cm	137.5-138.5cm	137	71.2845	70.9445	59.5711	0.34	59.2311	12.2194	4.4163	42.0012	0.5942	20.63	7.45605	70.9107	1.00319	2.230258	0.368230116	1.85282	100	
	41-42cm	138.5-139.5cm	138	59.2877	58.9477	49.2271	0.34	48.8871	10.9632	2.2467	34.1341	1.5431	22.4255	4.59569	69.8223	3.15646	1.853119	0.316271613	1.52894	100	
	42-43cm	139.5-140.5cm	139	47.1582	46.8182	39.2889	0.34	38.9489	8.5559	1.1599	27.6427	1.5904	21.967	2.978	70.9717	4.0833	1.471808	0.24738447	1.21824	100	
	49-50cm	146.5-147.5cm	146	59.557	59.217	29.0548	0.34	28.7148	23.4651	1.7685	3.268	0.2132	81.7178	6.15884	11.3809	0.74247	1.861584	0.958887142	0.87873	100	isotope
	50-51cm	147.5-148.5cm	147	44.0876	43.7476	31.8827	0.34	31.5427	23.9975	1.9874	5.2549	0.3029	76.0794	6.30067	16.6596	0.96029	1.375278	0.383681232	0.982	100	isotope
	54-55cm	151.5-152.5cm	151	-	-	49.8639	0.34	49.5239	13.6229	1.9375	31.93	2.0335	27.5077	3.91225	64.4739	4.1061	-			100	
	55-56cm	152.5-153.5cm	152	85.0972	84.7572	72.1804	0.34	71.8404	12.2084	2.7541	54.1533	2.7246	16.9938	3.83364	75.38	3.79257	2.664483	0.406060987	2.24827	100	
	56-57cm	153.5-154.5cm	153	55.5608	55.2208	46.7399	0.34	46.3999	9.4617	2.2124	33.8389	0.8869	20.3916	4.76811	72.9288	1.91143	1.735957	0.277299591	1.45173	100	
	62-63cm	159.5-160.5cm	159	47.8937	47.5537	37.8622	0.34	37.5222	22.5752	2.3545	2.588	10.0045	60.1649	6.27495	6.89725	26.6629	1.494929	0.315356806	1.17169	100	
	70-71cm	167.5-168.5cm	167	65.175	64.835	47.3734	0.34	47.0334	41.1308	3.8806	1.8145	0.2075	87.4502	8.25073	3.8579	0.44118	2.038196	0.55962276	1.46458	100	isotope
	85-86cm	182.5-184.5cm	182	91.6683	91.3283	64.7201	0.34	64.3801	58.7925	3.5918	1.8241	0.1717	91.3209	5.57905	2.83333	0.2667	2.871056	0.84716127	2.00272	100	isotope
	99-101cm	196.5-198.5cm	196	86.1279	85.7879	61.0218	0.34	60.6818	52.8724	4.7701	2.6868	0.3525	87.1306	7.86084	4.42769	0.5809	2.696885	0.789251808	1.8879	100	isotope
HH22-1192-GC-03	10-12cm	211-213cm	211	125.5069	125.1669	94.525	0.34	94.185	59.7506	7.5325	13.4484	13.4535	63.4396	7.99756	14.2787	14.2841	3.934829	0.973967306	2.93651	100	isotope
	12-14cm	213-215cm	213	102.808	102.468	72.242	0.34	71.902	58.0785	4.8442	6.9447	2.0346	80.7745	6.73723	9.65856	2.82968	3.221251	0.960892801	2.23634	100	
	27-29cm	226-228cm	226	103.8665	103.5265	78.0893	0.34	77.7493	54.6978	13.2951	8.5545	1.2019	70.3515	17.1	11.0027	1.54587	3.254527	0.810348947	2.42392	100	isotope
	42-44cm	241-243cm	241	88.1531	87.8131	63.9555	0.34	63.6155	51.3767	6.8915	4.9188	0.4285	80.7613	10.8331	7.73208	0.67358	2.76055	0.760691606	1.98084	100	isotope
	57-59cm	256-258cm	256	105.9597	105.6197	76.0078	0.34	75.6678	68.1624	3.4011	2.6404	1.4639	90.0811	4.49478	3.48946	1.93464	3.32033	0.941587551	2.3552	100	isotope
	69-70cm	268-269cm	268	52.3662	52.0262	36.7244	0.34	36.3844	32.6151	1.9529	1.5058	0.3106	89.6403	5.36741	4.13859	0.85366	1.63553	0.491725872	1.13151	100	isotope
	70-71cm	269-270cm	269	58.8336	58.4936	40.2354	0.34	39.8954	35.746	2.5996	1.3634	0.1864	89.5993	6.51604	3.41744	0.46722	1.838843	0.5846652	1.23956	100	
	71-72cm	270-271cm	270	71.5611	71.2211	53.3687	0.34	53.0287	46.9654	4.3179	1.7345	0.0109	88.566	8.14257	3.27087	0.02055	2.238953	0.571908205	1.65275	100	
	72-73cm	271-272cm	271	56.308	55.968	44.1055	0.34	43.7655	38.7261	3.6154	1.4194	0.0046	88.4855	8.26084	3.24319	0.01051	1.759447	0.383605784	1.36625	100	
	77-78cm	276-277cm	276	53.0493	52.7093	39.8321	0.34	39.4921	38.3976	1.0257	0.0688	0	97.2286	2.59723	0.17421	0	1.657004	0.415504558	1.23111	100	isotope
	87-88cm	286-287cm	286	64.3064	63.9664	51.1672	0.34	50.8272	43.8207	5.5258	1.4806	0.0001	86.2151	10.8717	2.91301	0.0002	2.01089	0.413052499	1.58751	100	isotope
	95-96cm	294-295cm	294	586.5854	586.2454	45.2766	0.34	44.9366	44.8186	0.05983	0.0425	0.0157	99.7373	0.13314	0.09458	0.03494	18.42959	17.01693807	0.98723	100	isotope
HH22-1192-GC-04	4-5cm	305.5-306.5cm	305	54.5438	54.2038	43.9721	0.34	43.6321	43.2352	0.3576	0.0359	0.0034	99.0903	0.81958	0.08228	0.00779	1.703986	0.332338887	1.36334	100	isotope
	19-20cm	320.5-321.5cm	320	61.7397	61.3997	50.007	0.34	49.667	40.0713	5.9833	3.4581	0.1543	80.6799	12.0468	6.96257	0.31067	1.930201	0.368836844	1.55214	100	isotope
	22-23cm	323.5-324.5cm	323	63.4853	63.1453	50.8788	0.34	50.5388	41.5188	2.4168	1.6712	4.932	82.1523	4.78207	3.30677	9.75884	1.985077	0.396306193	1.57886	100	isotope
	34-35cm	335.5-336.5cm	335	52.9288	52.5888	39.4464	0.34	39.1064	35.5502	2.6278	0.8271	0.1013	90.9063	6.71962	2.115	0.25904	1.653216	0.423841559	1.21878	100	isotope
	49-50cm	350.5-351.5cm	350	51.234	50.894	37.8859	0.34	37.5459	34.5822	1.948	0.8509	0.1648	92.1065	5.18832	2.26629	0.43893	1.599937	0.419619616	1.16983	100	isotope
	53-54cm	354.5-355.5cm	354	49.6389	49.2989	39.1024	0.34	38.7624	38.0967	0.3992	0.2198	0.0467	98.2826	1.02986	0.56704	0.12048	1.549793	0.331232317	1.21028	100	isotope
	57-58cm	358.5-259.5cm	358	47.3394	46.9994	34.9531	0.34	34.6131	31.2793	1.9046	0.9094	0.5198	90.3684	5.50254	2.62733	1.50174	1.477504	0.389383842	1.07839	100	isotope
	64-65cm	265.5-266.5cm	365	50.6906	50.3506	40.389	0.34	40.049	39.114	0.7358	0.1669	0.0323	97.6654	1.83725	0.41674	0.08065	1.582854	0.323847847	1.25091	100	isotope

8.3. Core 1168 – Foraminifera results

Section	Core Depth	True depth	Agglutinate sp.	A. Gallowayi	B. skaggerensis	B. frigga	Bolivina skaggerrakensis	B. marginata	Bulimina sp.	C. laevigata	C. neoteretis	C. reniforme	C. teretis	Cassidulina sp	C. lobatulus	C. refulgens	Cibicides sp	Discorbis vilardeboanus	Dentalina sp	E. excavatum	E. arctica	Fissurina sp	F. complanata	Furkensonia sp.	Hanzawia boueana	H. balthica	I. norcrossi	I. algida	Islandella sp.	Lagena sp	M. bareelanus	Melonis sp	Miliolina sp	N. labradorica	Nononionellina sp.	N. turgida	P. osloensis	P. bulloides	Pullimina sp.	Portatrochammina bipolaris	Pyrgo sp.	Quinqueloculina sp	Rosalina obtusa	Rosalina sp	S. loeblichi	S. fusiformis	Stainforthia sp.	T. angulosa	Trifarina sp.	Triloculina Trihedra	Other	Buccella spp (Buccella hannai)
HH22-1168-GC-01	7-8cm	7-8cm		1		4		1	2	1	2	17		4	40					2		3						1		17			7														3			1	7
	13-14cm	13-14cm		4		15	1				9	24		6				1		3		4					2	1		21			7																	8	
	21-22cm	21-22cm		2		14	1				9	42		7	41					2	1	1	1				1	1	1		31	1		4																3	
	30-31cm	30-31cm	1	2		32	2		1	1	8	46		8	14					5			1				4	10	1		49	4		4					1			1			1	1				6	
	45-46cm	45-46cm		29		39	2	2			16	111		13	53					6		4	3				3	7	2	1	64			3						1									1	8	5
	58-59cm	58-59cm		6		33	1			2	8	70		6	23					3	4	1	1					5	2		36			6							1								1	4	4
	74-75cm	74-75cm		28		38	3			3	7	80		9	31		2			3	4	3	4				4	6	5		50	1		3												1			11	
	96-97cm	96-97cm		12		25	2	1		4	6	74		5	9					2	1	1	3				1	3	3		36			1									1							5	1
1168-02	6-7cm	105-106cm		26		44	2	1		3	8	161		9	34					9	4	4	7				7	4	10		66			7							1						1			10	1
	22-23cm	121-122cm																																																	
	29-30cm	128-129cm		26		72	4	2	4	1	36	178		31	62		3			18	1	4	4	3		2	4	24	2	4	121			6	4			1					2				2		1	15	2
	30-31cm	129-130cm		18		42	1	3		3	36	175		18	82					9	1	2	1			1	7	27	7	2	105			2	2													1	1	11	3

8.4. Core 1192 – Foraminifera Results

Section	Core Depth	True depth	Ammodiscus sp	A. Gallowayi	B. skaggerensis	B. fridga	Bucella ssp (Bucella hamai)	B. marginata	C. laevigata	C. neoteretis	C. reniforme	C. teretis	Cassidulina sp	C. lobatulus	C. refulgens	Cibicides sp	Discorbis vilardeboanus	E. excavatum	E. arctica	Fissurina sp	F. complanata	Globocassidulina sp.	H. balthica	I. norcrossi	I. algida	Islandella sp.	Lagena sp	M. barealanus	Melonis sp	Miliolina sp.	N. labradorica	N. turgida	P. bulloides	Portatrochammina bipolaris	Pygo sp.	Quinqueloculina sp	S. loeblichi	S. fusiformis	Triferina sp.	Triloculina Trihedra	Other	Total Benthics	N. pachyderma	N. incompta	Neogloboquadrina sp.	T. quinqueloba	Total Planktic
1192 1192-0	3-4cm	3-4cm		10		3			4	3	4		4	5				3	4					2		3		21	1												3	70	28			1	29
	18-19cm	18-19cm		23		54	2	1	4	6	33		7	79				4	4	9	2	2		5	7		8	110			13	6	3						4		15	401	192	0	0	1	193
	24-25cm	24-25cm		8		16			7	7	47		11	42				2	1	2	1			6	1		1	36			5	1	3						1			198	102	5	3	1	111
	70-71cm	167-168		3		1			62	51	49	1	40	13	1	2		7	1	2	4			42	2	6		15	3		8	1				1		2	1	3	321	31				31
	85-86cm	182-184		10				1	44	73	42	1	34	17	2						2			70		5		16	3		1	2									323	49		1		50
1192 03	10-12cm	211-213cm		6		1			26	27	32		9	12	1	3		7		1	4			19	2			24	2	1	3	1			1				3	7	192	185	2			187
	27-29cm	226-228cm		9		4	1		10	6	18		4	12		7		8	1		2			12	2	2		101		3	15	5						1			7	230	26	2			28
	42-44cm	241-243cm	1	1		1			1	4	8		4	2						1	2			4				3			2										1	35	11	1			12
	69-70cm	268-269cm	1	17		1		2	7	33	24		20	11			1	9			1		1	12	14		1	89	5		25			1					4	3	282	92	1			93
	87-88cm	286-287cm		9					5	96	51		33	15				6		2	7			21	1			34	3		23						4			1	4	315	16	1			17

Core Depth	True depth																																													
3-4cm	3-4cm		14.29		4.286			5.714	4.286	5.714		5.714	7.143				4.286	5.714					2.857		4.286		30	1.429												4.286	100	96.55	0	0	3.448	100
18-19cm	18-19cm		5.736	0	13.47	0.499	0.249	0.998	1.496	8.229	0	1.746	19.7	0	0	0	0.998	0.998	2.244	0.499	0.499	0	1.247	1.746	0	1.995	27.43	0	0	3.242	1.496	0.748	0	0	0	0	0	0.998	0	3.741	100	99.48	0	0	0.518	100
24-25cm	24-25cm		4.04	0	8.081	0	0	3.535	3.535	23.74	0	5.556	21.21	0	0	0	1.01	0.505	1.01	0.505		0	3.03	0.505	0	0.505	18.18	0	0	2.525	0.505	1.515	0	0	0	0	0	0.505	0	0	100	91.89	4.5	2.703	0.901	100
70-71cm	167.5-168.5cm		0.935		0.312			19.31	15.89	15.26	0.312	12.46	4.05	0.312	0.623		2.181	0.312	0.623	1.246			13.08	0.623	1.869		4.673	0.935		2.492	0.312				0.312	0	0.623	0.312		0.935	100	100	0	0	0	100
85-86cm	182.5-184.5cm		3.096				0.31	13.62	22.6	13	0.31	10.53	5.263	0.619						0.619				21.67		1.548		4.954	0.929		0.31	0.619									100	98	0	2	0	100
10-12cm	211-213cm		3.125		0.521			13.54	14.06	16.67		4.688	6.25	0.521	1.563		3.646		0.521	2.083				9.896	1.042			12.5	1.042	0.521	1.563	0.521			0.521				1.563	3.646	100	98.93	1.07	0	0	100
27-29cm	226-228cm		3.913		1.739	0.435		4.348	2.609	7.826		1.739	5.217		3.043		3.478	0.435		0.87				5.217	0.87	0.87		43.91		1.304	6.522	2.174						0.435			3.043	100	92.86	7.14	0	0	100
42-44cm	241-243cm	2.857	2.857	0	2.857	0	0	2.857	11.43	22.86	0	11.43	5.714	0	0	0	0	0	2.857	5.714		0	11.43	0	0	0	8.571	0	0	5.714	0		0	0	0	0	0	0	0	2.857	100	91.67	8.33	0	0	100
69-70cm	268-269cm	0.355	6.028	0	0.355		0.709	2.482	11.7	8.511	0	7.092	3.901	0	0	0.355	3.191	0	0	0.355		0.355	4.255	4.965	0	0.355	31.56	1.773	0	8.865	0		0.355	0	0	0	0	0	1.418	1.064	100	98.92	1.08	0	0	100
87-88cm	286-287cm		2.857					1.587	30.48	16.19		10.48	4.762				1.905		0.635	2.222			6.667	0.317			10.79	0.952		7.302						1.27			0.317	1.27	100	94.12	5.88	0	0	100

8.5. 14C AMS Results from Zurich University

ETH nr.	sample label	sample label #	^{14}C coun	^{12}C (µA	$^{14}C/^{12}C$ (10^{-1}	+- (%)	$^{13}C/^{12}C$ (%)	sigma (%)	$F^{14}C$	+- (%)	sig (%)	age (y)	+-(y)	user
142104.1.2	25-26cm	1	8,892	6.5	0.2882	1.06	1.1021	0.07	0.2266	1.13	1.07	11,926	90	Hooton
142105.1.2	139.5-140.5cm	2	3,481	6.3	0.1190	1.69	1.1074	0.06	0.0898	1.86	1.86	19,357	149	Hooton
142106.1.2	167.5-168.5	3	7,202	6.6	0.2461	1.18	1.1055	0.06	0.1916	1.25	1.30	13,273	101	Hooton
142107.1.1	28-32-cm	4	285	5.6	0.0185	5.92	1.0964	0.03	0.0100	9.73	7.76	36,968	781	Hooton

8.6. Stable Isotope Raw Results

No.	Depth (cm)		Species	Count		Farlab ID	δ13C ‰ VPDB	δ18O ‰ VPDB	comments
1	3-4cm		M. barleeanus	13		2024-011-0	-1.36	3.72	
2	3-4cm		N. laboradorica	13		2024-011-0	-0.72	4.54	
3	3-4cm		C. reniforme	12		2024-011-0	-0.77	4.21	very small sample (12 micrograms),
4	3-4cm		N. pachyderma	12		2024-011-0	0.28	3.13	marginal reliability, lower precision
5	18-19cm		N. laboradorica	13		2024-011-0	-1.04	4.57	
4	18-19cm		M. barleeanus	11		2024-011-0	-1.40	4.09	
7	18-19cm		C. reniforme	28		2024-011-0	-1.05	3.89	
8	18-19cm		N. pachyderma	21		2024-011-0	0.50	3.14	
9	24-25cm		M. barleeanus	12		2024-011-0	-1.50	4.10	
10	24-25cm		C. reniforme	26		2024-011-1	-1.14	4.00	
11	24-25cm		N.pachyderma	37	92 Core	2024-011-1	0.14	3.47	
12	139.5cm		N.pachyderma	11		2024-011-1	0.09	4.63	
13	167.5cm		C. reniforme	15		2024-011-1	-0.81	5.01	
14	167.5cm		C. neoteretis	15		2024-011-1	-0.74	5.09	
15	182.2cm		M. barleeanus	8		2024-011-1	-1.60	4.57	
16	211cm		M. barleeanus	11		2024-011-1	-1.07	4.58	
17	226cm		M. barleeanus	18		2024-011-1	-1.45	4.25	
18	241cm		Mixed	15		2024-011-1	-0.82	4.68	
19	256cm		C. reniforme	30		2024-011-1	-1.28	4.61	
20	268cm		M. barleeanus	14		2024-011-2	-1.42	4.51	
21	286cm		C. reniforme	23		2024-011-2	-1.30	4.12	
22	7cm	7	C. reniforme/M. barleear	16		2024-011-2	-0.90	4.16	
23	13cm	13	C. reniforme	20		2024-011-2	-0.80	3.98	
24	21cm	21	C. reniforme	25		2024-011-2	-0.85	3.98	
25	30cm	30	C. reniforme	30		2024-011-2	-1.31	4.18	
26	45cm	45	C. reniforme	39		2024-011-2	-1.32	4.27	
27	58cm	58	C. reniforme	32	68 Core	2024-011-2	-1.49	4.11	
28	74cm	74	C. reniforme	38		2024-011-2	-1.35	4.33	
29	96cm	96	C. reniforme	37		2024-011-2	-1.51	4.17	
30	105cm	105	C. reniforme	37		2024-011-3	-1.56	4.26	
31	128cm	128	C. reniforme	35		2024-011-3	-1.33	4.32	
32	130cm	130	C. reniforme	35		2024-011-3	-1.42	4.29